DYNAMICS OF A SPIN-1 BEC IN THE REGIME OF A QUANTUM INVERTED PENDULUM

A Thesis
Presented to
The Academic Faculty

by

Corey S. Gerving

In Partial Fulfillment
of the Requirements for the Degree
Doctor of Philosophy in the
School of Physics

Georgia Institute of Technology
May 2013

DYNAMICS OF A SPIN-1 BEC IN THE REGIME OF A QUANTUM INVERTED PENDULUM

Approved by:

Professor Michael S. Chapman,
Advisor
Department of Physics
Georgia Institute of Technology

Professor T.A.Brian Kennedy
Department of Physics
Georgia Institute of Technology

Professor Andrew Zangwill
Department of Physics
Georgia Institute of Technology

Professor Kenneth Brown
Department of Chemistry
Georgia Institute of Technology

Professor Professor Carlos Sa de Melo
Department of Physics
Georgia Institute of Technology

Date Approved: 14 March 2013

To Emily and Gabriella, whom I seek to inspire with my dedication and commitment. I hope this serves as an example for you in your future endeavors.

To my wife Natalie, I thank you for your support and patience.

ACKNOWLEDGEMENTS

One does not get to where I am without the support of a great many people throughout the years. My career path has been very unlike what most people in the academic world are used to. I have been on active duty in the Army since 1995. I was given the opportunity to attend two different graduate schools while still in the Army, an experience a very small percentage of officers are afforded. My acknowledgements will be directed at both military and civilian people who have influenced me over the last 18 years. I want to thank the following professors from my undergraduate years: COL(retired) Vernon Davis, COL(retired) John LaSala, COL(retired) Bruce Oldaker, and Brigadier General (retired) Raymond Winkel for their passion for the discipline of physics and their rigorous approach to problem solving. I also want to thank the following professors from my Masters Degree years: Professor Brett Esry, Professor Amit Chakrabarti, Professor Larry Weaver, and my thesis advisor, Professor Chris Sorensen.

When I applied to Georgia Tech three years ago, it was imperative that I find an advisor who would let me start work on getting results immediately. I was introduced to Professor Mike Chapman. He showed me the lab, and I knew that it is where I wanted to work. Luckily for me, Mike had an opening on the BEC project, and he was willing to take a chance on an old guy like me. His patience was appreciated, and his ability to explain complicated things in simple terms was always refreshing. I should also thank the Georgia Tech School of Physics graduate admissions people for taking a chance on me in the first place. A 37-year old who hasn't taken a physics class in six years who needs to finish a PhD in three years is a tough sell, but they rolled the dice.

I owe a huge debt of gratitude to Dr. Chris Hamley. He was put in charge of making sure I figured everything out, and he made sure I was always doing something constructive. Many people consider Chris to be a curmudgeonly old man, but I didn't mind, since I was older than him and we came from a similar background. In all honesty, though, I don't know what I would have done if Chris wasn't here to help me along, so if he ever lowers himself to read my thesis, thank you.

Another thank you goes out to my teammates on the BEC experiment, Thai and Martin. We spent countless hours repairing the experiment when it wasn't working, and sitting in complete darkness when it was. Thai is a manic worker and Martin is extremely efficient in his execution of tasks. The experiment is in good hands, likely better hands, as I leave.

I also want to acknowledge Mike DePalatis, the only person in the lab that was willing and able to discuss sports at any time. Despite his affinity for burnt orange and large-horned bovines, he was a solid conversationalist. Additionally, he is an excellent physicist. He was very helpful on many occasions.

While on the subject of excellent physicists who were helpful, I would be remiss if I did not thank Dr. Chung-Yu Shih. He was a quiet professional with an abundance of knowledge.

We have been very fortunate in our lab to have snagged two excellent undergraduate assistants. I want to thank Ben Land for his brilliant work with the simulations and all of the help he provided with computer-related issues. He implemented an improved algorithm for the computer calculations that increased speed by almost two orders of magnitude. He also implemented the code for Quantum Monte-Carlo simulations and ran the simulation on the Center for Relativistic Astrophysics cluster, again increasing the speed of the calculations. His ability to automate many different calculations into the code have been beyond what one would expect from a non-computer science student. I would have been totally up a creek without his help. I

also want to thank Brian Rose for all of his help. He was instrumental in reorganizing large parts of the lab space, making the facility safer and more user-friendly. He was also able to talk sports on a limited basis, so bonus points there.

I want to thank my thesis committee for taking the time out of your busy schedule to help me make this document the best that it can be. I hope that I do not make your job too difficult.

My final acknowledgements will be to my family. During my studies, there were one or two occasions when I may have not been as nice as I could have. In terms of cardinal direction / equine similes, I may have been like the south end of a north-bound horse. Also, it appears to be the tendency for physicists to always want to be right, despite definitive proof to the contrary. My family was on the receiving end of a finite number of these instances. Don't get me wrong, they are capable of giving as well as they get, but I thank them for the times they tolerated my giving without retaliation. I am very proud of my daughters, Emily and Gabriella. They are growing up to be strong, confident, intelligent women, and the world be theirs for the taking; spread your wings and fly, my fledgling raptors. Then there is my wife, Natalie. No matter what I say here, it will not even come close to adequately describing how awesome she is. She has put up with so much over the last 17 years of Army life. I won't go so far as to say she has suffered in silence...but nobody is perfect. In all seriousness, she is the best thing that has happened to me, and I am the luckiest man in the world to have her as my wife.

TABLE OF CONTENTS

LIST OF TABLES

LIST OF FIGURES

SUMMARY

The primary study of this thesis is the non-equilibrium dynamics of a quantum inverted pendulum as examined in the collective spin dynamics of a spin-1 Bose-Einstein condensate. The measurements build on the success of previous experiments that studied spin mixing and spin-nematic quadrature squeezing, and improved on the theoretical model used to describe the system evolution. The major contribution of this thesis is the in-depth study and experimental realization of the non-gaussian evolution of a quantum inverted pendulum. Additionally, in order to compare experimental results with the simulation past the low depletion limit, current simulation techniques needed to be extended to model atomic loss. These extensions show that traditional measurements of the system evolution (e.g. the mean and standard deviation of the evolving quantity) were insufficient in capturing the quantum nature of the evolution. It became necessary to look at higher order moments and cumulants of the distributions in order to capture the quantum fluctuations. Extending the implications of the loss model further, it is possible that the system evolves in a way previously unpredicted. Spin-mixing from a hyperbolic fixed point in the phase space and low noise atom counting form the core of the experiment to measure the evolution of the distributions of the spin populations. The evolution of the system is also compared to its classical analogue, the momentum-shortened inverted pendulum. The other experimental study in this thesis is mapping the mean-field phase space. The mean-field phase space consists of different energy contours that are divided into both phase-winding trajectories and closed orbits. These two regions are divided by a separatrix whose orbit has infinite period. Coherent states can be created fairly accurately within the phase space and allowed to evolve freely. The nature of their

subsequent evolution provides the shape of the phase space orbit at that initial condition. From this analysis a prediction of the nature of the entire phase space is possible.

CHAPTER 1

INTRODUCTION

The simple pendulum, like the harmonic oscillator, is an example of a well-known classical system that can be extended to the quantum limit to serve as a model for more complicated systems. In fact, the simple pendulum reduces to the harmonic oscillator for small initial displacements from its equilibrium position. However, the harmonic oscillator approximation for a simple pendulum is not valid for a pendulum prepared in its inverted state. The inverted state of the simple pendulum corresponds to a hyperbolic fixed point in the pendulum's phase space. As the equilibrium position is unstable, any single perturbation to the system will cause the pendulum to fall. The early dynamics of its evolution are extremely sensitive to its initial conditions. In the quantum limit, the precision of the initial preparation of the inverted pendulum is limited by the Heisenberg uncertainty principle, resulting in inevitable evolution regardless of the care of state preparation.

The non-equilibrium dynamics of a quantum inverted pendulum has an important role in a wide range of physical systems, specifically those in which a hyperbolic fixed point is found in the phase space. Though an appropriately-sized quantum inverted pendulum has not been demonstrated, the dynamics can be closely modeled in a spin-1 BEC. This thesis will examine the dynamics of a spin-1 BEC in the regime of a quantum inverted pendulum. This chapter will provide a brief review of the key developments in BEC work over the last nearly twenty years to highlight the distinctive properties of this unique form of matter, and the applicability of the spinor BEC in particular for studying a quantum inverted pendulum.

1.1 Historical Overview of Bose-Einstein Condensates

Since the first Bose-Einstein Condensates (BEC) in dilute atomic gases were observed [1–3], the field of atomic and condensed matter physics has erupted into a plethora of experimental and theoretical work. It was the culmination of over 20 years of work dating back to the 1970s with atomic hydrogen [4, 5] and later with the laser cooling of alkali atoms [6, 7]. Bose-Einstein condensation is a second-order phase transition in which bosons macroscopically occupy the ground state of the trapping potential when the temperature falls below the critical temperature. This is when the inter-particle spacing is less than the thermal de Broglie wavelength of the particles. In terms of the particle density, this can be expressed as $n\lambda_{dB}^3 = 2.612$, where n is the particle density and $\lambda_{dB} = h/\sqrt{2\pi m k_B T}$ is the thermal de Broglie wavelength. The thermal de Broglie wavelength at room temperature is smaller than the size of an atom, and increases as the temperature is reduced. However, in order to prevent normal condensed states (e.g. solid, liquid) as the temperature is lowered, the atoms must be kept at low densities under ultrahigh vacuum. Under these conditions, the atoms need to be cooled to the sub-microKelvin regime in order to undergo Bose-Einstein condensation.

Bose condensed atoms posses identical spatial wavefunctions, and the superposition of these wave functions produces a macroscopic coherent matter wave. The coherent matter wave is the quintessential characteristic of a BEC, and several of the early key experiments were devoted to studying this phenomenon. Coherence in a macroscopic matter wave was first demonstrated by the group at MIT by interfering two independent BEC's [8]. The Munich group performed two different experiments with double-slit interference, one with a BEC and one with a thermal cloud above the BEC transition temperature. The result demonstrated that the BEC had a long-range phase coherence, while the thermal cloud did not [9]. The tunneling of macroscopic

wavefunctions between adjacent potential wells was also demonstrated [10, 11]. Additionally, condensates loaded in 3D lattices have been observed transitioning between the Mott-Insulator phase and the superfluid phase [12], demonstrating phase coherence transference through the tunneling of wavepackets between lattice sites. Another interesting observation was that of an atom laser, where atoms from a Bose condensate are selectively removed from the trapping potential, analogous to coherent optical fields producing lasers [10, 13–15].

For the first five years condensates were created only in magnetic traps. Atoms were laser cooled to the μK temperature, then evaporative cooling was used to bring the atoms below the critical temperature. The use of magnetic traps limited the study of BECs to systems that could be described by a scalar order parameter, $\psi(\vec{r}, t)$ whose dynamics are governed by the Gross-Pitaevskii equation [16]. This trap configuration was adequate for studying the weak inter-atomic interactions that also make atomic BECs unique. These interactions, typically elastic inter-atomic collisions, are necessary for the atoms to reach thermal equilibrium and for evaporative cooling below the critical point. These interactions also affect the ground state and dynamical properties of the BEC [17, 18], and repulsive interactions are required to prevent large condensates from collapsing [19, 20]. Additionally, weak atomic interactions are responsible for the superfluid behavior of the gas such as quantized vortices [21–23] and superfluid sound waves [24–26].

Another trapping technique involves creating a condensate in a magnetic microtrap constructed with lithographically patterned wires on a solid-state chip. Though this technique allows for miniaturization of the BEC set-up and provides the ability to study interactions between ultracold atoms and the chip surface [27, 28], it is still limited in that the use of magnetic trapping limits the study of the internal interactions which will be addressed in the next section.

1.2 Spinor BEC

The use of a magnetic trap for the creation of BECs has limited the experimental work to primarily single species and single component systems. The atoms are confined to one Zeeman sub-level in the ground state hyperfine manifold. Development of trapping methods that were not so limited represented a new avenue of BEC research, extending into multi-species and multi-component systems where coupled, interacting quantum fluids could be explored. Of particular note, spinor condensates, or atomic BECs with internal spin degrees of freedom, offered a new form of coherent matter with internal quantum structures. These BEC systems are related to other macroscopic quantum systems in which internal degrees of freedom play a prominent role [29–34]. The investigations in this thesis build upon previous work in this lab on multi-component spinor condensates confined in optical traps, in which the first ferromagnetic condensate was realized [35], the first quantitative validation of the mean-field theory of spin-1 condensates was provided [34], coherent spin oscillations and coherent control of spinor dynamics were demonstrated [36], and sub-Poissonian fluctuations [37] and spin-nematic quadrature squeezing [38] were observed. The main goal of this thesis is to explore the non-equilibrium dynamics of a quantum inverted pendulum as seen in a spin-1 condensate. The purpose of these explorations is to experimentally measure the intricate quantum nature of the pendulum evolution from both classically stable state and other prepared states.

1.2.1 Spinor BEC Experiments

The first spinor condensates were investigated by experimentalists at MIT using sodium condensates confined in optical traps [39]. Their studies included the observation of spin-mixing in initially excited spin states [32], and the formation and dynamical evolution of spin domains in large extended condensates [40–42]. Based on these observations, it was determined that the spin-1 ^{23}Na condensates demonstrated

anti-ferromagnetic ordering of the spins in low magnetic field, and thus had a positive value for the spinor dynamical energy [32]. These experiments used a magnetic trap to initially trap the atoms, then transferred them to an optical trap.

The first all-optical trapping techniques for creating BECs were developed in our lab using ^{87}Rb [35]. Similar to techniques used in the MIT experiments, the condensate is prepared in the $m_f = 0$ state using a high magnetic field. The magnetic field is quickly lowered (a process called a "quantum quench" [43]) to study the subsequent evolution [34]. The equilibrium populations measured were in good agreement with the phase diagram of the ground states [32] and exhibited the predicted quantum phase transition at the critical value of the magnetic field (relative to the spinor dynamical energy) [34, 43]. The Hamburg group reported similar results for the $f = 2$ manifold, as well [33].

Later work in our lab studied the coherent evolution and control of a spinor system for the first time, providing the first validation of the mean-field theoretical treatment of dynamics [36]. This work demonstrated both low and high field oscillations, as well as control of the spin dynamics through magnetic field pulses to shift the spinor phase. The Hamburg group performed similar work with the $f = 2$ manifold of ^{87}Rb [44, 45], and the group at NIST performed similar work with $f = 1$ ^{23}Na [46].

Spinor condensates also exhibit unique spatial excitations and structures. Spin domains were demonstrated in spinor condensates in several experiments [32, 47]. The Berkeley group observed spontaneous symmetry breaking across the phase transition through measurements of the transverse magnetization using large ^{87}Rb condensates in quasi 2-D extended systems [48]. They also demonstrated that dipolar effects could be observed in the formation of helical spin textures [49]. Other groups have demonstrated the spontaneous breaking of spatial and spin symmetries (Hannover, [50]), skyrmions (Rochester, [51]), and quantum phase transitions in Na (Georgia Tech, [52]).

The previously listed spinor work focused on the mean-field limit, but beyond mean-field explorations have also been conducted. Observations of super-Poissonian noise as a result of vacuum fluctuations was observed by several groups [53–55]. Later, development of low-noise atom detection techniques capable of detecting sub-Poissonian quantum correlations in our and other labs allowed for the observation of sub-Poissonian fluctuations and spin-nematic squeezing [38, 52, 56].

1.2.2 Spinor Theory

As previously discussed, spinor BECs [31, 35, 39, 57] differ from the single-component BECs in that there are internal collisional interactions amongst the atoms that produce interesting dynamics. The small spin dependence of the collisional interaction energy results in an interplay of different atomic spin orientations [29, 30]. Compared to the total interaction energy, the spin dependent interaction energy is small ($\sim 0.5\%$ in ^{87}Rb), and is a manifestation of the difference between the s-wave scattering lengths into the allowed angular momentum channels (See Chapter 2). The sign (positive or negative) of the difference determines the properties of the spin-1 system, ferromagnetic or anti-ferromagnetic. The ground state is determined by a combination of the collective spinor energy and the per-particle energy in a finite magnetic field, which is discussed in more detail in Section 2.5.

One of the consequences of the spin-dependent interactions is a process called spin-mixing, where the spin components can coherently exchange populations. This is when two $m_f = 0$ atoms collide to produce an $m_f = 1$ and an $m_f = -1$ atom. The process is reversible, and magnetization ($M = N_{m_f=1} - N_{m_f=-1}$) is conserved. This process is analogous to optical four-wave mixing whereby two pump photons are converted into two outgoing modes with opposite momenta and frequency shift inside a non-linear crystal with a $\chi^{(3)}$ term [58]. Spin-mixing is the critical component in many of the theoretical investigations for spin-1 condensates, as well as the

experiments discussed earlier.

Theoretical exploration of spinor condensates have taken two main paths: mean-field [59–61] and quantum [62–64]. The mean-field approach has worked well for calculating spatial excitations of the spinor order parameter and for the dynamics of the internal modes of classical states which evolve periodically [60, 63, 65]. However, the mean-field approach breaks down for classically unstable states, such as the pure $m_f = 0$ initial state used in our experiment. The quantum approach captures the evolution of the $m_f = 0$ state.

The quantum approach is also necessary to account for discrepancies with experimental results by investigating the effects of particle number and magnetic fields [66, 67]. Ultimately, through use of the quasi-probability distribution to capture the quantum evolution of the system for the mean-field approach, solid agreement between the two approaches has been shown [58], and either can now be used to compare with experimental results from our lab.

The effects of atomic loss are not incorporated into any current theoretical publications. However, atomic loss is a major factor in our experimental measurements, since the trap lifetime is $\sim$1.8 s and we have made spin-mixing measurements out to 4 s. As a result, a theoretical model for atomic loss was developed in this thesis to allow for comparisons at much later evolution times.

1.3 Thesis Contributions and Organization

This thesis describes two sets of experimental results along with improvements to the theory that are critical to longer time matching of experiment and simulation. The first set of experimental results describe the mapping of the semi-classical phase space of the system. It uses the results of coherent oscillations to effectively map the phase space in two ways. First, the periods of the oscillations are used to locate the separatrix. Second, the coherent oscillations are fitted to simulated results to match the

fractional population to a spinor phase, and these results are used to plot individual energy contours in the phase space. The results provided in this thesis are provided by the current experimental apparatus that has been improved to provide better control than was available to previous students in this lab. Additionally, our understanding of the phase space and state preparation techniques is far more advanced.

The second set of experimental results are the measurements of the non-Gaussian evolution of the spin-1 ferromagnetic ^{87}Rb condensate. This work builds on the work of previous doctoral students. The original all-optical BEC experiment and the flexible control system employed were developed for the thesis work of Dr. Murray Barrett [68]. That system was used by Dr. Ming-Shien Chang for the exploration of coherent spin-mixing [47]. Dr. Chang developed the basic spin-mixing measurement tools and the microwave system used for state manipulation. While measuring the relative number squeezing generated by coherent spin-mixing, Dr. Eva Bookjans [69] developed the low-noise imaging techniques used by our group, along with demonstrating the first use of RF rotations to calibrate atom counting. In Dr. Chris Hamley's thesis, a deeper theoretical understanding of the spin-mixing process demonstrates how spin-nematic squeezing is generated, as well as the development of measurement protocols involving microwaves and RF manipulations combined in new ways to measure states previously unmeasurable. Also, it provided a better conceptual understanding of the phase spaces involved, allowing for development of simulation techniques with accurate initial conditions for $m_f = 0$ condensates in the semi-classical picture. This thesis contributes a detailed experimental realization of the dynamical evolution of a quantum inverted pendulum as explored in a spin-1 BEC. The highly non-Gaussian evolution of the system as predicted by simulation required thousands of data points to obtain statistically reliable results. Additionally, the loss model used for the dynamical simulations provides a first-order correction for atomic loss as a result of finite trap lifetimes.

This thesis is organized into eight chapters, with Chapter 1 being the introduction. Chapter 4 gives a discussion of the simple pendulum and provides insights that will be used in later chapters. Chapter 2 discusses the spinor BEC theory. This includes the development of quantum and mean-field theoretical approaches as exemplified by several of the key papers on the topic. Chapter 3 provides an overview of the dynamical simulation techniques used for comparison with experimental results. Chapter 5 gives a brief description of the experimental apparatus. This has been covered in detail previously, but the key components of the experimental apparatus are discussed again. Chapter 6 prepares states using RF and microwave rotations that are then used to effectively map the phase space. In Chapter 7 the evolution of the system under spin-mixing from a pure $m_f = 0$ initial condition is studied. The probability distributions of the spin populations are measured, and the distributions are characterized by calculating the central moments and cumulants. Chapter 8 explores some of the implications of the loss model. Chapter 9 contains concluding remarks and possible future experiments.

CHAPTER 2

SPINOR BOSE-EINSTEIN CONDENSATE THEORY

This chapter will summarize the key results from earlier papers [29, 30, 60, 62, 63, 65, 70]. Specifically, the literature review will focus on the application of the theory to the evolution of a ferromagnetic ^{87}Rb condensate from the classically stable initial state of $f = 1$, $m_f = 0$. The system can either be left to freely evolve (spin mixing) or be prepared into a specific initial state after the magnetic field quench. Theoretical discussions of spinor condensates have largely fallen into one of two main categories: mean-field or quantum. The mean-field approach results in dynamical equations that do not evolve for an exact $m_f = 0$ condensate. It is possible to extend the mean-field approach by incorporating quantum fluctuations in the initial state [58]. The quantum theory has shown slow immediate evolution with critical dampening leading to the ground state populations [62, 63, 65]. This thesis incorporates a viable loss model to allow simulation comparison with data for longer times. With the inclusion of the loss model, the mean-field and quantum theory more closely match with experimental results at longer times [71], and shows a slow initial evolution followed by under-damped oscillations in the $m_f = 0$ fractional population that is consistent with earlier experiments [34].

2.1 Gross-Pitaevskii Equation

The Gross-Pitaevskii equation is derived from the Hamiltonian for a quantum system of identical bosons by applying the Hartree-Fock approximation and using a pseudo-potential to describe the interaction between particles using the scattering lengths

[16].

$$H = \sum_{i=1}^{N} -\frac{\nabla^2}{2m} + V_T\left(\mathsf{r}_i\right) + U\left(\mathsf{r}_i, \mathsf{r}_j\right). \tag{2.1}$$

For a spinor BEC with spin-1, there are two scattering channels, one for a total spin of $F = 0$ and one for a total spin of $F = 2$. For the low-temperature limit there is only s-wave scattering, and the spin-mixing interaction, $U\left(\mathsf{r}_i, \mathsf{r}_j\right)$, is modeled as a contact pseudo-potential in two body collisions [62, 63, 65]. The interaction between two atoms in a collision is given by [62, 63]:

$$U\left(\mathsf{r}_i, \mathsf{r}_j\right) = \delta\left(\mathsf{r}_i - \mathsf{r}_j\right) \sum_{F=0}^{2} g_F \sum_{M_F=-F}^{F} \left|F, M_F\right\rangle \left\langle F, M_F\right| \tag{2.2}$$

where $g_F = 4\pi\hbar^2 a_F/m$ is the coupling strength of the total spin F channel, a_F is the s-wave scattering length, and m is the particle mass. The scattering channels can be rewritten in terms of the $\left|f = 1, m_f\right\rangle_1 \otimes \left|f = 1, m_f\right\rangle_2$ basis of the colliding atoms as in [62]. The double sum in Eqn. (2.2) then becomes

$$\begin{aligned}
&\sum_{F=0}^{2} g_F \sum_{M_F=-F}^{F} \left|F, M_F\right\rangle \left\langle F, M_F\right| \\
&= g_2(\hat{\Psi}_1^\dagger \hat{\Psi}_1^\dagger \hat{\Psi}_1 \hat{\Psi}_1 + 2\hat{\Psi}_1^\dagger \hat{\Psi}_0^\dagger \hat{\Psi}_1 \hat{\Psi}_0 + \frac{2}{3}\hat{\Psi}_1^\dagger \hat{\Psi}_{-1}^\dagger \hat{\Psi}_1 \hat{\Psi}_{-1} + \frac{2}{3}\hat{\Psi}_0^\dagger \hat{\Psi}_0^\dagger \hat{\Psi}_0 \hat{\Psi}_0 \\
&+ \frac{2}{3}\hat{\Psi}_1^\dagger \hat{\Psi}_{-1}^\dagger \hat{\Psi}_1 \hat{\Psi}_{-1} + \frac{2}{3}\hat{\Psi}_0^\dagger \hat{\Psi}_0^\dagger \hat{\Psi}_1 \hat{\Psi}_{-1} + 2\hat{\Psi}_0^\dagger \hat{\Psi}_{-1}^\dagger \hat{\Psi}_0 \hat{\Psi}_{-1} + \hat{\Psi}_{-1}^\dagger \hat{\Psi}_{-1}^\dagger \hat{\Psi}_{-1} \hat{\Psi}_{-1}) \\
&+ g_0(\frac{4}{3}\hat{\Psi}_1^\dagger \hat{\Psi}_{-1}^\dagger \hat{\Psi}_1 \hat{\Psi}_{-1} + \frac{1}{3}\hat{\Psi}_0^\dagger \hat{\Psi}_0^\dagger \hat{\Psi}_0 \hat{\Psi}_0 - \frac{2}{3}\hat{\Psi}_1^\dagger \hat{\Psi}_{-1}^\dagger \hat{\Psi}_0 \hat{\Psi}_0 - \frac{2}{3}\hat{\Psi}_0^\dagger \hat{\Psi}_0^\dagger \hat{\Psi}_1 \hat{\Psi}_{-1})
\end{aligned} \tag{2.3}$$

where $\Psi_\alpha^\dagger \to \left|f = 1, m_f = \alpha\right\rangle$ has been substituted for brevity. For reasons which will be obvious later, it is useful to rearrange the Hamiltonian (Eqn. (2.1) with Eqn. (2.3)) into symmetric and asymmetric portions. The kinetic energy term of the Hamiltonian is symmetric under exchange of indices, and we will assume that the trapping potential, $V_T(\mathsf{r}_i)$, is also symmetric. The spin-independent part is also symmetric under interchange of indices and has a coupling strength which is the weighted average of the channel strengths ($\lambda_s = (2g_2 + g_0)/3$). The spin-dependent part is asymmetric

under exchange of indices and has a couplling strength that is proportional to the difference of the channel strengths ($\lambda_a = (g_2 - g_0)/3$). The symmetric and asymmetric portions of the Hamiltonian are given by [62]:

$$\mathcal{H}_S = \sum_i \int d^3r \Psi_i^\dagger \left(-\frac{\hbar^2 \nabla^2}{2m} + V_T \right) \Psi_i + \frac{\lambda_s}{2} \sum_{ij} \int d^3r \Psi_i^\dagger \Psi_j^\dagger \Psi_i \Psi_j \tag{2.4}$$

$$\begin{aligned} \mathcal{H}_A = \frac{\lambda_a}{2} \int d^3r \Big(& \Psi_1^\dagger \Psi_1^\dagger \Psi_1 \Psi_1 + \Psi_{-1}^\dagger \Psi_{-1}^\dagger \Psi_{-1} \Psi_{-1} - 2\Psi_1^\dagger \Psi_{-1}^\dagger \Psi_1 \Psi_{-1} \\ & + 2\Psi_1^\dagger \Psi_0^\dagger \Psi_1 \Psi_0 + 2\Psi_{-1}^\dagger \Psi_0^\dagger \Psi_{-1} \Psi_0 + 2\Psi_0^\dagger \Psi_0^\dagger \Psi_1 \Psi_{-1} + 2\Psi_1^\dagger \Psi_{-1}^\dagger \Psi_0 \Psi_0 \Big) \end{aligned} \tag{2.5}$$

The Hamiltonian above can be referred to as the spin-mixing Hamiltonian. The spin-independent symmetric portion (Eqn. (2.4)) will determine the overall spatial and motional wavefunction, while the spin-dependent asymmetric portion (Eqn. (2.5)) allows interchange of hyperfine states during collisions while preserving the overall spin. It is this portion of the Hamiltonian that drives spin-mixing.

2.2 Single Mode Approximation

This thesis seeks to study the internal dynamics of the system without worrying about spin waves, vortices, skyrmions, and the like. Despite having separated the spin-mixing Hamiltonian into two portions, (a spin independent portion that determines the spatial modes and a spin-dependent portion that governs the internal modes) generally speaking, there is nothing prevents energy from being exchanged between the two portions. Fortunately, the strength of the two interactions in the Hamiltonian does provide two length scales for the BEC. The single mode approximation (SMA) takes advantage of these different length scales to remove the complication of energy exchange between the spatial/motional modes and the spin internal modes. The two length scales for the symmetric and anti-symmetric portions of the Hamiltonian are given by the healing lengths $\xi_i = 2\pi\hbar/\sqrt{2m\,|\lambda_i|\,n}$, where n is the density, and the index i is either s or a, for the symmetric or anti-symmetric portion of the

Hamiltonian. For ^{87}Rb and ^{23}Na, $\lambda_s \gg \lambda_a$ making the spin independent length scale much smaller than the spin dependent length scale. Consequently, if one can make a condensate where the density drops to zero in a region smaller than the spin modes can vary, then all of the m_f components will have the same spatial wavefunction. This approximation is what is known as the single mode approximation (SMA). In the previous section we assumed that the trapping potential, V_T, was symmetric with respect to spin. In a shallow, linearly polarized dipole force trap such as the one used in our experiment, the trapping potential is not dependent on the spin component. If the magnetic field gradient is also small such that the overall trapping potential is the same for all three spin components, then the approximation made in the previous section is indeed valid. As a result, one can decouple the spatial structure from the internal dynamics. The symmetric portion of the Hamiltonian will be dominant and will determine the overall spatial wavefunction $\phi(\mathsf{r})$ which is the solution to the mean-field scalar Gross-Pitaevskii equation for $\mathcal{H}_S$ [62]:

$$\left(-\frac{\nabla^2}{2m} + V_T + \lambda_s N|\phi|^2\right)\phi = \mu\phi, \quad \int d^3r|\phi(\mathsf{r})|^2 = 1 \tag{2.6}$$

with μ being the chemical potential. As previously stated, this spatial wavefunction is common to all of the m_f projections. This simplification separates the internal dynamics from the spatial dynamics. These conditions are possible to achieve through the use of cross traps or lattices to tightly confine the condensate in all three dimensions.

For a large number of atoms, the scalar Gross-Pitaevskii equation is typically solved using the Thomas-Fermi approximation. The kinetic energy term is neglected, and Eqn. (2.6) yields $\phi(\mathsf{r}) = \sqrt{\frac{\mu - V_T}{N\lambda_s}}$. For a trapping potential approximated by a three dimensional harmonic oscillator, the chemical potential is given by [47]:

$$\mu = \left(\frac{15\hbar^2 m^{1/2}}{2^{5/2}} N\bar{\omega}\bar{a}\right)^{2/5} \tag{2.7}$$

where $\bar{a} = (2a_2 + a_0)/3$ is the mean scattering length and $\bar{\omega}$ is the geometric mean

of the harmonic oscillator frequencies. The density is given by [47]

$$N|\phi(\mathsf{r})|^2 \approx n_{TF}(\mathsf{r}) = \frac{15N}{8\pi R_1 R_2 R_3} \max\left[1 - \sum_{i=1}^{3} \frac{r_i^2}{R_i^2}, 0\right] \tag{2.8}$$

where $R_i = \sqrt{2\mu/m\omega_i^2}$ are the Thomas-Fermi radii with ω_i the characteristic frequencies of the three dimensional harmonic oscillator potential. It is clear from Eqn. (2.8) that the peak density, then, will be $n_0 = 15N/8\pi R_1 R_2 R_3$.

By approximating the internal modes of the condensate in the SMA as $\hat{\Psi}_\alpha \approx \hat{a}_\alpha \phi(\mathsf{r})$, where $\alpha = 0, \pm 1$, and integrating over the spatial portions, the symmetric and asymmetric portions of the Hamiltonians simplify to [62]:

$$\hat{H}_s = \mu\hat{N} - \lambda_s{}'\hat{N}\left(\hat{N} - 1\right) \tag{2.9}$$

$$\begin{aligned}\hat{H}_a =& \lambda_a{}'\left(\hat{N}_1^2 + \hat{N}_{-1}^2 - 2\hat{N}_1\hat{N}_{-1} + 2\hat{N}_1\hat{N}_0 + 2\hat{N}_{-1}\hat{N}_0\right.\\ &\left. + 2\hat{a}_0^\dagger\hat{a}_0^\dagger\hat{a}_1\hat{a}_{-1} + 2\hat{a}_1^\dagger\hat{a}_{-1}^\dagger\hat{a}_0\hat{a}_0\right).\end{aligned} \tag{2.10}$$

Here $\hat{a}_\alpha$ is the bosonic annihilation operator and follows the usual commutation relation $\left[\hat{a}_\alpha, \hat{a}_\beta^\dagger\right] = \delta_{\alpha\beta}$. Additionally, $2\lambda_i{}' = \lambda_i \int \left|\phi(\mathsf{r})^4\right| d^3r$ and $\hat{N} = \hat{a}_1^\dagger\hat{a}_1 + \hat{a}_0^\dagger\hat{a}_0 + \hat{a}_{-1}^\dagger\hat{a}_{-1}$ are the spatially integrated interaction strength and total number of atoms, respectively. Using the Thomas-Fermi approximation, the density squared integral $\int \left|\phi(\mathsf{r})^4\right| d^3r$ evaluates to $\frac{4}{7}\frac{n_0}{N}$ [47], and as a result the spatially integrated interaction strengths $\lambda_i{}'$ scale with the number of atoms as $N^{-3/5}$. Furthermore, with no atom loss or change in trapping potential one can see that $\hat{H}_s$ is constant, and all of the dynamics happen in $\hat{H}_a$.

The experimental values for some of the different quantities discussed in this section are included in Table 2.1.

Table 2.1: Experimental values of various theoretical quantities.

Symbol	Theoretical Quantity	Value	Units
N	Number of Atoms	$45,000$	atoms
$a_{f=0}$	Spin-0 s-Wave Scattering Length	101.8(2)	Bohr Radii
$a_{f=2}$	Spin-2 s-Wave Scattering Length	100.4(a)	Bohr Radii
ω_i	Trap Frequencies	$2\pi(200, 200, 200)$	rad/s
T_c	Critical Temperature	321	nK
μ	Chemical Potential	1.94764×10^{-30}	Joules
		2939.35	Hz
R_i	Thomas-Fermi Radii	$(4.13, 4.13, 4.13)$	μm
ξ_s	Spin Healing Length	12.71	μm
n_o	Thomas Fermi Peak Density	3.801×10^{14}	cm^{-3}
λ_a'	Inter-Spin Energy	$2\pi(8.61 \times 10^{-5})$	rad/s/atom
c	Spinor Dynamical Rate	$2\pi(7.75)$	rad/s

2.3 Quantum Analysis of the Spin Mixing Hamiltonian

Looking only at the asymmetric spin-mixing Hamiltonian, one can rewrite it in an eigenbasis of angular momentum states [63]:

$$\hat{H}_a = \lambda_a' \left(\hat{S}^2 - 2\hat{N} \right) \tag{2.11}$$

where $\hat{S}^2 = \hat{S}_x^2 + \hat{S}_y^2 + \hat{S}_z^2$, and the second quantized form of the components of the total spin angular momentum are used (See Table A.1). Eqn. (2.11) readily shows that the eigenstates of the spin-mixing Hamiltonian are total spin angular momentum states $|S, M_S\rangle$ with energy:

$$E_S^a = \lambda_a' \left[S(S+1) - 2N \right]. \tag{2.12}$$

At this point it is instructive to examine the ground state of the spin-mixing Hamiltonian. For an anti-ferromagnetic condensate (e.g. ^{23}Na), $\lambda_a' > 0$), the energy is minimized by minimizing S. This happens globally when $S = 0$ $(S = 1)$ for even (odd) N. The resulting m_f values for the ground state are $\langle N_{-1} \rangle = \langle N_0 \rangle = \langle N_1 \rangle = N/3$. Conversely, for a ferromagnetic condensate (e.g. ^{87}Rb), $\lambda_a' < 0$ and the resulting minimum of the energy occurs when S is maximized. The maximum value of S is N, and this state will have $2N+1$ degenerate ground states, one for each value

of the conserved magnetization. For the $M_S = 0$ state, the ground state populations of the m_f states are $\langle N_{-1}\rangle = \langle N_1\rangle = N/4$ and $\langle N_0\rangle = N/2$.

The evolution of an initial state is achieved by first expanding the initial state onto each of the eigenstates and evolving their phases for each eigenvalue $e^{-iE_S^a t/\hbar}$:

$$|\psi(t)\rangle = e^{-i\theta_N(t)} \sum_{S=0}^{N} C_S e^{-i\lambda_a{}' S(S+1)t} |S, M_S\rangle. \tag{2.13}$$

Here, $C_S \equiv \langle\psi(0)|S, M_S\rangle$, and the common part of the eigenvalue due to the atom number has been pulled from the sum, $\theta_N = -2N\lambda_a{}' t/\hbar$. Since Eqn. (2.9) commutes with both N and $\hat{S}_z$, the number of atoms and the magnetization ($M \equiv \langle S_z\rangle = N_{+1} - N_{-1}$) are both conserved.

The common initial state for the experiment has all of atoms in the $m_f = 0$ hyperfine state. We represent this as a Fock state ($|N_1, N_0, N_{-1}\rangle$) where $N_1 = N_{-1} = 0$ and $N_0 = N$. To analyze the evolution, the angular momentum states are expanded into the Fock basis, which are constructed as in [58, 66].

2.4 Mean Field Analysis of the Spin-Mixing Hamiltonian

Another evaluation technique for the spin-mixing Hamiltonian is to use a mean-field approach. In addition to the mean-field approach already used to calculate the spatial modes in the SMA, another mean-field approximation can be used on the internal states. The first step is to derive a set of coupled dynamical equations for $\hat{H}_a$ by using the Heisenberg equation of motion. Substitution of the spin dependent Hamiltonian (Eqn. (2.10)) into the Heisenberg equation of motion for each m_f state gives the coupled equations [58]:

$$i\hbar\frac{\partial\hat{a}_1}{\partial t} = 2\lambda_a{}'\left(\hat{a}_1^\dagger\hat{a}_1\hat{a}_1 - \hat{a}_{-1}^\dagger\hat{a}_1\hat{a}_{-1} + \hat{a}_0^\dagger\hat{a}_1\hat{a}_0 + \hat{a}_{-1}^\dagger\hat{a}_0\hat{a}_0\right) \tag{2.14a}$$

$$i\hbar\frac{\partial\hat{a}_0}{\partial t} = 2\lambda_a{}'\left(\hat{a}_1^\dagger\hat{a}_1\hat{a}_0 + \hat{a}_{-1}^\dagger\hat{a}_0\hat{a}_{-1} + \hat{a}_0^\dagger\hat{a}_1\hat{a}_{-1}\right) \tag{2.14b}$$

$$i\hbar\frac{\partial\hat{a}_{-1}}{\partial t} = 2\lambda_a{}'\left(\hat{a}_{-1}^\dagger\hat{a}_{-1}\hat{a}_{-1} - \hat{a}_1^\dagger\hat{a}_1\hat{a}_{-1} + \hat{a}_0^\dagger\hat{a}_0\hat{a}_{-1} + \hat{a}_1^\dagger\hat{a}_0\hat{a}_0\right). \tag{2.14c}$$

The mean field approximation can be made when there a large number of atoms. In this limit, the quantum fluctuations can be ignored, and the field operators can be replaced with complex numbers to represent the classical field amplitudes and phases of the internal modes: ($\hat{a}_\alpha \to \sqrt{N}\zeta_\alpha$, $\hat{a}_\alpha^\dagger \to \sqrt{N}\zeta_\alpha^*$ with $\zeta_\alpha = |\zeta_\alpha| e^{i\theta_\alpha}$ and $\sum_\alpha \zeta_\alpha^*\zeta_\alpha = 1$). This approximation yields the dynamical equations

$$i\hbar\dot{\zeta}_1 = c\left[(\rho_1 + \rho_0 - \rho_{-1})\,\zeta_1 + \zeta_0^2\zeta_{-1}^*\right] \tag{2.15a}$$

$$i\hbar\dot{\zeta}_0 = c\left[(\rho_1 + \rho_{-1})\,\zeta_0 + 2\zeta_1\zeta_{-1}\zeta_0^*\right] \tag{2.15b}$$

$$i\hbar\dot{\zeta}_{-1} = c\left[(\rho_{-1} + \rho_0 - \rho_1)\,\zeta_{-1} + \zeta_0^2\zeta_1^*\right] \tag{2.15c}$$

where $c = 2\lambda_a{}'N$ and $\rho_i = |\zeta_i|^2 = N_i/N$ are the fractional populations.

It is useful to attempt to reduce the number of parameters for the mean-field dynamical equations. In general, the three complex numbers representing the classical fields for the three components,

$$\psi = (\zeta_1, \zeta_0, \zeta_{-1})^T,$$

have six parameters. However, the constraint that $\sum_\alpha \zeta_\alpha^*\zeta_\alpha = 1$ reduces the number of parameters to four. Going one step further, one can re-parameterize using $\zeta_1 = \sqrt{\frac{1-\rho_0+m}{2}}e^{i\chi_+}$, $\zeta_0 = \sqrt{\rho_0}$, and $\zeta_{-1} = \sqrt{\frac{1-\rho_0-m}{2}}e^{i\chi_-}$, (where $\chi_\pm = \theta_\pm - \theta_0 = \frac{\theta_s \pm \theta_m}{2}$, and $m = (N_1 - N_{-1})/N$). The phase combinations $\theta_s = \theta_+ + \theta_- - 2\theta_0$ and $\theta_m = \theta_+ - \theta_-$ are called the spinor phase and magnetization phase, respectively. What makes this parameterization useful is that the mean field spinor energy depends on the spinor phase but not the magnetization phase. Taking advantage of this fact, and changing to a rotating frame to remove the magnetization phase ($\zeta_{\pm1}{}' \to e^{\mp\theta_m/2}\,\zeta_{\pm1}$) [58], the equations simplify to just two dynamical variables, ρ_0 and θ_s:

$$\dot{\rho}_0 = \frac{2c}{\hbar}\rho_0\left(\sqrt{(1-\rho_0)^2 - m^2}\right)\sin\theta_s \tag{2.16a}$$

$$\dot{\theta}_s = \frac{2c}{\hbar}\left[(1-2\rho_0) + \frac{(1-\rho_0)(1-2\rho_0) - m^2}{\sqrt{(1-\rho_0)^2 - m^2}}\cos\theta_s\right] \tag{2.16b}$$

These dynamical equations are identifiable as being that of a momentum-shortened pendulum [60], where the length of the pendulum is not fixed. By making the same mean field substitutions into Eqn. (2.10) one can readily obtain the mean-field spinor energy functional per particle (it is necessary to divide through by N):

$$\mathcal{E} = \frac{c}{2}m^2 + c\rho_0\left[(1-\rho_0) + \sqrt{(1-\rho_0)^2 - m^2}\cos\theta_s\right] \tag{2.17}$$

It is interesting to note that Eqn. (2.16) could have been obtained using the Hamiltonian equations of motion, $\dot{\rho}_0 = -\frac{2}{\hbar}\frac{\partial \mathrm{E}}{\partial \theta_s}$ and $\dot{\theta}_s = \frac{2}{\hbar}\frac{\partial \mathrm{E}}{\partial \rho_0}$. This demonstrates that ρ_0 and θ_s are canonically conjugate variables. There are two additional canonically conjugate variables, m and θ_m, but since the energy functional does not depend on θ_m, $\dot{m} = 0$, meaning that magnetization is conserved [65, 72].

As with the quantum Hamiltonian, it is instructional to identify the ground states for the mean-field energy functional. For the anti-ferromagnetic ground states ($c > 0$), the ground states are when $m = 0$ and either $\theta_s = \pm\pi$ or $\rho_0 = 0, 1$. This ground state does not lend itself to direct comparison to the quantum ground state for the anti-ferromagnetic case. For the ferromagnetic ground states ($c < 0$), the energy functional is minimized when $\theta_s = 0$ and $\rho_0 = (1-m^2)/2$. For $m = 0$ it is clear that the ground state populations for the mean-field energy functional are the same as for the quantum Hamiltonian. The solutions to the mean-field dynamical equations are oscillatory in nature, similar to experimental results. However, what is not seen with the mean-field solutions is the apparent dampening that the experiment shows. A general solution using Jacobian elliptic functions can be found in Ref. [60]. For the ferromagnetic system, the period is dependent on the displacement from the ground state. For small displacements from the ground state, the period is approximately $T \approx 1/(2\,|c|)$. As stated previously, the experiment is often initialized in the $m_f = 0$ state where $\zeta_{\pm 1} = 0$ and $\zeta_0 = 1$. Inspection of Eqn. (2.15) shows that the time derivatives for this initial state are all zero, and hence the pure $m_f = 0$ state does not evolve from the mean-field equations. This is obviously in conflict with the quantum

simulation and the experimental measurements. It is for this reason that a quasi-probability distribution of initial states that replicate the Fock state $|0, N, 0\rangle$ must be used in order for the mean-field to recover the quantum solution [58].

2.5 Magnetic Fields

Thus far, the effects of magnetic fields have been neglected. The Zeeman energies are found using the well-known Breit-Rabi formula for the hyperfine ground states [73]. This formula is expanded into a power series giving the linear Zeeman effect and a quadratic Zeeman effect for low fields. Furthermore, in the SMA, only the energy difference of the m_f states affects dynamics [58]. This energy difference is given by $E_\alpha - E_0 = p\alpha + q\alpha^2$, where $\alpha = \pm 1$, $p = \mu_B B_z g_f$ is the linear Zeeman contribution, $q = \mu_B^2 B_z^2/(\hbar^2 E_{HFS})$ is the quadratic Zeeman contribution, g_f is the Landé g-factor, and E_{HFS} is the ground state hyperfine splitting [63, 64, 74]. The total magnetic field energy to second order is given by

$$\begin{aligned} E_B &= E_1 N_1 + E_0 N_0 + E_{-1} N_{-1} \\ &= E_1 N_1 + E_0 \left(N - (N_1 + N_{-1})\right) + E_{-1} N_{-1} \\ &= (p+q) N_1 + (-p+q) N_{-1} + E_0 N \\ &= p\left(N_1 - N_{-1}\right) + q\left(N_1 + N_{-1}\right) + E_0 N \end{aligned} \tag{2.18}$$

The first term in Eqn. (2.18) shows that the linear Zeeman shift is proportional to $S_z = (N_1 - N_{-1})$, where each atom contributes an energy of pm_f. What is less obvious is the contribution of the quadratic Zeeman effect. Here it is convenient to introduce the spin-1 quadrupole operators. Table A.2 shows the spin-1 quadrupole operators in both matrix form and in terms of the bosonic operators for the different m_f states. The matrix form of the operators are in a spherical polar basis.

The quadrupole operator Q_{zz} can be easily rewritten in terms of the m_f component

populations:

$$\begin{aligned}\frac{Q_{zz}}{2} &= \tfrac{1}{3}N_1 + \tfrac{1}{3}N_{-1} - \tfrac{2}{3}N_0 \\ &= \tfrac{1}{3}\left(N_1 + N_{-1}\right) - \tfrac{2}{3}\left(N - N_1 - N_{-1}\right) \\ &= \left(N_1 + N_{-1}\right) - \tfrac{2}{3}N \end{aligned} \tag{2.19}$$

One can neglect the constant term at the end of Eqn. (2.19), along with the constant term at the end of Eqn. (2.18), since they do not affect the dynamics. The resulting magnetic field energy contribution to the Hamiltonian, neglecting the constant terms, is $E_B = pS_z + \frac{q}{2}Q_{zz}$.

2.5.1 Quantum Approach with Finite Magnetic Field

The spin-mixing Hamiltonian, then, for a single mode, spin-1 condensate in a finite magnetic field takes the basis independent form

$$\hat{H}_{a,B} = \lambda_a{}' \left(\hat{S}^2 - 2\hat{N}\right) + p\hat{S}_z + \frac{q}{2}\hat{Q}_{zz}. \tag{2.20}$$

The choice of basis now becomes important. S_z commutes with the entire Hamiltonian, but $\hat{Q}_{zz}$ and $\hat{S}^2$ do not commute. This complication makes it difficult to solve the evolution using the angular momentum formulation. However, Fock states are eigenstates of both S_z and $\hat{Q}_{zz}$. Additionally, the angular momentum basis has already been projected onto the Fock basis [66].

As an alternative, the spin-mixing Hamiltonian (Eqn. (2.20)) can be evaluated using techniques provided in Refs. [64, 67, 75], which provides a Fock state basis as a number of pairs of $m_f = \pm 1$ in a vacuum state of atoms with $m_f = 0$. A Fock state can be enumerated as $|N_1, N_0, N_{-1}\rangle$ as was discussed earlier. However, an equivalent enumeration is $|N, M, k\rangle$, where $N = N_1 + N_0 + N_{-1}$ is the total atom number, $M = N_1 - N_{-1}$ is the magnetization, and k is the number of pairs of ± 1 atoms. Since the spin-mixing Hamiltonian conserves total number, N, and magnetization, M, the only evolution for this basis will be in k. In this basis the spin-mixing Hamiltonian acts

as a hopping Hamiltonian, jumping between numbers of pairs and can be represented by a tri-diagonal matrix [38]. Eqn. (2.10) can be rearranged by taking advantage of the bosonic operator commutation relationships, thus pairing mode operators into number operators. The result is

$$\hat{H}_a = \lambda_a{}' \left(\left(\hat{N}_1 - \hat{N}_{-1} \right)^2 + \left(2\hat{N}_0 - 1 \right) \left(\hat{N}_1 + \hat{N}_{-1} \right) + 2\hat{a}_1^\dagger \hat{a}_{-1}^\dagger \hat{a}_0 \hat{a}_0 + 2\hat{a}_0^\dagger \hat{a}_0^\dagger \hat{a}_1 \hat{a}_{-1} \right). \tag{2.21}$$

With this change, adding the effects of a finite magnetic field is not difficult since it is diagonal in this basis. As Eqn. (2.18) indicates (after taking the E_0 as the zero point for the quadratic Zeeman energy), the magnetic field contribution to $\hat{H}_a$ is $p\left(\hat{N}_1 - \hat{N}_{-1}\right) + q\left(\hat{N}_1 + \hat{N}_{-1}\right)$. For $M_L = 0$ the spin-mixing Hamiltonian with a finite magnetic field can be evaluated for numbers of pairs, yielding the following matrix elements [38, 64]:

$$\begin{aligned} \tilde{H}_{k,k'} = & \left\{ 2\lambda_a{}' \left(2\left(N - 2k \right) - 1 \right) + 2qk \right\} \delta_{k,k'} \\ & + 2\lambda_a{}' \Big\{ \left(k' + 1 \right) \sqrt{\left(N - 2k' \right) \left(N - 2k' - 1 \right)}\, \delta_{k,k'+1} \\ & + k' \sqrt{\left(N - 2k' + 1 \right) \left(N - 2k' + 2 \right)} \delta_{k,k'-1} \Big\}. \end{aligned} \tag{2.22}$$

For $q = 0$ Eqn. (2.22) takes the form of the matrix elements for Eqn. (2.12), and the eigenvalues are the same for both. The eigenvectors are the angular momentum states projected onto the Fock basis as described earlier, and the exact solution follows rather trivially. For $q \neq 0$ the eigenstates are a mix between the angular momentum basis and the Fock pairs basis, and the matrix elements of Eqn. (2.22) can be diagonalized to get an exact solution [67]. The eigenspectrum for both ferromagnetic and anti-ferromagnetic condensates can be seen in Ref. [38]. For low magnetic fields the eigenenergies vary quadratically with index because the eigenstates are angular momentum states. On the other hand, the eigenenergies vary linearly with index for high magnetic field because the eigenstates are Fock states. The ground state in high magnetic field is the lowest energy eigenstates of Q_{zz}, which is the $|0, N, 0\rangle$ Fock state

equivalent to the $m_f = 0$ polar state, regardless of the sign of ${\lambda_a}'$ [59].

2.5.2 Mean-Field Equations with a Finite Magnetic Field

The mean field dynamical equations (Eqn. (2.15)) are easily modified to include a finite magnetic field:

$$i\hbar\dot{\zeta_1} = E_1\zeta_1 + c\left[\left(\rho_1 + \rho_0 - \rho_{-1}\right)\zeta_1 + \zeta_0^2\zeta_{-1}^*\right] \tag{2.23a}$$

$$i\hbar\dot{\zeta_0} = E_0\zeta_0 + c\left[\left(\rho_1 + \rho_{-1}\right)\zeta_0 + 2\zeta_1\zeta_{-1}\zeta_0^*\right] \tag{2.23b}$$

$$i\hbar\dot{\zeta_{-1}} = E_{-1}\zeta_{-1} + c\left[\left(\rho_{-1} + \rho_0 - \rho_1\right)\zeta_{-1} + \zeta_0^2\zeta_1^*\right]. \tag{2.23c}$$

With the same parameterization and change of variables as before, the simplified dynamical equations become

$$\dot{\rho}_0 = \frac{2c}{\hbar}\rho_0\left(\sqrt{\left(1-\rho_0\right)^2 - m^2}\right)\sin\theta_s \tag{2.24a}$$

$$\dot{\theta}_s = -\frac{2q}{\hbar} + \frac{2c}{\hbar}\left[\left(1-2\rho_0\right) + \frac{\left(1-\rho_0\right)\left(1-2\rho_0\right) - m^2}{\sqrt{\left(1-\rho_0\right)^2 - m^2}}\cos\theta_s\right]. \tag{2.24b}$$

The energy functional takes the form

$$\mathcal{E} = \frac{c}{2}m^2 + c\rho_0\left[\left(1-\rho_0\right) + \sqrt{\left(1-\rho_0\right)^2 - m^2}\cos\theta_s\right] + pm + q\left(1-\rho_0\right) \tag{2.25}$$

The dynamical equations developed in Sections 2.5.1 and 2.5.2 will be further examined in Chapter 3.

2.5.3 Mean-Field and Spin-Nematic Phase Spaces

The system can be represented in the spin-nematic phase space using the operators of Tables A.1 and A.2. The mean-field energy functional of Eqn. (2.25) can be re-written as:

$$\mathcal{E} = \frac{c}{4}\left(1-x^2\right)\left(1+\cos\theta_s\right) + \frac{q}{2}\left(1-x\right) \tag{2.26}$$

where $x = 2\rho_0 - 1$. Because of the added complexity that a finite magnetic field adds, only $m = 0$ is considered.

Furthermore, the expectation value for several of the spin and quadrupole operators can be calculated using the matrix representation of Tables A.1 and A.2 and the parameterizations of order parameter $\psi = (\zeta_1, \zeta_0, \zeta_{-1})^T$ from Section 2.4:

$$\begin{aligned}
\langle S_x \rangle &= 2\sqrt{\rho_0(1-\rho_0)}\cos\frac{\theta_s}{2}\cos\frac{\theta_m}{2} \\
\langle Q_{yz} \rangle &= 2\sqrt{\rho_0(1-\rho_0)}\sin\frac{\theta_s}{2}\cos\frac{\theta_m}{2} \\
\langle S_y \rangle &= -2\sqrt{\rho_0(1-\rho_0)}\cos\frac{\theta_s}{2}\sin\frac{\theta_m}{2} \\
\langle Q_{xz} \rangle &= -2\sqrt{\rho_0(1-\rho_0)}\sin\frac{\theta_s}{2}\sin\frac{\theta_m}{2}.
\end{aligned}$$

where all of the values range from $-1 \to 1$. For convenience, the expectation values with subscripts x and y can be combined into expectation values that are perpendicular to the z operators:

$$\begin{aligned}
\langle S_\perp \rangle^2 = \langle S_x \rangle^2 + \langle S_y \rangle^2 &= 4\rho_0\left(1-\rho_0\right)\cos^2\frac{\theta_s}{2} \\
&= 2\rho_0\left(1-\rho_0\right)\left(1+\cos\theta_s\right) \\
&= \frac{1}{2}\left(1-x^2\right)\left(1+\cos\theta_s\right)
\end{aligned}$$

$$\begin{aligned}
\langle Q_{\perp z} \rangle^2 = \langle Q_{xz} \rangle^2 + \langle Q_{yz} \rangle^2 &= 4\rho_0\left(1-\rho_0\right)\sin^2\frac{\theta_s}{2} \\
&= 2\rho_0\left(1-\rho_0\right)\left(1-\cos\theta_s\right) \\
&= \frac{1}{2}\left(1-x^2\right)\left(1-\cos\theta_s\right)
\end{aligned}$$

and, as a result

$$\langle S_\perp \rangle^2 + \langle Q_\perp \rangle^2 + x^2 = 1.$$

The energy functional can be rewritten in terms of these new expectation values:

$$\mathcal{E} = \frac{c}{2}\langle S_\perp \rangle^2 + \frac{q}{2}(1-x).$$

The spin-nematic phase space can be represented as a sphere with energy contours given by the energy functional, similar to Refs. [38, 58], where x takes the place of Q_{zz}. Fig. 2.1 shows the ferromagnetic mean-field and spin-nematic $m = 0$ phase space for several different values of magnetic field energy.

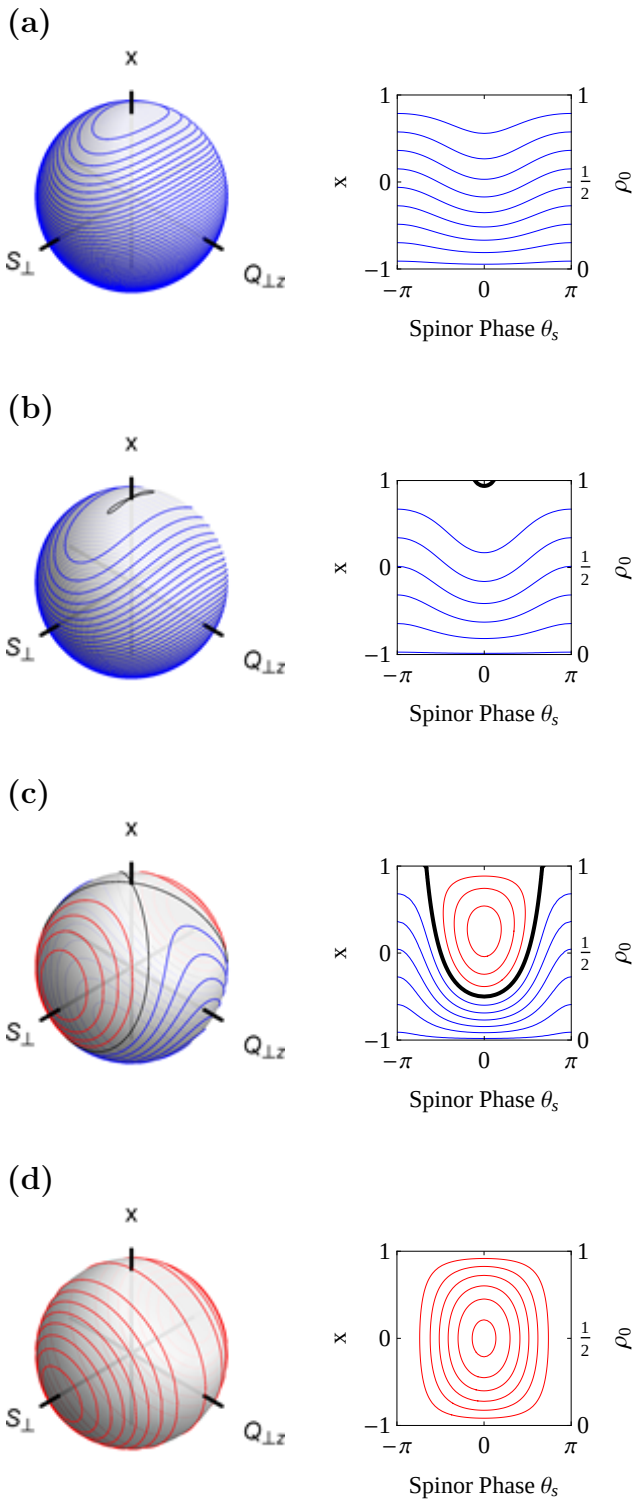

Figure 2.1: Mean-field and spin-nematic phase space in a finite magnetic field for a ferromagnetic condensate. Magnetic field energy q is $|3c|$, $|2c|$, $\frac{|c|}{2}$, and 0 in **(a)**−**(d)**, respectively. The mean-field phase space represents a Mercator projection of one hemisphere of the spin-nematic phase space.

2.6 Quantum Phase Transition in a Quenched ^{87}Rb BEC

In nature, phase transitions of many kinds are associated with changes in the thermodynamic properties of matter, such as temperature, pressure, etc. Indeed, quantum many-body systems such as a Bose gas undergoes a thermodynamic phase transition during evaporative cooling leading to Bose-Einstein condensation[76]. At zero temperature, however, these phase transitions no longer occur. Instead, there are quantum phase transitions (QPT). A quantum phase transition is a change in the *character of a system's ground state* which occurs as some parameter of its Hamiltonian passes critical value [76–78]. In Sections 2.5.1 and 2.5.2 the addition of a finite magnetic field in the quantum and mean-field Hamiltonian made the ground state conditional upon the value of the magnetic field. This phenomenon will be briefly explained in more detail here.

The ground state phase is a result of the competition between the ferromagnetic energy, $E = \lambda_a' \hat{S}^2 = \frac{c}{2N}\hat{S}^2$, and the quadratic Zeeman interaction, $E_q = q\hat{Q}_{zz}$ [76]. At high magnetic fields, the Hamiltonian of multi-component fluids such as the ^{87}Rb condensate are dominated by the quadratic Zeeman energy, favoring the polar state of $m_f = 0$, or $|\psi_{GS}|^2 = (0, 1, 0)^T$ as the ground state. Conversely, at low fields the fluids are characterized by a contact interaction that favors a ferromagnetic phase. [79]

Fig. 2.1 shows the quantum phase transition using the spin-nematic and mean-field phase spaces as the magnetic field is quenched through the critical point. As the magnetic field is decreased for the $m = 0$ ferromagnetic condensate, the ground state goes from the pure polar state of $m_f = 0$ to a mixed ferromagnetic state (a state that involves the $m_f = \pm 1$ Zeeman sub-levels). When the decreasing field reaches the critical value($q_c = 2|c|$), the separatrix first appears, signifying the change in the ground state (Fig. 2.1 (b)). For values above q_c the quadratic Zeeman energy dominates, while below q_c the collisional interactions are dominant, resulting in a

grounds state of $|\psi_{GS}|^2 = (\frac{1}{4} - \frac{q}{8|c|}, \frac{1}{2} + \frac{q}{4|c|}, \frac{1}{4} - \frac{q}{8|c|})^T$.

During the conduct of the experiment the system is initialized at high field and rapidly quenched through the phase transition point. The ground state of the high field preparation is a hyperbolic fixed point in the phase space of the low-field system, and evolves analogous to the evolution of the simple pendulum studied in Chapter 4. Other publications have studied various facets of the dynamics of a quenched spinor condensate such as spontaneous symmetry breaking, formation of spin textures, ferromagnetic domains, and magnetization fluctuations [43, 48, 76, 77]. This thesis will instead study the evolution of the Fock state coefficients of the condensate.

CHAPTER 3

DYNAMIC SIMULATIONS

The equations developed in Chapter 2 provide the necessary tools to simulate the experiment and to make predictions, both qualitative and quantitative, about the experimental results. This chapter will discuss the details of the dynamical simulations, including the mathematical methods of evolving the dynamical equations, the nature of the initial conditions, the method used for modeling loss, and the general predictions about experimental results. Rather than dedicating equal time to ferromagnetic and anti-ferromagnetic condensates, this chapter will spend much of its time using the conditions that are relevant to the experiment, to wit: a $\sim 40,000$ atom ^{87}Rb (ferromagnetic) condensate initialized to the $m_f = 0$ state in a high magnetic field (~ 2G) and quenched to a final magnetic field value of approximately 200 mG. Though this system has been shown to generate squeezing in the low-depletion limit for early time [38], this chapter will not discuss the squeezing in any detail. Instead, this chapter will focus on dynamics well past the low depletion limit. These simulations will be used in the following chapters for comparison of experimental results and for the illustration of conceptual results. The fully quantum simulations of the dynamical equations developed in Section 2.5.1 will be used for comparison of all experimental output, while the mean-field simulations of the dynamical equations developed in Section 2.5.2 will be used to illustrate the conceptual results. All simulations in this chapter, unless specifically noted, use the same parameters as the experiment, and are numerically integrated using a fourth-order Runge-Kutta technique.

3.1 Quantum Dynamical Simulations

The quantum Hamiltonian in the pairs basis given by Eqn. (2.22) could be diagonalized, finding the eigenenergies and eigenvectors to yield exact solutions [66, 67]. However, this method is impractical for a large number of atoms. An advantage of this Hamiltonian, though, is that it is simple to numerically integrate the Schrödinger equation for the initial state using the tri-diagonal matrix without ever solving the exact eigenvalue problem. This method also adds the ability to include a time-varying magnetic field, which is the case for the experiment. The simulation for the state ψ is represented as a vector of the complex coefficients of the Fock states starting with $\psi_0 = 1$ and all other $\psi_{k\neq 0} = 0$ as the initial $m_f = 0$ state. The Schrödinger equation is numerically integrated using Eqn. (2.22) for $\tilde{H}$:

$$\dot{\psi}(t) = \frac{i}{\hbar}\tilde{H}\cdot\psi(t) \tag{3.1a}$$

$$\begin{pmatrix} \dot{\psi}_0 \\ \dot{\psi}_1 \\ \vdots \\ \dot{\psi}_k \\ \vdots \\ \dot{\psi}_{k_{\max}} \end{pmatrix} = \begin{pmatrix} \tilde{H}_{00}\cdot\psi_0 + \tilde{H}_{01}\cdot\psi_1 \\ \tilde{H}_{10}\cdot\psi_0 + \tilde{H}_{11}\cdot\psi_1 + \tilde{H}_{12}\cdot\psi_2 \\ \vdots \\ \tilde{H}_{k(k-1)}\cdot\psi_{k-1} + \tilde{H}_{kk}\cdot\psi_k + \tilde{H}_{k(k+1)}\cdot\psi_{k+1} \\ \vdots \\ \tilde{H}_{k_{\max}(k_{\max}-1)}\cdot\psi_{k_{\max}-1} + \tilde{H}_{k_{\max}k_{\max}}\cdot\psi_{k_{\max}} \end{pmatrix} \tag{3.1b}$$

$$\psi(t+\Delta t) = \psi(t) + \Delta t\cdot\dot{\psi}(t) \tag{3.1c}$$

The Schrödinger equation is iterated as many times as needed to achieve the desired evolution time.

3.1.1 Mean-Field Dynamical Equations

The quantum dynamical simulations discussed in the previous section yield the means of comparing the experimental data to the theory, and generally speaking they provide all of the experimentally obtainable values for comparison. However, what the

quantum simulations do not provide is an intuitive means of analyzing the phase space that the mean-field dynamical equations provide. As was seen in Chapter 4, visualizing the evolution of the system overlaid on the phase space was quite illustrative. However, as was previously mentioned, these mean-field dynamical equations for a classically unstable state such as a pure $m_f = 0$ state will not evolve. As will be seen in Chapter 4, where a quasi-probability distribution is chosen to replicate a quantum-like pendulum evolution, a similar technique can be used to initialize the mean-field dynamical equations such that evolution will occur. This is a common technique used in quantum optics [80], where a distribution of classical states is created and the mean-field dynamics are calculated for each state. In the case of Chapter 4, the distribution will be a simple Gaussian centered on the hyperbolic fixed point. For a spin-1 ferromagnetic condensate initialized in the $m_f = 1$ hyperfine state, the distribution is less straight forward.

3.1.1.1 Quasi-Probability Distribution for Mean-Field Dynamics

The quasi-probability distribution is obtained using the techniques found in [58], which will be highlighted here. In general, the product of two variances of operators $\hat{A}$ and $\hat{B}$ is given by the familiar relationship $\langle(\Delta\hat{A})^2\rangle\langle(\Delta\hat{B})^2\rangle \geq \frac{1}{4}|[\hat{A},\hat{B}]|^2$. Using an initial Fock state of $|0,N,0\rangle$ and Table A.3, only two pairs of operators have a non-zero expectation value of their commutator: $\langle 0,N,0|\,[S_x,Q_{yz}]\,|0,N,0\rangle = -2iN$ and $\langle 0,N,0|\,[S_y,Q_{xz}]\,|0,N,0\rangle = -2iN$. The product relationship for the variances of each is, then, $\langle(\Delta\hat{S}_x)^2\rangle\langle(\Delta\hat{Q}_{yz})^2\rangle \geq N^2$ and $\langle(\Delta\hat{S}_y)^2\rangle\langle(\Delta\hat{Q}_{xz})^2\rangle \geq N^2$. For the uncorrelated initial state, the variance is split equally between each of the operator pairs. Furthermore, the expectation value for each operator is zero for the $m_f = 0$ state. Therefore, normal distributions for S_x, S_y, Q_{yz}, and Q_{xz} are generated that meet these criteria, where S_x, S_y, Q_{yz}, and Q_{xz} are scaled by the number of atoms. These are then used to generate a quasi-probability distribution (QPD) of the classical

field variables ρ_0, m, χ_+, and χ_- that are needed for the semi-classical simulations. Using $\psi = \left(\sqrt{\rho_1}e^{i\chi_+}, \sqrt{\rho_0}, \sqrt{\rho_{-1}}e^{i\chi_-}\right)^T$, and the matrix form of the operators in Table A.1 and Table A.2, the expectation values in terms of the classical field variables can be derived. These equations can be inverted and used to obtain the initial values of the vector order parameter from the uncorrelated distributions of S_x, S_y, Q_{yz}, and Q_{xz}:

$$\chi_+ = \tan^{-1}\left(-\frac{S_y + Q_{yz}}{S_x + Q_{xz}}\right) \tag{3.2}$$

$$\chi_- = \tan^{-1}\left(\frac{S_y - Q_{yz}}{S_x - Q_{xz}}\right) \tag{3.3}$$

$$\rho_0 = \frac{1}{2} + \sqrt{\frac{1}{4} - \frac{1}{8}\left(\left(\frac{S_x + Q_{xz}}{\cos\chi_+}\right)^2 + \left(\frac{S_x - Q_{xz}}{\cos\chi_-}\right)^2\right)} \tag{3.4}$$

$$m = \frac{1}{8\rho_0}\left(\left(\frac{S_x + Q_{xz}}{\cos\chi_+}\right)^2 - \left(\frac{S_x - Q_{xz}}{\cos\chi_-}\right)^2\right) \tag{3.5}$$

These different values of ρ_0, m, χ_+, and χ_- are used in the dynamical equations to show the evolution of each set of initial conditions.

3.1.2 Convergence of the Quantum and Mean-Field Approaches

The quantum and mean-field dynamical simulations are compared in Fig. 3.1. The simulations in Fig. 3.1 were conducted using conditions expected in the experiment: $45,000$ atoms initialized in the $m_f = 0$ at a magnetic field of 2 G. The system is quenched at $t = 0$ by rapidly decreasing the magnetic field from its initial value to its final value of $\sim$ 200 mG with a decay constant of $\tau_B = 1$ ms. The spinor dynamical rate for the two simulations was also chosen to match experimental conditions, $c = -2\pi\hbar \times 7.5$ Hz. The red line represents the mean value of $\langle\hat{N}_0\rangle/N$ (or ρ_0, interchangeably) and the shaded regions represent the standard deviation. Initial inspection of the two results show very good agreement. In fact, closer analysis shows that the two results differ by $< 0.5\%$ for the mean and $< 1\%$ for the standard deviation. This deviation is likely due to the finite number of samples used in the

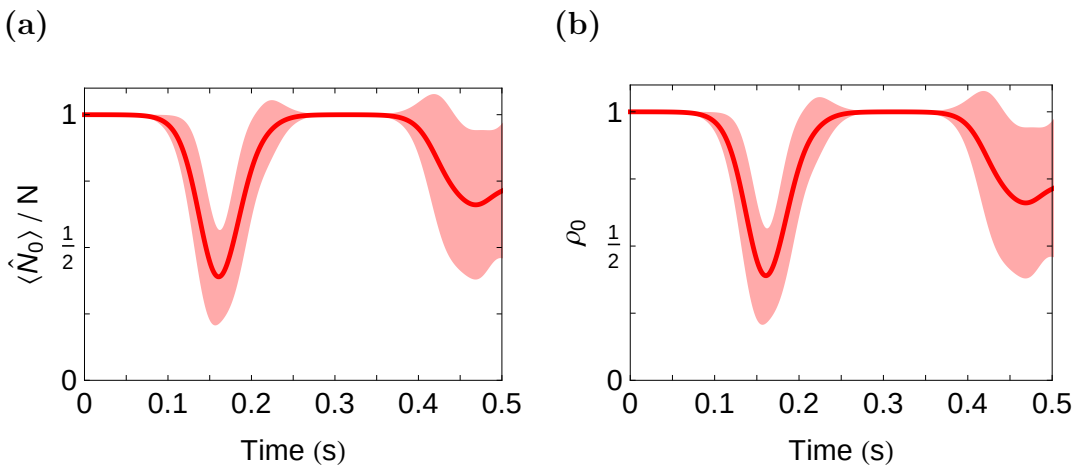

Figure 3.1: Comparison of the quantum and semi-classical simulations. Shown here are the mean (solid red line) and standard deviation (shaded region) of $\langle \hat{N}_0 \rangle / N$ for the (a) quantum simulation and ρ_0 for the (b) semi-classical simulation.

ensemble for the semi-classical simulation (5000).

3.1.3 Effects of Magnetic Field on Evolution

In Chapter 2, two different sets of dynamical equations were derived, one for the absence of a field (Eqn. (2.11)), and one for the presence of a finite magnetic field (Eqn. (2.20)). The results of simulations of each Hamiltonian are shown in Fig. 3.2. The no-field simulations (left column) show an almost immediate evolution out of the $m_f = 0$ initial state. The evolution reaches a single minimum, then gradually climbs to the equilibrium value. The results of the evolution with a finite magnetic field (right column) show a major change in the dynamics for a magnetic field of 200 mG. Initially the population evolves slowly, as in the zero-field case. However, near 200 ms rapid population dynamics occur with one oscillation followed by seemingly damped oscillations. For higher fields, the onset of oscillation would occur sooner, and the depth of the oscillation would be reduced. At $q = 2|c|$, the evolution would show no oscillation since that is the value of the critical point where the ground state of the system changes to the polar state.

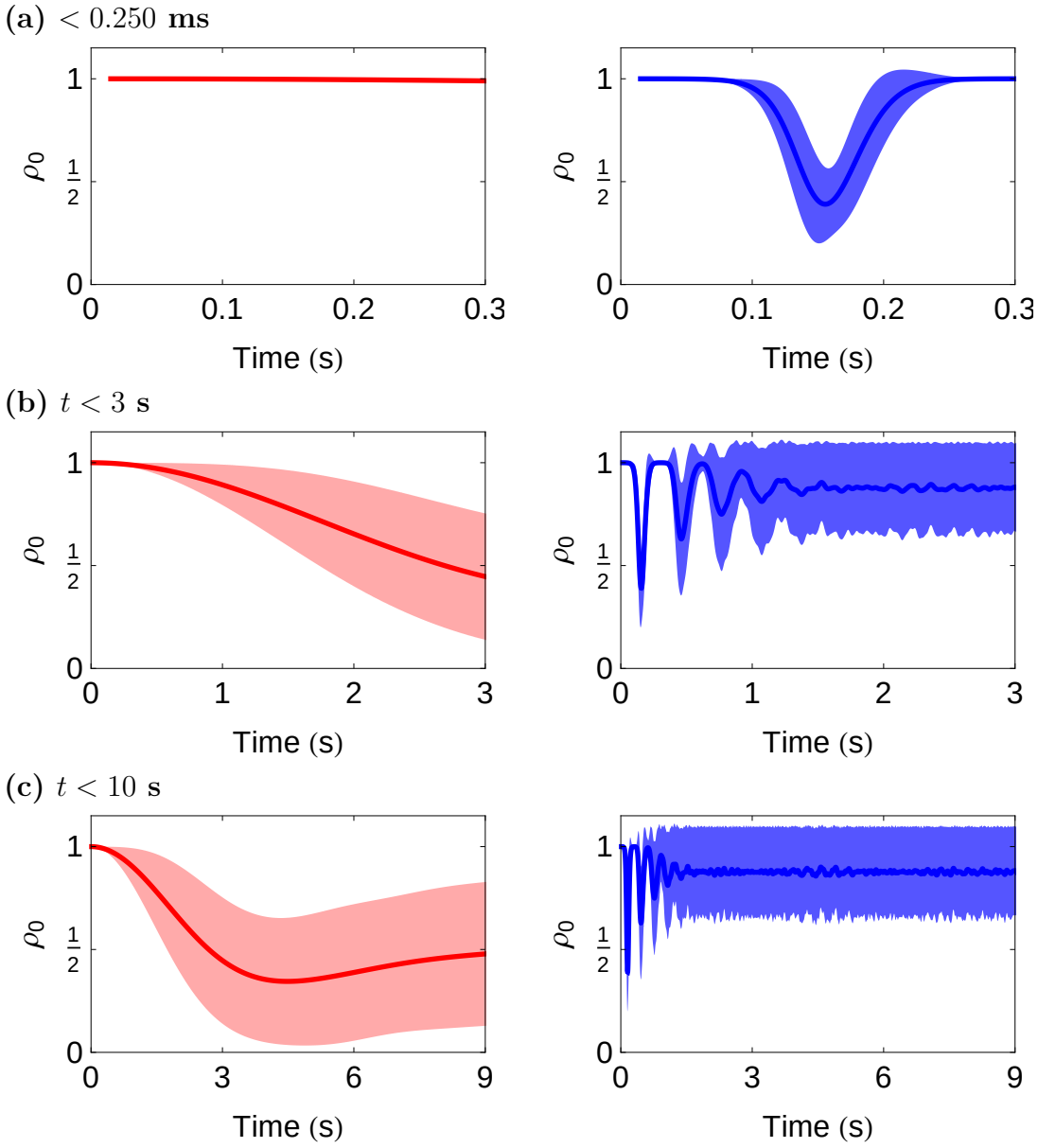

Figure 3.2: Comparison of dynamic evolution with and without a magnetic field. Shown here are the results of simulations for a magnetic field of 0 mG (left) and 200 mG (right). The solid line represents the mean, and the shaded region represents the standard deviation. Simulations for $45,000$ atoms, and $c = -2\pi \times 7.75$ Hz. Atomic loss has not been accounted for in these simulations.

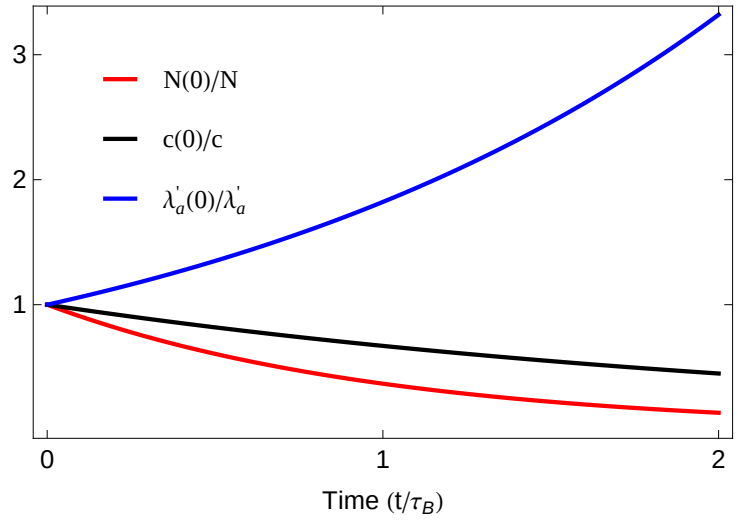

Figure 3.3: Time scaling for atom number and dynamical simulation values. Shown here is the time scaling of the atom number, N (red), inter-spin energy,$\lambda_a{}'$ (blue), and the spinor dynamical rate, c (black), assuming an exponential loss of atoms with a time constant τ_B.

3.1.4 Effect of Atomic Loss on the Simulation

For times less than $\sim$ 200 ms, the dynamical simulations have been shown to reasonably reflect the experimental results [38, 58]. However, at later times the experiment tends to oscillate in a coherent fashion immediately after the first revival in ρ_0, while the simulation pauses at the first revival, conceptually similar to the way an inverted pendulum slows near the top of an orbit. One possible explanation for this discrepancy is that the dynamical equations developed in Chapter 2 do not account for the effect of atomic loss [71]. The trap lifetime of the condensate is $\sim$ 2s, less than an order of magnitude larger than the simulation times past 250 ms, so it is not unreasonable to expect the loss to make a difference. For this thesis, the effects of loss were implemented into the dynamical equations in two ways, and will be explained in the following sections. Previous experimental groups have implemented atomic loss into their simulations differently, with some success [36, 46].

3.1.4.1 Modeling Loss by Varying the Spinor Dynamical Rate

In Section 2.2, the spatially integrated interaction strength, or inter-spin energy, $\lambda_i' = \frac{1}{2}\lambda_i \int \left|\phi(\mathsf{r})^4\right| d^3r$ was determined to scale with the total atom number as $N^{-3/5}$ for the quantum derivation of the dynamical equations. For the mean field equations, the spinor dynamical rate, c, was related to the inter-spin energy by $c = 2\lambda_a' N$, so c scales with the total atoms number as $N^{2/5}$. The inter-spin energy and the spinor dynamical rate as a function of time are shown in Fig. 3.3, along with the atom number, assuming an exponential loss of atoms with time constant τ_B. By numerically integrating the same dynamical equations, only taking into account the effect of atom loss on the density of the condensate, and therefore the values of λ_i' and c, the simulation results can be made to more accurately model the experimental results. (See Chapters 6 and 7).

3.1.4.2 Modeling Loss with a Quantum Monte Carlo Simulation

An alternate calculation of the effects of atom loss is to use a stochastic Monte Carlo (or quantum trajectories) simulation. The quantum Monte Carlo is implemented similar to Refs [71, 81–83]. The atoms are assumed to be lost one at a time and the process of losing an atom effectively measures its m_f state and so the collapse operators are simply related to the annihilation operators for the modes of the condensate. The numerical integration of the k coefficients is performed with an effective Hamiltonian given by:

$$H_{eff} = H_{SMA} - \tfrac{i}{2}\sum_i C_i^\dagger C_i \tag{3.6}$$

$$= H_{SMA} - \tfrac{i}{2\tau_B}\hat{N} \tag{3.7}$$

where $C_i = \sqrt{1/\tau_B}\hat{a}_i$ are the collapse operators for each mode ($i = -1, 0, 1$) and τ_B is the condensate lifetime. During the time interval Δt of the numerical integration each atom has a probability $e^{-\Delta t/\tau_B}$ of remaining. For each atom a random number in the

range 0 to 1 is generated to stochastically determine how many atoms to annihilate in each mode. If this number is greater than $e^{-\Delta t/\tau_B}$, then the appropriate collapse operator is applied to the state vector. The number of atoms for each mode is given by $\langle \hat{N}_i \rangle$. After the collapse operators have been applied the k coefficients are re-normalized and the next step of the numerical integration is performed with updated values for N and M. Results are obtained from the quantum Monte Carlo simulation by taking the average of quantum expectation values from many runs with the same initial conditions but a uniquely seeded sequence of random numbers to determine the annihilation probabilities. In effect, the results of the quantum Monte Carlo simulation are the average of many quantum trajectories.

At first glance the quantum Monte Carlo is a daunting task since in general it should be necessary to use a basis spanning every possible value of $N(t)$, $M(t)$, and $k(t)$ which scales as N^3. However the action of the collapse operators shifts the state vector from $N(t)$ and $M(t)$ to $N(t+\Delta t)$ and $M(t+\Delta t)$ while modifying the k coefficients in a well characterized way. At any given step of the calculation there is only one value for N and M. So for any step of the calculation the basis is proportional to $N(t)$ and is completely described with the current values of N, M, and the complex coefficients for the k index.

The results for the quantum Monte Carlo simulation are nearly identical to those produced by the scaling of the spinor dynamical rate. Through the remainder of this thesis, the quantum Monte Carlo simulation is used for comparison of all experimentally obtained values, except where specifically indicated, where the scaled spinor dynamical rate is used. Fig. 3.4 shows the comparison of the dynamical simulations for the system without loss (left column) and with atomic loss(right column). The obvious difference between the two sets of simulations occurs at the first revival of the system ($t \sim 250$ ms). The simulation without loss shows a long pause (~ 150 ms) followed by dampened, multi-frequency oscillation. The simulation that incorporates

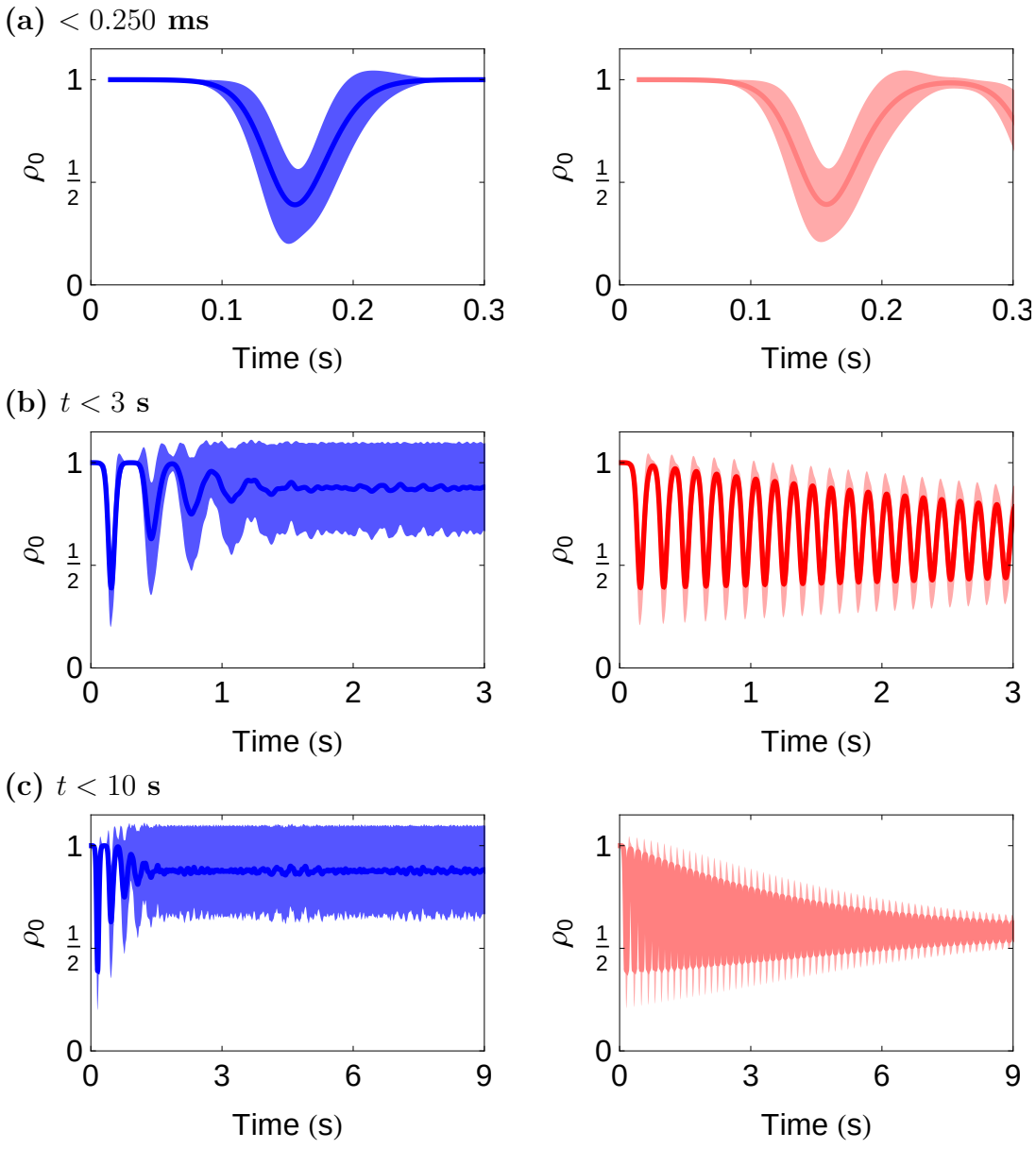

Figure 3.4: Comparison of dynamic evolution with and without loss. Shown here are the results of simulations without (left) and with (right) atomic loss accounted for. Simulations for $45,000$ atoms, $B = 220$ mG, and $c = -2\pi \times 7.75$ Hz. The shaded region represents the standard deviation.

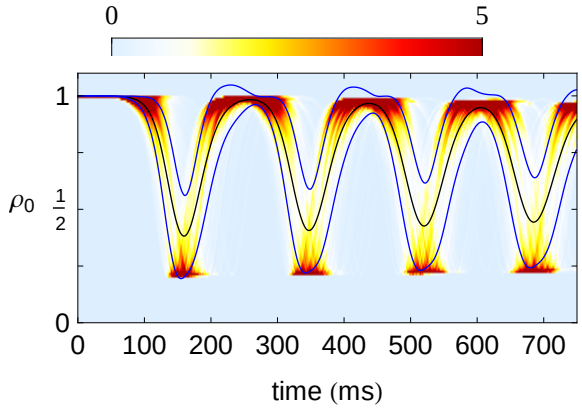

Figure 3.5: Evolution of the probability density of ρ_0. The black line represents the mean value of ρ_0 and the blue lines represent $\pm\sigma$, the standard deviation.

loss, on the other hand, shows no noticeable pause. Instead, it continues oscillating with approximately a single-frequency. There is slight dampening of the evolution, as well.

3.2 Evolution of the Probability Density

The previous simulation results for ρ_0 only showed the mean and standard deviation of the evolution. However, the spin-1 BEC shows detailed non-Gaussian distributions in the evolution of ρ_0 as shown in Fig. 3.5, where loss is included. The values for the simulation were chosen to match experimental conditions ($N = 45,000$ atoms, $B = 220$ mG, $|c| = 2\pi 7.75$ Hz, $\tau_B = 1.8$ s). Notice how the system pauses in the initial state for ~ 100 ms before beginning rapid oscillations. This is similar to how a pendulum prepared in the inverted state has a long pause before it begins rapid oscillations. The pause time of the spin-1 BEC is logarithmically sensitive to the size of its initial uncertainty (e.g. For larger condensates the pause time scales logarithmically with the number of atoms.) In the loss-less model, the spin-1 BEC pauses after the first revival, just as an inverted pendulum would. In the model that includes loss, though, there is no subsequent pauses. Fig. 3.5 also shows how the probability of ρ_0 tends to bunch near the turning points in the evolution. At these

times one can see that the mean of ρ_0 is not close to point of maximum probability. This is a good indication that there is a skew in the distribution, an inherently non-Gaussian feature. More on the non-Gaussian evolution of the spin-1 BEC will be discussed in Chapter 7.

CHAPTER 4

SIMPLE PENDULUM THEORY

The mean-field equations of motions developed in Chapter 2 take the form of a non-rigid pendulum. Specifically, the form is that of a momentum-shortened pendulum, where the length of the pendulum is reduced for larger values of the momentum. Unlike a momentum-lengthened pendulum (e.g. a pendulum attached to the pivot point with a spring), it is difficult to contrive a macroscopic physical system that models the many-body BEC system. However, much insight can be gained from first looking at the simple pendulum (e.g. the behaviour of the simple pendulum near the hyperbolic fixed point, mapping of the phase space, etc.). This chapter will explore the simple pendulum, (including the classical, semi-classical, and quantum model systems), the phase space, the equations of motion, and the simulation results. The concept of quadrature squeezing will also be introduced with the simple pendulum.

It is important to note, however, that even though the Hamiltonian for a simple pendulum is similar in form to the Hamiltonian for the mean-field approach of a spinor BEC, there are subtle differences in the phase spaces and dynamics of the two that make direct comparison limited. Moving forward, it is a caution to the reader not to read too much into any direct comparisons between the two systems. The systems are analogous, but not identical.

4.1 The Simple Pendulum, Classical Picture

A simple pendulum consists of a point mass m at the end of a massless, rigid rod of length L. Its angular position, θ, will be measured from the upward vertical (See Fig. 4.1). The Hamiltonian and corresponding equations of motion for the pendulum

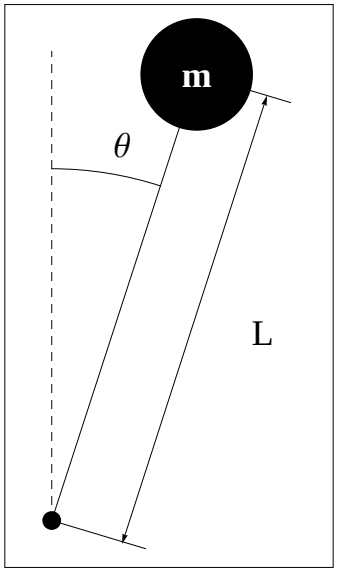

Figure 4.1: The simple pendulum. The simple inverted pendulum consists of a point mass m affixed to a rigid, massless rod of length L. Its angular position is measured from the upward vertical and the zero point for potential energy is when $\theta = \frac{\pi}{2}$.

are:

$$H = \frac{{p_\theta}^2}{2mL^2} + mgL\cos\theta \tag{4.1a}$$

$$\dot{p}_\theta = -\frac{\partial H}{\partial \theta} = mgL\sin\theta \tag{4.1b}$$

$$\dot{\theta} = \frac{\partial H}{\partial p_\theta} = \frac{p_\theta}{mL^2} \tag{4.1c}$$

where the zero point of potential energy was chosen to be $\theta = \pi/2$. The Hamiltonian in Eqn. (4.1a) can be used to plot the corresponding phase space and energy contours. The phase space is divided into two regions: a region of closed orbits (red) where the pendulum oscillates back and forth, and a region of phase winding orbits (blue) where the pendulum undergoes complete loops. The two regions are divided by the separatrix, which are the orbits with total energy exactly equal to mgL. The simple pendulum has ground state locations at $(\theta = \pm n\pi, p_\theta = 0)$, as well as hyperbolic fixed points located at $(\theta = \pm 2n\pi, p_\theta = 0)$ (See Fig. 4.2). If the pendulum has energy larger than mgL, it will undergo phase winding orbits, but if it has energy less

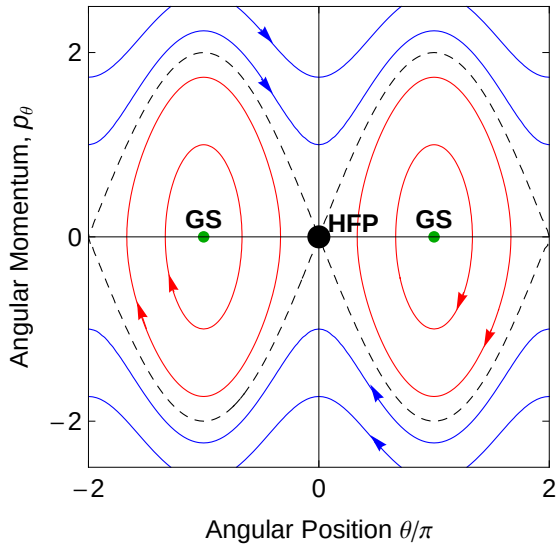

Figure 4.2: Simple inverted pendulum phase space. The phase space for the simple pendulum is depicted. The energy contours are shown with arrows indicating direction of dynamic evolution. The thick black line represents the separatrix, the red lines are energy contours for closed orbits, and the blue lines are energy contours for phase-winding orbits.

than mgL, it will undergo phase oscillating orbits. If the pendulum is prepared in an initial configuration with a total energy exactly equal to mgL, it will evolve from its start point along the separatrix with just enough momentum to reach one of the hyperbolic fixed points in the phase space, where it comes to rest. If the pendulum could be prepared perfectly at one of the hyperbolic fixed points, it would not evolve in the classical limit. Such an initial state is not physically possible, however, due to thermal fluctuations and inevitable imprecisions in the initial conditions.

The types of orbits for each region are shown in Fig. 4.3. Fig. 4.3 (a) shows the commonly visualized pendulum motion, where the pendulum oscillates back and forth in coordinate space, and the phase-space trajectory is a closed orbit inside the separatrix. The parametric plot of the angular displacement for this orbit is shown in the right column.

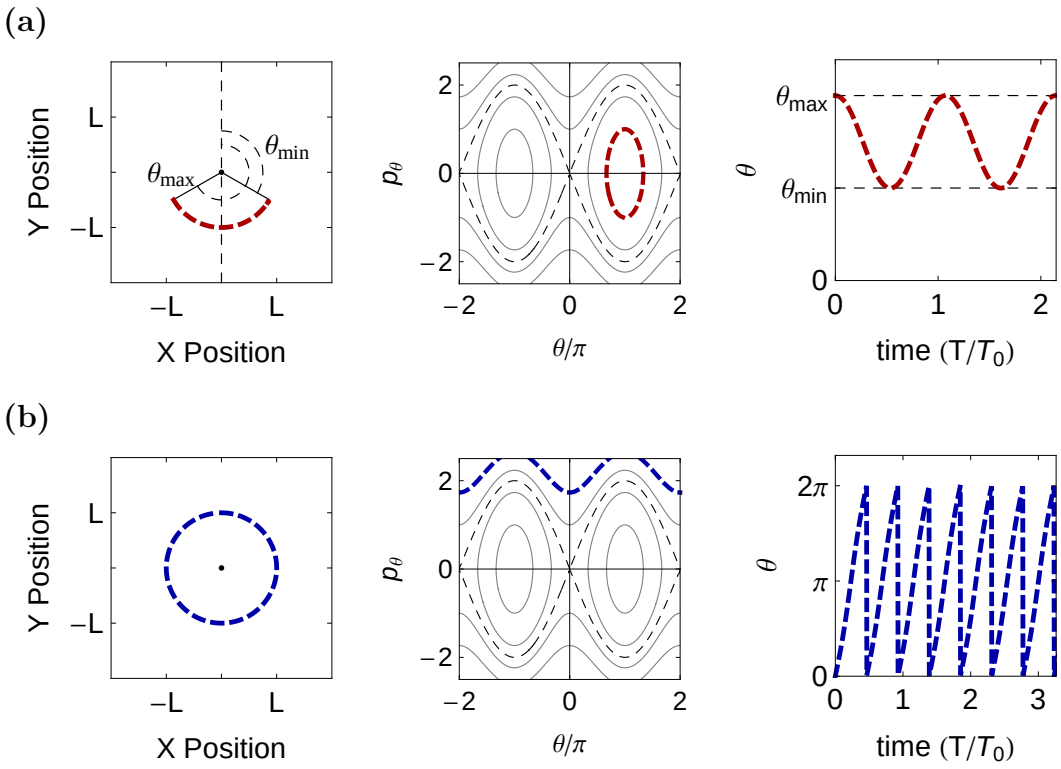

Figure 4.3: Closed and winding orbits. The two main types of orbits for a simple inverted pendulum. The left column for rows (a) and (b) is the coordinate space representation, and the center column is the orbit depicted on the phase space. The right column shows the parametric plot of the orbit. **(a)** shows a pendulum with a total energy less than mgL. The pendulum oscillates back and forth in coordinate space between a minimum angle and maximum angle. Orbits in this category have angular displacements between 0 and 2π. **(b)** shows a pendulum with a total energy greater than mgL. This pendulum makes complete circular paths in coordinate space, and its angular displacement keeps increasing by 2π with each orbit.

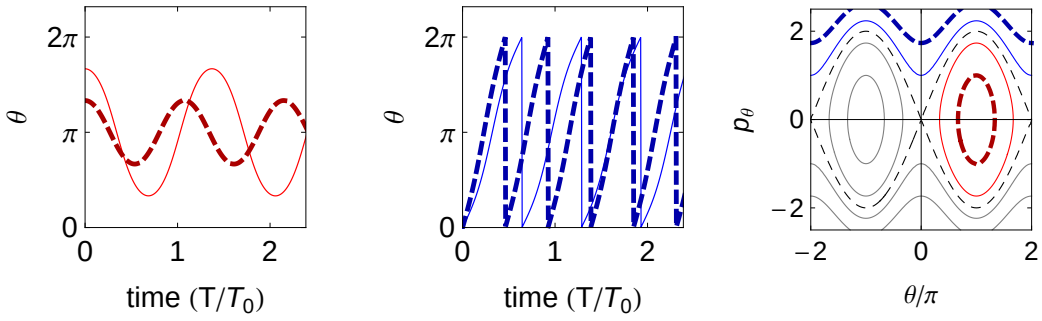

Figure 4.4: Period of oscillations for different energies. Both phase winding and closed orbits of different energies. The time for each plot is relative to the period for small oscillations, $T_0 = 2\pi\sqrt{L/g}$.

Fig. 4.3 (b) shows the phase-winding orbit, where the pendulum undergoes complete circles in coordinate space, and the phase-space trajectory is outside of the separatrix. The parametric plot of the angular displacement for this orbit is shown in the right column, as well. The parametric and phase space plots of Fig. 4.3 provide several useful insights for the many-body quantum system. First, one can estimate where in the phase space an orbit begins based on the shape of the parametric plot for the angular displacement. Looking at Fig. 4.3 (a) one can see that the dashed red line starts at rest at a maximum and moves to a minimum, where it again stops momentarily and changes direction. This can be seen in the phase space, as well. The same can be done for the phase-winding orbits in Fig. 4.3 (b). This technique can be employed for many different oscillations and one can effectively map the phase space by observing oscillations of different initial conditions, which will be done in Chapter 6.

Second, the period of the orbit decreases as you move further from the separatrix. Fig. 4.4 shows orbits at different energies on a common time scale, where $T_0 = 2\pi\sqrt{L/g}$ is the period of oscillation for small displacements near the ground state. The dashed lines in each are the orbits furthest from the separatrix, and the solid lines are the orbits closest to the separatrix. It is clear that the closer to the

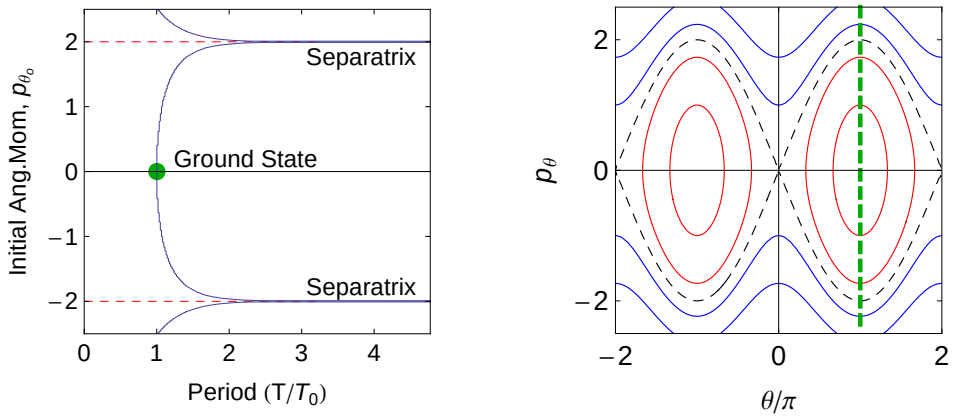

Figure 4.5: Cross-section of simple pendulum phase space. The period is measured for different values of the initial angular momentum for an angular displacement of π. (Indicated by a green line in the phase space.) The separatrix is indicated with dashed red lines, and the ground state location is labeled with a green dot.

separatrix the orbit, the longer the period, with the separatrix having an infinite period. Consider the green line in Fig. 4.5, that cuts across the phase space for different initial values of angular momentum at a fixed value of the angular displacement, in this case, $\theta_0 = \pi$. The period for the different orbits is plotted in Fig. 4.5. The separatrix is clearly visible at the points where the period asymptotically approaches infinity, and the ground state is easily identifiable in this case because the initial angular displacement passes through where one expects to find the ground state. This can be done for several similar cuts along both directions to quickly verify the map the phase space, as well.

4.1.1 The Simple Inverted Pendulum

This subsection will consider the simple pendulum initialized to points near the hyperbolic fixed point, where $(\theta_0,\, p_{\theta_0}) \sim (0, 0)$. Fig. 4.6 shows the evolution of an inverted pendulum with initial conditions $(\theta_0,\, p_{\theta_0}) = (0.025, 0)$ (Red line). As expected, the pendulum stays balanced in the inverted position for a finite period of time before

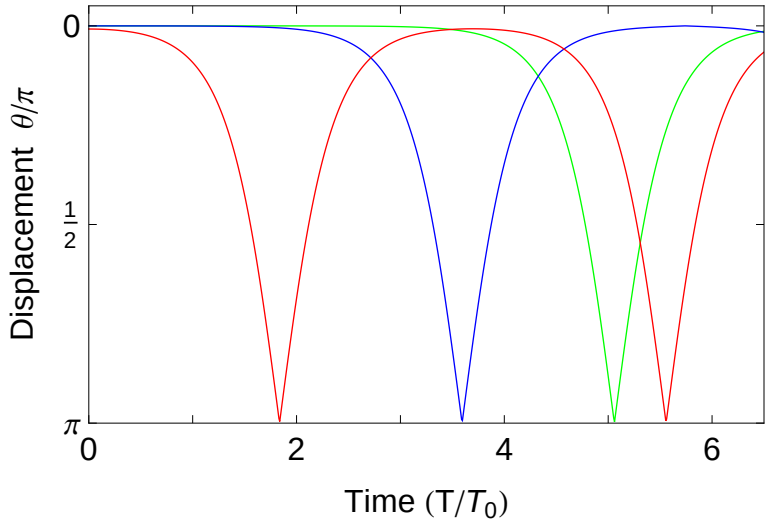

Figure 4.6: Displacement of a simple inverted pendulum. The displacement of a simple inverted pendulum is shown for several initial states near the hyperbolic fixed point. The red line is for $(\theta_0, p_{\theta_0}) = (0.025, 0)$. The blue line is for $(\theta_0, p_{\theta_0}) = (10^{-4}, 0)$. The green line is for $(\theta_0, p_{\theta_0}) = (10^{-6}, 0)$. The pendulum spends much of its time in the inverted state, and quickly falls through its minimum, returning to the inverted position where it again slows at the top. The initial delay before evolution increases as the initial state of the pendulum approaches the hyperbolic fixed point at $(0, 0)$.

it rapidly falls through its lowest point. The pendulum returns to its start position, slowing down considerably near the top. For $p_{\theta_0} = 0$, as $\theta_0 \to 0$, the initial pause goes to infinity, as can be seen from Fig. 4.6 (blue line- $(\theta_0, p_{\theta_0}) = (10^{-4}, 0)$, green line- $(\theta_0, p_{\theta_0}) = (10^{-6}, 0)$).

4.2 The Simple Pendulum, Semi-Classical Picture

A semi-classical approach to the simple pendulum can be used (in lieu of a fully quantum approach) when quantum mechanical effects become important [84]. In the semi-classical approach, the quantum nature of the system is captured with a quasi-probability distribution (QPD) representing the initial state. Each initial condition from the QPD is then separately evolved in time using the classical equations of motion.

Quantum mechanical effects must be considered when the system size is comparable to the deBroglie wavelength. The dimensionless quantity $\alpha = 4m^2gL^3/\hbar^2$, where $\sqrt{\alpha}$ is the ratio of pendulum length to the reduced deBroglie wavelength, $\lambda_{dB}/2\pi$ [84], will aid in this determination. For $\alpha \gg 1$ the classical approach discussed in the previous section is sufficient to describe the dynamics. However, when $\alpha \leq 1$ quantum mechanics are needed to describe the evolution. A simple method for implementing the quantum mechanical nature of the evolution is to use the semi-classical approach that both captures the quantum dynamics for $\alpha \leq 1$ and yet also works for larger α.

When initializing the pendulum, regardless of how careful the preparation, there must be an uncertainty in the initial angular position, $\Delta\theta$. In the quantum limit, the uncertainty principle dictates that there is a corresponding minimum uncertainty in the angular momentum, Δp_θ, given by [1]

$$\Delta\theta\Delta p_\theta \geq \hbar. \tag{4.2}$$

Since $\Delta p_\theta = mL^2\Delta\dot{\theta}$, the resulting uncertainty in the initial angular velocity is then $\Delta\dot{\theta} \geq \hbar/(mL^2\Delta\theta)$.

In general, the uncertainty in preparation will result in equal uncertainties in the potential and kinetic energy, which provides the relationship $1/\alpha \simeq (\Delta\theta)^2 \sin(\frac{\Delta\theta}{2})2$. This relationship can be used to calculate $\Delta\theta$ for any value of α. As an example, consider a classical pendulum with $m = 0.1$ kg and $L = 1.0$ m, $\alpha = 3.5 \times 10^{67}$ and $\Delta\theta = 1.8 \times 10^{-17}$ radians. On the other hand, for a quantum system where $\alpha = 1$, $\Delta\theta \sim 1.5$ radians.

A quasi-probability distribution for θ and $\dot{\theta}$ is constructed using a normalized Gaussian centered on $(\theta, \dot{\theta}) = (0, 0)$, using uncertainties as calculated above [84]. This ensemble is then propagated forward in time using any number of techniques.

[1] Ref. [85] provides a more rigorous restatement of the uncertainty principle that accounts for the periodicity of θ. However, for $\Delta\theta \ll 2\pi$, $\Delta\theta\Delta p_\theta \geq \hbar$ is an acceptable approximation [84].

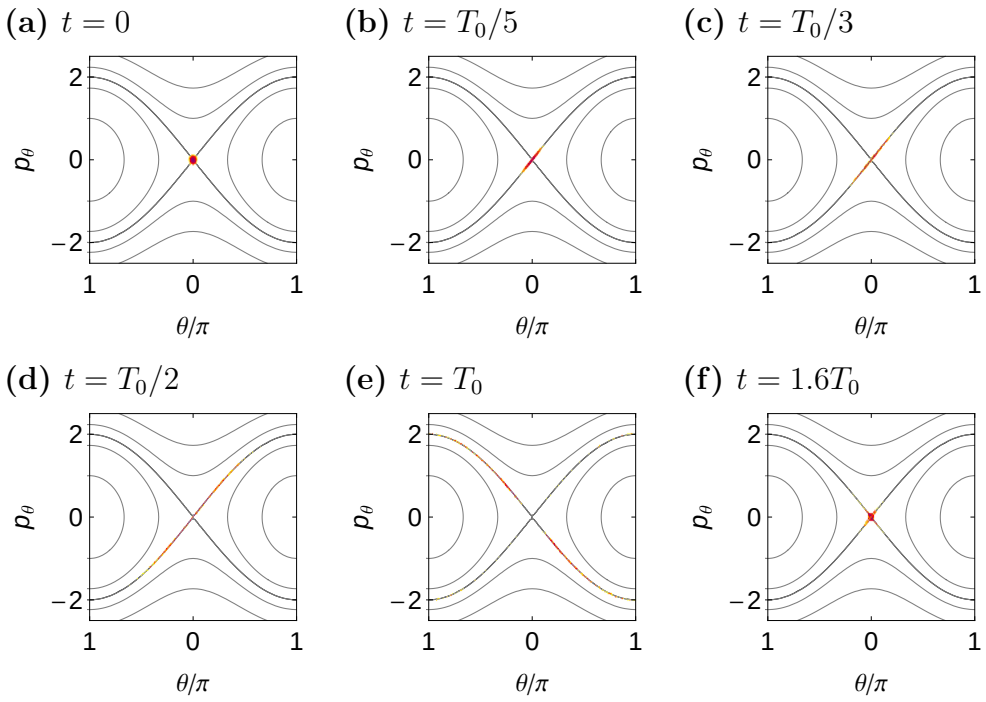

Figure 4.7: Simple pendulum probability density evolution. The evolution of the initial state is shown for various time steps. The system starts as a Gaussian distribution centered on the hyperbolic fixed point.

Since the initial condition of the pendulum is represented by a probability distribution, one can expect that subsequent measurements of the system evolution will also result in a distribution of the angular displacement for different times. The evolution of the a simple inverted pendulum for several different times is shown in Fig. 4.7. $\Delta\theta = 0.05$, well in the classical regime ($\alpha \sim 10^6$), was chosen for illustrative purposes, but the techniques can be used for the quantum regime, also. The ensemble of systems is initialized with a distribution centered on the hyperbolic fixed point at $(0, 0)$. The evolution of each system in the ensemble follows the appropriate classical energy contours based on the initial conditions. This evolution causes the ensemble to symplectically[2] squeeze [86, 87] along the separatrix in the first and third quadrant

[2]Hamiltonian systems such as the simple pendulum are well known for having a symplectic phase space. In a symplectic phase space, the area is preserved under transformation. So the area of the distribution at $t = 0$ would be the same as the area of the distribution at $t > 0$. Depending on the initial conditions, this concept is what produces quadrature squeezing in Hamiltonian systems.

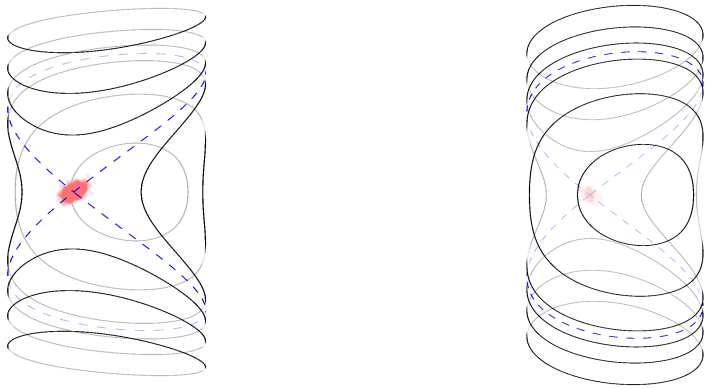

Figure 4.8: Simple pendulum cylindrical phase space. The phase space of the simple pendulum can be mapped to a cylinder where the contour lines meet at $\pm\pi$.

of the phase space. The evolution continues, with the closed orbits completing their orbits inside the separatrix and the winding orbits continuing to acquire phase. The simulations used to make Fig. 4.7 reset the winding phase trajectories to the opposite side of the phase space (e.g. $\theta \geq \pi \rightarrow \theta - \pi$) in order to continue to track the evolution graphically. An alternative phase space is shown in Fig. 4.8, where the phase space of Fig. 4.7 is wrapped around a cylinder such that contour lines meet at $\pm\pi$.

4.2.1 Non-Gaussian evolution of the simple inverted pendulum

Another way of following the evolution of the inverted pendulum's probability distribution is to look only at the magnitude of the angular displacement from the inverted position. This method does not distinguish between positive and negative displacement. The results of this method are shown in Fig. 4.9. The system is initialized at $t = 0$ narrowly distributed about $(\theta = 0, p_\theta = 0)$. As the system evolves, the different ensembles have different periods based on their location in the phase space. For portions of the evolution time the mean of $|\theta|$ does not pass through the point of highest probability of the system. Additionally, the distribution for $|\theta|$ appears to

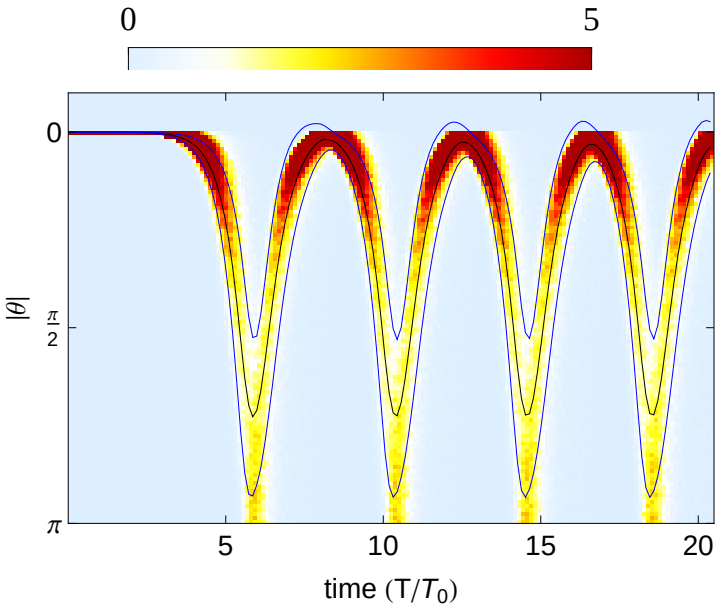

Figure 4.9: Probability distribution evolution of $|\theta|$. The evolution of the probability distribution $|\theta|$ is shown. The black line represents the mean value of $|\theta|$, while the blue lines represent the bounds of the standard deviation.

be sharply skewed from the mean at certain times in the evolution, thus indicating that the mean and the standard deviation are not adequate to fully describe the evolution of the initial distribution. To better characterize the distributions, it is useful to examine the cumulants. The first cumulant represents the mean of the distribution. The second cumulant represents the standard deviation of the distribution. The third cumulant is related to the skew (or the asymmetry, which direction the data is weighted relative to the mean) of the distribution. A positive third cumulant means that the majority of the values in the distribution are 'to the left' of the mean. The fourth cumulant is loosely related to the pointed-ness of the data. Cumulants, κ_n, should not be confused with central moments, $u_n = \langle (x - \bar{x})^n \rangle$. Though the first through third cumulants are the same as the central moments, the fourth and higher cumulants differ. The cumulants have the advantage of being independent of each other, while central moments are not. (e.g. The higher central moments may be

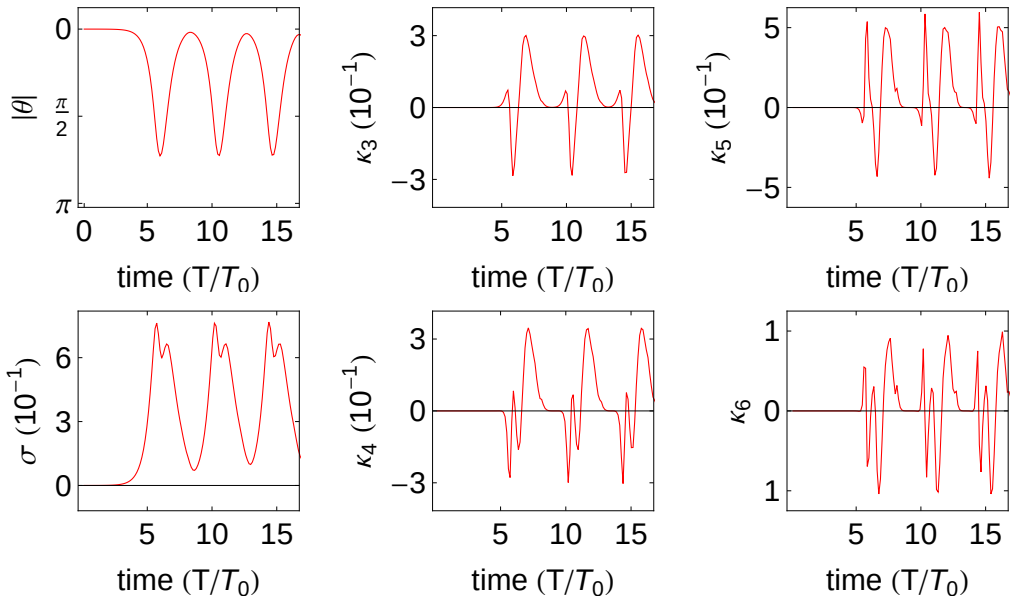

Figure 4.10: First through sixth cumulants of $|\theta|$. The evolution of the first through sixth cumulants of $|\theta|$ are shown, with the odd cumulants on the top row, and the even cumulants on the bottom row.

dominated by terms from the lower moments, whereas cumulants subtract the contributions from lower cumulants from the higher cumulants.) The first through sixth cumulants are derived in Appendix B. Fig. 4.10 shows the first six cumulants for the evolution of the inverted pendulum. The cumulants provide some interesting insights. First, the second cumulant, or the standard deviation, shows a double-peaked structure that repeats itself during the evolution. What is more interesting, though, is the low points in the standard deviation. For each successive oscillation, the minimum standard deviation increases. This is due to the dispersion of the system, which is visible in Fig. 4.7. Due to the different periods of neighboring orbits, the system will eventually spread out along the entire phase space trajectories.

The non-Gaussian nature of the evolution is visible in the third and fourth cumulants. For a Gaussian distribution, the third cumulant and fourth cumulants are zero. However, the third and fourth cumulants for the simple pendulum are clearly not zero, which indicates non-Gaussian activity at the extremes of the pendulum's motion.

The fifth and sixth cumulants also show structure in the evolution of the pendulum. These same traits of the evolution will be seen in the non-rigid, momentum-shortened pendulum in Chapter 7.

4.3 The Simple Pendulum, Quantum Solution

The time-independent Schrödinger wave equation for the simple pendulum is given by

$$-\frac{\hbar^2}{2mL^2}\frac{\partial^2\psi}{\partial\theta^2} + mgL\cos\theta\psi = E\psi.$$

The variable substitution $\theta = 2z$, $a = -8mL^2E/\hbar$, and $\alpha = 4m^2gL^3/\hbar^2$ provide the standard form of Mathieu's equation:

$$\frac{\partial^2\psi}{\partial z^2} + (a - 2\alpha\cos 2z)\,\psi = 0. \tag{4.3}$$

The solutions to Eqn. (4.3) are the periodic Mathieu sine and cosine functions, $se_n(z,\alpha)$ and $ce_n(z,\alpha)$ with eigenvalues $a_n(\alpha)$ and $b_n(\alpha)$ for even n, respectively. The initial condition, $\psi(0) = \left(\frac{1}{2\pi\Delta\theta^2}\right)^{\frac{1}{4}}\exp\left(\theta^2/2\Delta\theta^2\right)$ (where $\Delta\theta$ is obtained from Eqn. (4.2)) is expanded on to the Mathieu cosine functions since it is an even function. The time evolution becomes:

$$\psi(r,t) = \psi(r)\,e^{-iEt/\hbar} = \sum_{n,even}\gamma_n ce_n\exp\left[ia_nt/\hbar\right]$$

where γ_n are the expansion coefficients of for the initial conditions, ce_n are the periodic Mathieu cosine functions, and a_n are the respective eigenvalues.

An alternative approach is to simply numerically integrate the time-dependent Schrödinger equation:

$$-\frac{2}{\alpha}\frac{\partial^2\psi}{\partial\theta^2} + \cos(\theta)\,\psi = \frac{2i}{\sqrt{\alpha}}\frac{\partial\psi}{\partial s}$$

where the dimensionless $s = \sqrt{L/g}t$ was introduced.

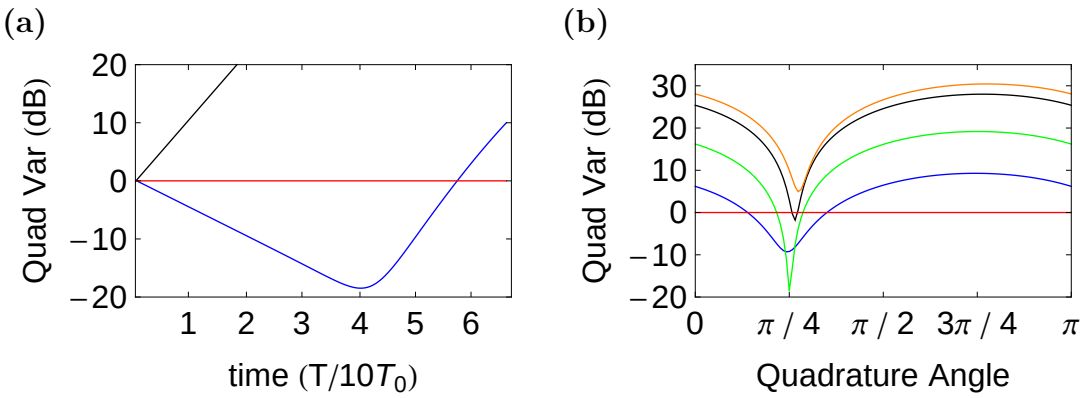

Figure 4.11: Quadrature squeezing in a simple pendulum. The results of simulating the quadrature squeezing in the simple inverted pendulum. **(a)** shows the evolution of the maximum predicted squeezed and anti-squeezed quadrature for the system. **(b)** shows the squeezing parameter for different quadrature angles and evolution times.

4.4 Quadrature Squeezing in the Simple Pendulum

Quadrature squeezing is typically discussed in systems other than the simple pendulum. For example, squeezing has been studied for spin systems by using interactions with squeezed light [88], repeated quantum non-demolition (QND) measurements [89, 90], light in cavity modes [91, 92], and by collisional interactions [93, 94]. More recently, Refs. [38, 58] studied spin-nematic squeezing using the spin-1 system discussed in this thesis. The idea of squeezed light, spin-squeezing, and squeezing in quantum systems is theoretically well understood [80, 95, 96]. However, the systems studied in the above references are not required to gain an understanding of quadrature squeezing. The concept of quadrature squeezing in classical systems has been used for decades to improve precision measurements [97–99]. The simple pendulum, by the very nature of its Hamiltonian and resulting behavior near a hyperbolic fixed point, demonstrates quadrature squeezing. Squeezing in a quantum simple pendulum is discussed in in Ref. [100]. This section will address the concept of quadrature squeezing for the classical simple pendulum ($\alpha \sim 10^{67}$). It is well known that Hamil-

tonian systems provide a symplectic[3] phase space [86, 87, 101–105]. The benefit of the symplectic phase space is that the area of the phase space is conserved under transformation, such as time evolution. In other words, if a system, described by a Hamiltonian such as Eqn. (4.1a), is initialized in a state described by a probability distribution such as was done in Section 4.2.1, then the area of that probability distribution will remain constant during time evolution. When looking at Fig. 4.7 one can see that if the area of the distribution is conserved, then for later times during the evolution, the distribution must squeeze in the direction perpendicular to the flow in phase space. If the system could be prepared in a minimum uncertainty state, then the uncertainty of the quadrature perpendicular to the flow would obviously fall below the standard quantum limit.

In order to quantify the amount of squeezing, a squeezing parameter is defined for the simple pendulum system. Section 4.2 gave the uncertainty relationship for the simple pendulum at the Heisenberg limit as $\Delta p_\theta \Delta\theta \geq \hbar$. However, quadrature squeezing can be demonstrated for any initial state where $\Delta p_\theta \Delta\theta = \bar{\Delta}$. Using this relationship, a squeezing parameter is defined in terms of the quadratures of θ and p_θ:

$$\xi^\phi = \langle (\Delta((\cos\phi)\theta + (\sin\phi)p_\theta))^2 \rangle / (\bar{\Delta}^2) \tag{4.4}$$

with ϕ as the quadrature angle. Squeezing in the simple pendulum system will be indicated by the value of $\xi^\phi < 1$ for some value of ϕ.

The results of the quadrature squeezing simulations are in Fig. 4.11. Fig. 4.11 **(a)** shows the squeezing parameter at the predicted maximum squeezed and anti-squeezed quadrature. While the variance of the result drops for squeezing, the variance in the

[3]The word symplectic, used for the first time with its modern mathematical meaning by Hermann Weyl (1885 1955) in his book first published in 1939, derives from a Greek word meaning complex. Weyl used it because the word complex, whose origin is Latin, had already a different meaning in mathematics. [101]

other quadrature is increasing such that their product remains constant. Fig. 4.11 **(b)** shows how the squeezing parameter changes for different quadrature angles.

4.4.1 Ways to Produce Squeezed States for the Inverted Pendulum

In previous classical squeezing examples [97–99], parametric amplification of the potential energy was used to generate the quadrature squeezing. The basic principle is that the shape of the phase space is changed and the system is allowed to evolve in the new phase space until its squeezed state is appropriately positioned, then the phase space is returned to its original state and the new system evolves from an initial configuration that is squeezed in one quadrature. For a simple pendulum, an analogous technique can be used. Instead of a point-mass system under the influence of gravity, consider a charged particle pivoting on a rigid, massless rod in the presence of an external electric field perpendicular to the rotation axis of the particle. The equations of motion would be virtually identical, but the direction of the electric field could be changed when desired. If the system begins as in Fig. 4.12 (a), the probability distribution of the system will squeeze along the separatrix as previously discussed. At some later time t the direction of the electric field is changed. The system then resembles Fig. 4.12 (b). In the new phase space, the probability distribution will rotate around the ground state until it is oriented in the preferred direction. The electric field can be changed back to its original direction, and the "new" initial conditions will evolve as before, but one of the quadratures will be squeezed. (See Fig. 4.12 (c).)

4.5 Concluding Remarks

The similarities between the mean-field equation for the spin-1 BEC and the simple pendulum make a strong understanding of the simple pendulum very useful when working with the spin-1 BEC. Using the shape of the parametric plots and the period measurements to map the phase space in a simple pendulum has direct applications to mapping the phase space for the spin-1 BEC. Additionally, the uncertainty in the

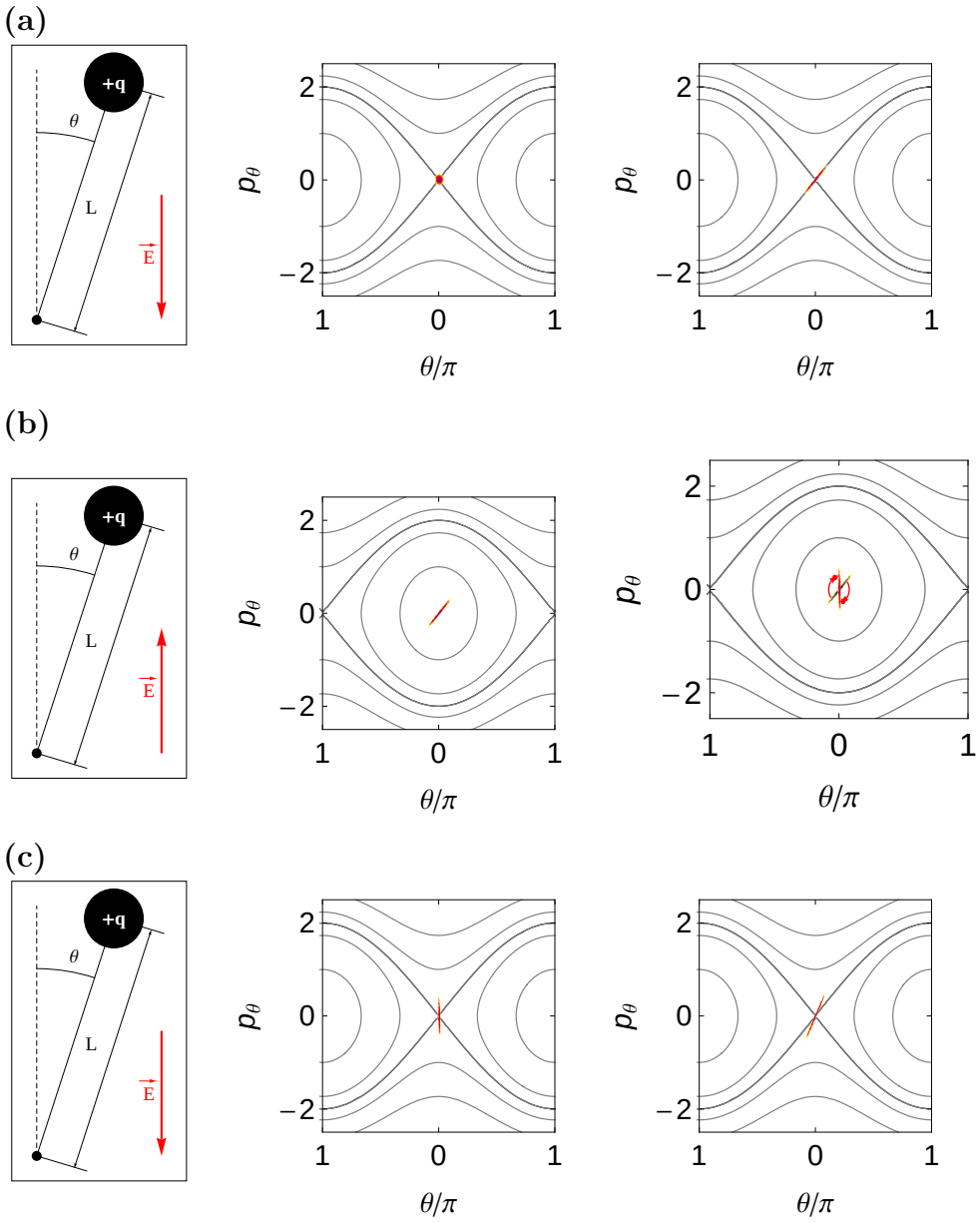

Figure 4.12: Creating squeezed quadratures in a simple pendulum. The creation of squeezed quadratures for improved measurements is shown. In each row, the first figure is the model system with the electric field direction indicated. The middle figure is the initial state of the system. The right column is the system after a finite evolution time. The distribution size has been exaggerated for clarity. **(a)** shows the initial squeezing of the system along the separatrix. In **(b)**, the direction of the electric field is changes, changing the shape of the phase space. The probability distribution rotates clock-wise around the phase space until a later time when it is oriented in the desired direction. In **(c)**, the electric field is changed back to its original orientation, and the squeezed state is allowed to evolve.

initial conditions for a simple pendulum leading to a probability distribution at later times also lends directly to the BEC experiment, as do the semi-classical solution techniques. Lastly, the concept of quadrature squeezing found in novel systems can be conceptually explained using the simple pendulum example.

Despite the differences between the two systems, much of the basic physics between the two is the same, particularly near the hyperbolic fixed point, which is the starting point for all of our experimental procedures. Chapter 6 will explore the phase space of the spin-1 BEC using similar techniques outlined here. Chapter 7 will examine the non-Gaussian evolution of the BEC in a similar fashion to the methods shown in this chapter.

CHAPTER 5

EXPERIMENTAL APPARATUS

A basic top-down view of the schematic of the experimental chamber is shown in Fig. 5.1, where the acceleration due to gravity points into the page. The chamber contains rubidium atoms in ultra-high vacuum (UHV), and the chamber is designed for ample optical access (seven 2.75" flanges and two 6" flanges). Near resonant light for the magneto-optical trap (MOT) is directed through orthogonal view ports in three dimensions where they intersect in the center of the chamber. The MOT beams in the gravity direction are not shown. Additionally, the repump transition beams are not shown, as they are directed along the same path as the MOT beams in the gravity direction. Around the chamber are the optics associated with directing and focusing the dipole force trapping lasers. The main trapping laser is a CO_2 laser, and a cross trap laser beam at 852 nm is not shown because it is above the chamber and out of the plane of the schematic. The trapping lasers are directed to overlap the center of the MOT in the chamber. There are three lenses in the chamber: two ZnSe lenses are used for focusing the CO_2 trapping laser, while the third lens is for imaging. Three orthogonal magnetic bias coils are mounted directly to the chamber that are used for nulling out the Earth's magnetic field and applying the desired experimental bias field. There are three sets of gradient coils as well. Two are oriented along the CO_2 laser axis, one for zeroing the gradient in that direction, and the other for applying a Stern-Gerlach separation force for imaging of the m_f states. The third set of gradient coils provides the magnetic field gradient for the MOT. They are not shown in the schematic, but are located above and below the chamber and are oriented such that the gradient produced is parallel to the gravity direction. Also not shown in the

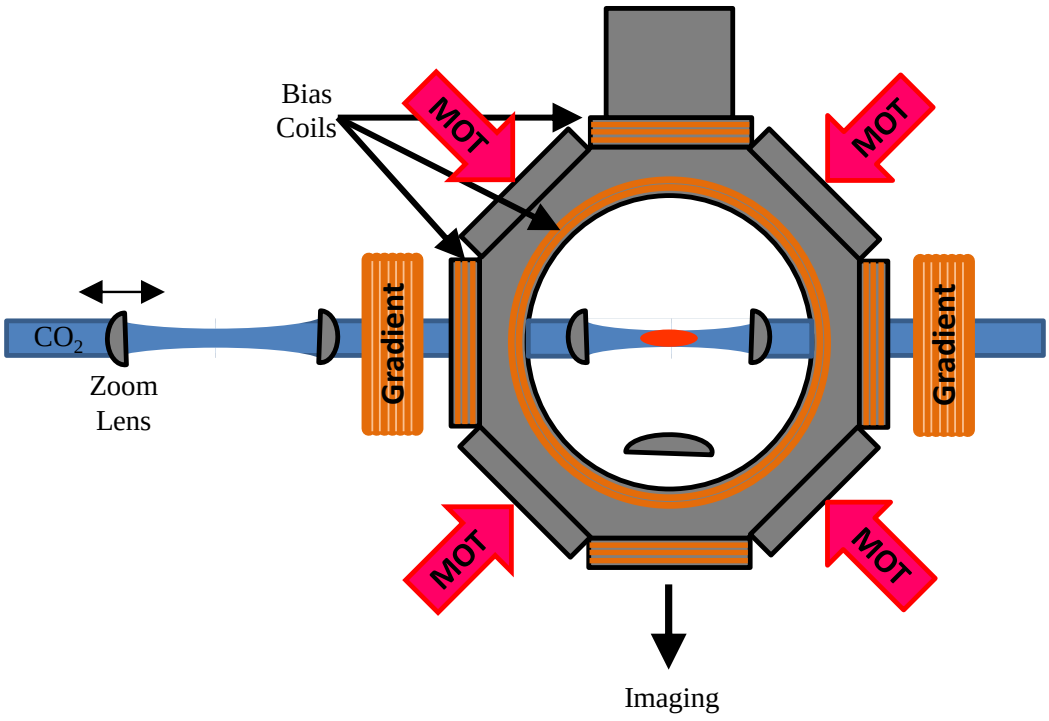

Figure 5.1: Diagram of the BEC chamber. Shown here is the BEC chamber, along with the CO_2 path, four of the six MOT beams, the gradient and bias coils, and the imaging axis.

schematic are the microwave horn (pointing into the chamber from above) and the RF coil (which sits on top of the upper window).

5.1 Vacuum System

The experimental chamber is a stainless steel octagon from Kimball Physics maintained at UHV by an ion pump and a titanium sublimation pump. The octagon has two large glass windows mounted on 6" flanges, and five smaller glass windows mounted on 2.75" flanges. All of the glass windows are anti-reflective coated for broadband near infra-red. Of the remaining three 2.75" ports, two are mounted across from each other with zinc selenide (ZnSe) windows to allow the CO_2 laser beam ($\lambda = 10.6$ μm) to pass through. The final 2.75" flange, which is located opposite the imaging axis of the experiment, is connected to the vacuum pumps. As stated above, there

are two ZnSe lenses inside the chamber for focusing the main trapping laser and a high-aperture laser objective (HALO) lens for imaging (Fig. 5.1).

The rubidium in the chamber comes from two sources. The first is from getters that are mounted on electrical feed-throughs of the chamber. The rubidium is released into the chamber by passing current through the feed-through, heating up the getter and releasing the rubidium. The second source is the left-over rubidium already in the chamber. It is recycled using light intensity assisted de-adsorption (LIAD) [106] which involves illuminating the chamber windows with high intensity blue LEDs ($\sim$ 455 nm). These lights are very efficient at the de-absorption of the rubidium from the glass windows and provide a reliable source for loading the MOT. The de-absorption of the rubidium increases the pressure in the chamber during loading; however, the rubidium quickly re-absorbs when the lights are turned off so the pressure drops once the trap is loaded.

5.2 ^{87}Rb Energy Level Structure

The electronic ground state structure of rubidium is [Kr]$5s^1$, indicating a single valence electron. Since the remaining electrons are in closed shells, they do not contribute to the total angular momentum of the atom. As a result, rubidium has a hydrogen-like electronic structure. The fine structure from spin-orbit coupling splits the excited $5p$ state into two levels with total electronic angular momentum, $\mathbf{j} = \mathbf{l} + \mathbf{s}$, having values of $\frac{1}{2}$ and $\frac{3}{2}$ where $\mathbf{l}$ is the electronic orbital angular momentum and $\mathbf{s}$ is the electronic spin angular momentum. In the standard Russell-Saunders notation these are designated $5^2P_{1/2}$ and $5^2P_{3/2}$, while the ground state is designated as $5^2S_{1/2}$. The transition to these two states from the ground state are known as the D lines. The transition from $5^2S_{1/2}$ to $5^2P_{1/2}$ is known as the D_1 line (λ = 794.9 nm) and the transition from $5^2S_{1/2}$ to $5^2P_{3/2}$ is known as the D_2 line (λ = 780.241 nm). The remainder of this section will discuss the D_2 line, since it is the relevant transition

for laser cooling and imaging of ^{87}Rb. It is depicted in Fig. 5.2. Taking into account the coupling of the nuclear spin, $\mathbf{i}$, with the total electronic angular momentum, the $5^2S_{1/2}$ and $5^2P_{3/2}$ states split into states of total atomic angular momentum, $\mathbf{f} = \mathbf{i}+\mathbf{j}$. The nuclear spin of ^{87}Rb is $\frac{3}{2}$, giving the $5^2S_{1/2}$ electronic ground state two hyperfine states with a total atomic spin of $f = 1$ and $f = 2$. Similarly, $5^2P_{3/2}$ has hyperfine states of $f' = 0, 1, 2, 3$ [73, 107].[1] Dipole-allowed transitions between the ground and excited state manifolds are used for laser cooling. The strongest transition of the manifolds is the σ^+ polarization transition connecting the $|f = 2,\ m_f = 2\rangle$ state to the $|f' = 3,\ m'_f = 3\rangle$. Atoms in the $|f' = 3,\ m'_f = 3\rangle$ state can only decay to the $|f = 2,\ m_f = 2\rangle$ state, allowing for the continuous cycling on this transition. It is for this reason that it is called the cycling transition. Optical pumping tends to move the atomic states towards the cycling transition in m_f states. However, the cycling on this transition is not perfect since there is a non-zero probability of off-resonant excitation to the $f' = 2$ state. The unfortunate consequence of this excitation is that the $f' = 2$ state has a 50% probability of decaying to the $f = 1$ ground state. The result is that the off-resonant transition probability for the cycling transition light to excite the atom back into the excited state manifold is negligible. The off-resonant excitation of atoms to the $f' = 2$ manifold is often called the depumping transition since it removes atoms from the cycling transition. Fortunately, a second laser can be used to excite the $f = 1$ to $f' = 2$ transition to repump the lost atoms back into the optical pumping scheme leading to the cycling transition. The cycling transition and repump transition are the two most important laser frequencies needed for the MOT and for imaging.

[1] Excited state f numbers are typically denoted with primes.

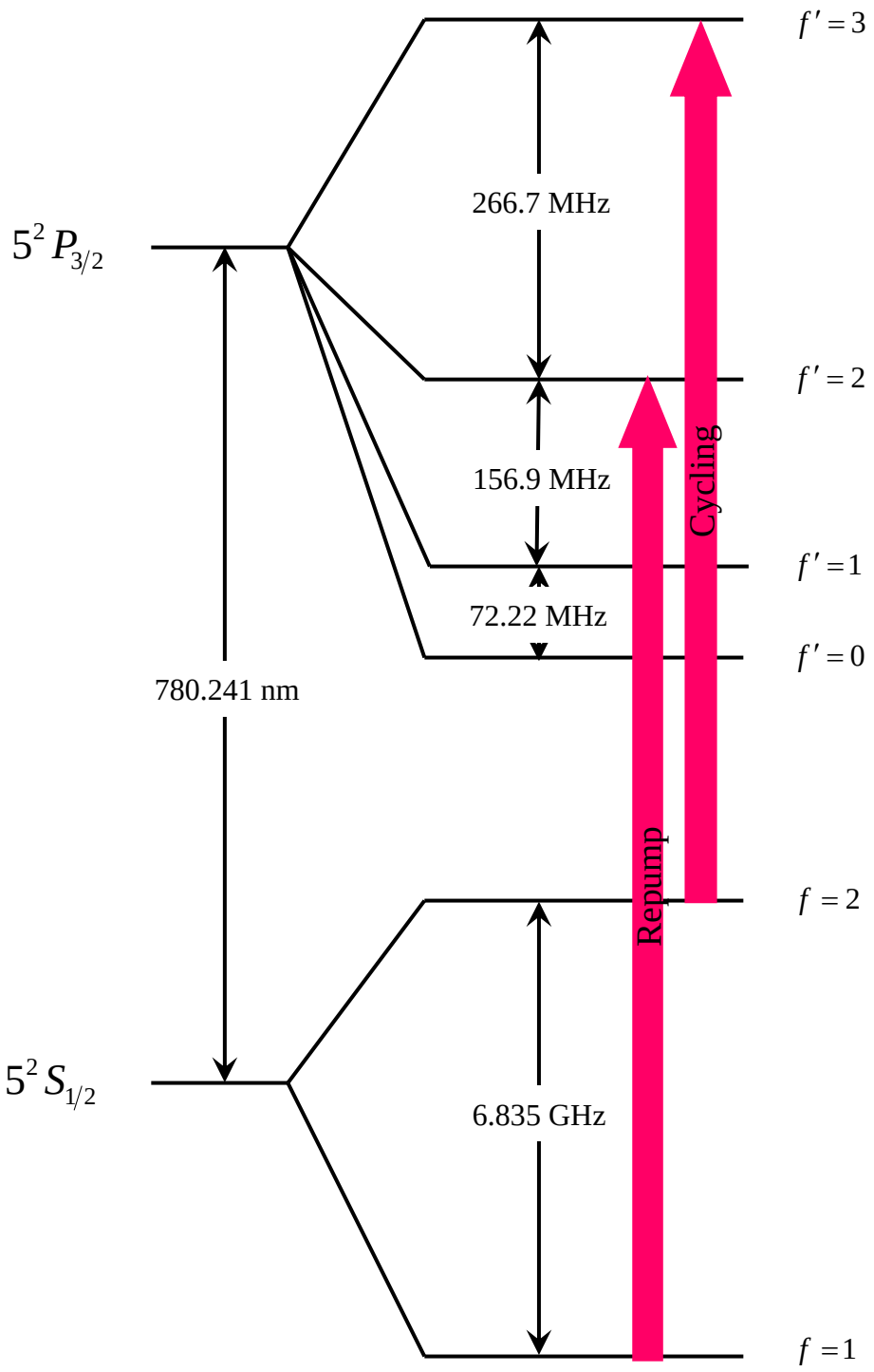

Figure 5.2: ^{87}Rb D_2 line. Shown here is the D_2 line for ^{87}Rb. The "repump" transition is from the $f = 1$ to the $f' = 2$ line, and the "cycling" transition is from the $f = 2$ to the $f' = 3$ line.

5.3 Magneto-Optical Trap

The MOT is formed using a set of anti-Helmholtz coils and lasers near the ^{87}Rb D_2 line cycling and repump transitions. The cycling transition lasers are in a $\sigma^+ - \sigma^-$ configuration on three orthogonal axes using retro-reflected beams [107]. The typical laser power per beam at the chamber is $30 - 35$ mW, collimated with a ~ 15 mm waist, and clipped into a top-hat profile with a diameter of ~ 25 mm. The repump laser has the same top-hat profile, but it is only on the up/down (gravity) axis of the MOT beam configuration and has ~ 15 mW of power. The repump is combined with the cycling transition using a polarizing beam cube, so its circular polarization is opposite of the cycling transition.

5.3.1 MOT Laser Set-up

Saturated absorption spectroscopy is used to stabilize the lasers to the frequencies of the atomic transitions [108], which uses a strong pump pump beam counter-propagating with a weak probe beam to overcome the Doppler broadening in a room temperature vapor cell used as the atomic reference. This technique provides a narrow peak for each transition frequency on top of the Doppler absorption feature.[2] A useful feature of saturated absorption spectroscopy is that halfway between each pair of transitions is a cross-over peak. These peaks are usually larger in amplitude than the peaks of the actual transitions and provide excellent locking points. The saturated absorption spectrum is converted into an error signal via frequency modulated spectroscopy (FM spectroscopy), and that error signal is used to lock the laser directly on the peaks of the spectroscopy [108].

The lasers for the cycling transition employ a complicated frequency shifting scheme using an optics setup depicted in Fig. 5.4 in order to produce the relatively

[2]The narrowness of the saturated absorption peak is limited by the transition linewidth of ~ 6 MHz but is typically a few times larger. This is still much narrower than the Doppler profile which is ~ 1 GHz for rubidium at room temperature.

large range of detunings required by the experiment. Laser light from an external cavity diode laser (ECDL) master oscillator is frequency shifted up 160 MHz by an acousto-optic modulator (AOM) (Fig. 5.3 red arrow, Fig. 5.4 AOM 1) which is used to offset the lock of the master laser from the lock point of the $f' = 1 - f' = 3$ crossover resonance.

The beam from the master laser is then double-passed through variable frequency AOM (Fig. 5.3 green arrow, Fig. 5.4 AOM 3) to seed an injection locked diode laser (ILDL). The frequency shift from AOM 3 varies from 2×140 MHz to 2×238 MHz. The ILDL is then used as the seed for the tapered amplifier (TA). The output of the TA is passed through a final AOM to control the power and is divided into three fibers going to the experimental chamber. This AOM also shifts the frequency of the light down 110 MHz (Fig. 5.3 purple arrows, Fig. 5.4 AOM 4). A low power probe beam for absorptive imaging is also derived from frequency shifting the master laser. It is switched on and off using a double-passed AOM operating at 186 MHz (Fig. 5.3 orange arrows, Fig. 5.4 AOM 2).

A second ECDL seeds another ILDL used for repump laser light (Not shown in Fig. 5.3 or Fig. 5.4.) The power from this ILDL delivered to the experiment is controlled by an AOM. The frequency of the repump laser is far simpler than that of the cycling transition. The lock used for the repump is shifts the laser light 80 MHz from the resonance. The control AOM then shifts the light 80 MHz back to resonance.

All of the light beams have a shutter to eliminate any light that may leak through the AOMs at undesired times. This setup is essentially unchanged since circa 2001 [47, 68]. In summary, the result of the laser setup is light on the ^{87}RB D_2 manifold connecting the ground state electronic state $5^2S_{1/2}$ to the excited state $5^2P_{3/2}$. The MOT cycling transition master laser varies from ~ 6 MHz red of the cycling transition $5^2S_{1/2}\ f = 2 \rightarrow 5^2P_{3/2}\ f' = 3$ to ~ 200 MHz to the red. (which is also ~ 65 MHz blue

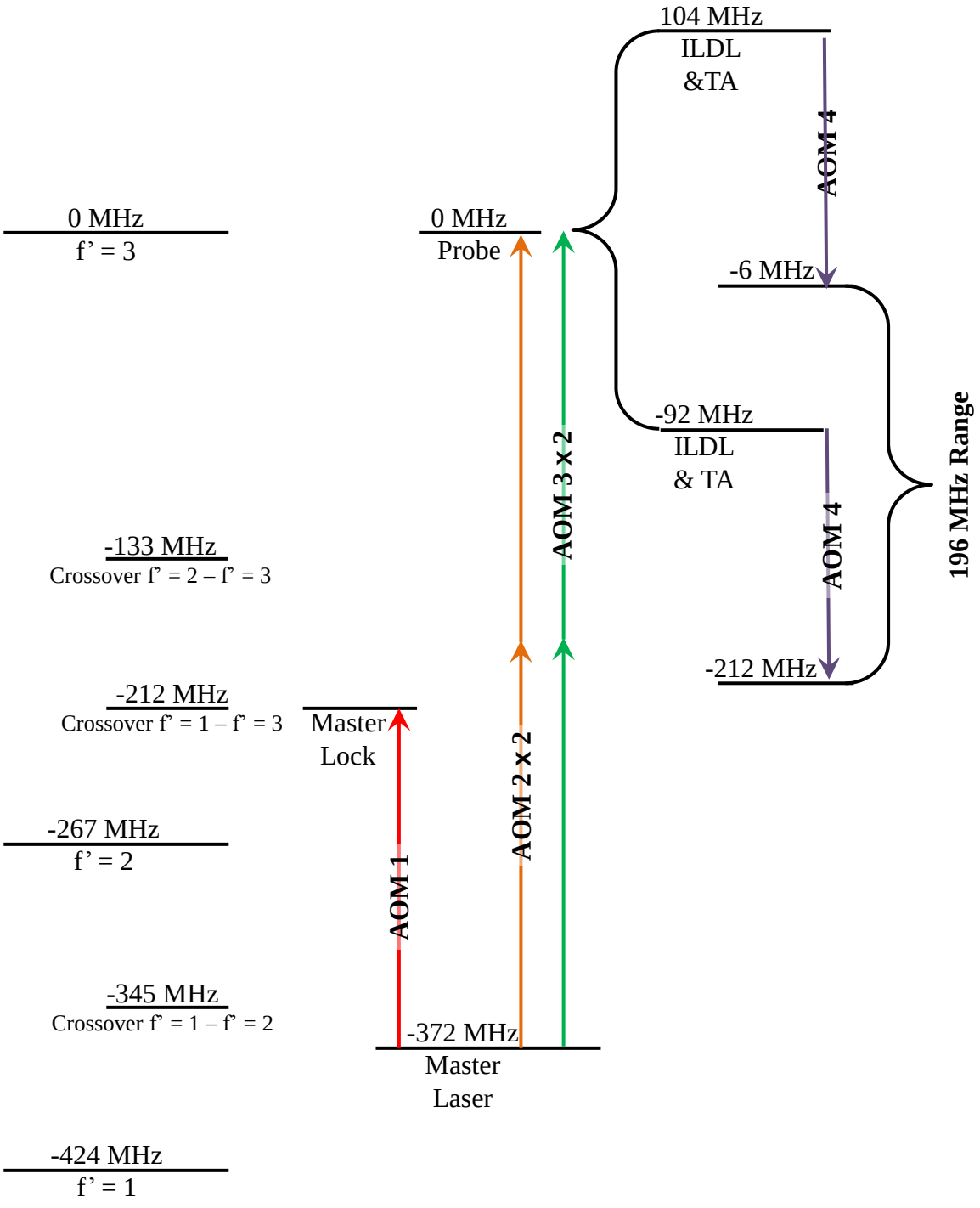

Figure 5.3: Frequency shifts for the MOT laser lock. Shown here are the different frequency shifts for the MOT laser lock. Each shift is labeled with the appropriate AOM responsible for the shift in Fig. 5.4. A double arrow represents a double-passed AOM, while a single arrow represents a single frequency shift.

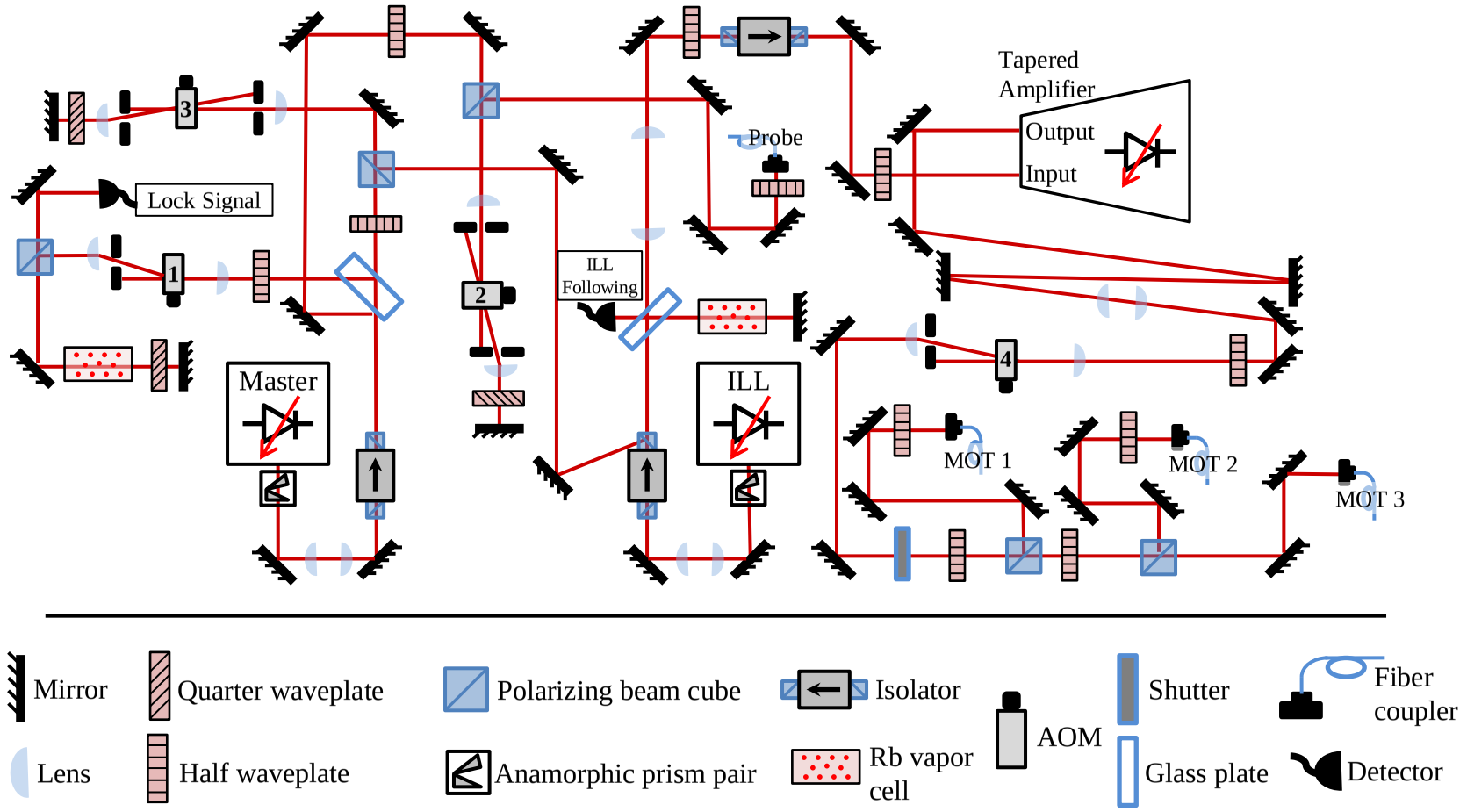

Figure 5.4: MOT cycling laser schematic. Shown here is the schematic of the cycling transition for the MOT lasers. The AOMs are labeled to correspond to the specific frequency shifts indicated in Fig. 5.3.

of the depumping transition $5^2S_{1/2}\ f = 2 \rightarrow 5^2P_{3/2}\ f' = 2$). The weak absorptive probe is on the cycling transition to within 0.1 MHz. The repump laser stays on resonance for the $5^2S_{1/2}\ f = 1 \rightarrow 5^2P_{3/2}\ f' = 2$ transition.

5.4 Dipole Force Trapping

The dipole force trapping laser is an Coherent GEM series industrial CO_2 laser at 10.6 μm with a 100 W continuous output power. The trap operates in the regime of the quasi-electrostatic trap (QUEST) where the AC polarizability of the trapped atom is approximately the DC polarizability [47, 68, 109]. The CO_2 laser power delivered to the experiment is controlled by an AOM. The beam is aligned through the ZnSe optics of the chamber in a horizontal direction. The AOM control of the laser power is carefully calibrated in order to control the main trapping beam power from 5 mW to 50 W of power going through the chamber. The beam path incorporates a telescope with a motor-actuated zoom lens that allows for the size of the beam waist at the focusing lens to be varied, thus varying the waist of the trap at the focus inside the chamber. The waist size varies from $\sim 20 - 120$ μm, depending on the stage of the experiment. Further details of dipole force trapping with the CO_2 laser are described in Ref. [47].

In Section 2.2 the single mode approximation was made which made the derivations of the dynamical equations easier. In order to create the tightly confined traps that make the SMA a valid assumption, a second dipole force trapping laser oriented perpendicular to the main CO_2 trap is required. This second dipole force trapping laser is an 852 nm diode laser that provides up to 30 mW of power at the experimental chamber. The light from the 852 nm cross trap is in the far off resonant trap (FORT) regime [109]. Like many of the other lasers, its power is controlled by an AOM and it has a shutter to block leakage during imaging. The 852 nm cross trap laser beam is fiber coupled to a fixed-focus setup aligned across the main trapping beam. The

beam alignment is very delicate, as the cross trap has a waist of 20 μm, and its focus must cleanly intersect the 20 μm waist of the main trapping beam at its focus. The combination of the two dipole force trapping lasers at the proper power produces a nearly spherical trap geometry with nearly equal trap frequencies in each direction. Additionally, its size is such that the SMA is valid.

5.5 Microwave and RF Systems

The lasers described in Section 5.3.1 primarily interact with the electric dipole moment of the valence electron. However, the experiment requires transitions between sublevels that are electric dipole forbidden, so alternative techniques are needed to excite these transitions. Oscillating magnetic fields can be used to interact with the magnetic dipole moment of the valence electron. Within the electronic ground state hyperfine manifold the magnetic dipole transitions are accessible by using microwaves which connect the $f = 1$ to $f = 2$ (red, green, and blue arrows in Fig. 5.5) and RF which connect Zeeman sub-levels within the same f state (gray arrows in Fig. 5.5). Access to these transitions is useful for magnetic field measurements, state preparations, and the measurement used to reconstruct the phase space. The general schematic for the microwave system is shown in Fig. 5.5. The microwave system starts by taking frequency reference from a GPS receiver which produces a 10 MHz reference signal. The reference signal is taken by a Hewlett Packard E4422B frequency synthesizer set to one half of the microwave frequency of 6.835 MHz. This is done for two reasons: the synthesizer used was limited to 4 GHz in output, and the Mini-Circuits ZASWA-2-50DR RF switch used to control the synthesizer leaks above 5 GHz. After the switch, the frequency is doubled using a MARKI Microwave D0204LA passive doubler. The signal then passed through a Midisco M314080 isolator enroute to an ALGA Microwave 12 W amplifier. After the amplifier the signal is sent to the microwave horn located above the experimental chamber. The microwave

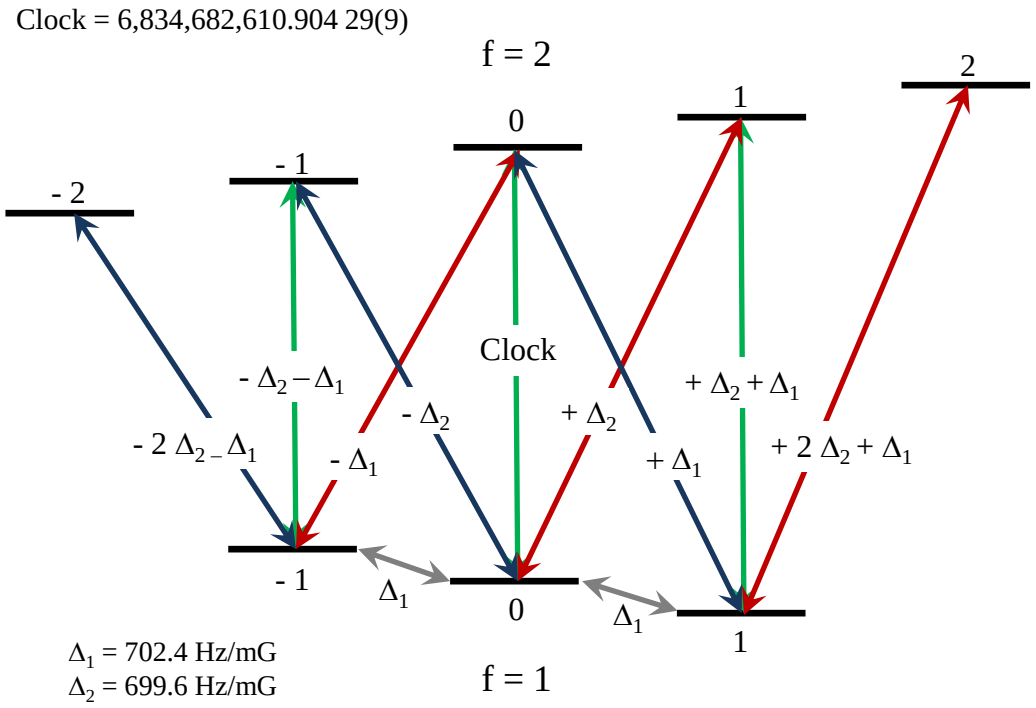

Figure 5.5: Microwave and RF transitions. Shown here are the different frequency shifts for the microwave and RF transitions. The transitions between the $f = 1$ and $f = 2$ levels are indicated as differences from the clock transition, while the transitions within the sublevels (e.g. $f = 1$, $m_f = 0$ to $m_f = 1$) are given as the resonant frequency.

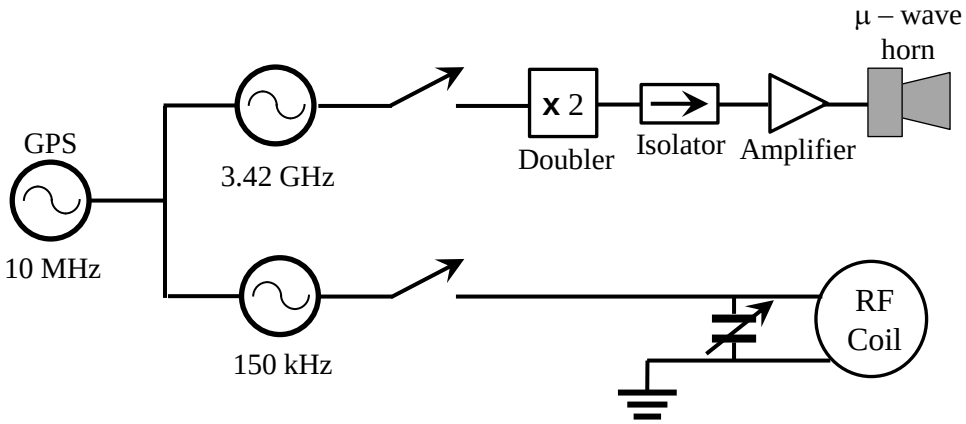

Figure 5.6: Schematic of the microwave and RF control system. Shown here is the microwave and RF control schematic. Each system is referenced to a 10 Mhz signal provided by GPS.

horn is a right circular cylinder of copper with a diameter 1.5". The microwave system is capable of Rabi rates of 20 kHz when driven at the maximum amplifier output power of 12 W.

The general schematic for the RF system is also shown in Fig. 5.5. The Stanford Research Systems DS345 function generator for the RF uses the same 10 MHz GPS reference. The function generator drives the RF coil directly through a Mini-Circuits ZYSWA-2-50DR RF switch. Though the power is limited to 100 mW by the switch, the system is capable of obtaining Rabi rates of 2.5 kHz. The RF is coupled to the atoms by a simple two-turn coil placed on top of the chamber centered on the large window. The required frequency for the RF transitions varies with the magnetic field ($\Delta_1 = 700$ Hz/mG). For the typical magnetic field bias used in this experiment the RF frequency was ~ 200 mG $\times$ 700 Hz/mG ~ 150 kHz. The amplitude of the oscillating magnetic field is increased by operating the coil in parallel with a 90 nF capacitor. The capacitor is tuned such that coil-capacitor circuit forms a resonator at the desired operation frequency $\sqrt{LC} = (2\pi \times 150 \text{ kHz})^{-1}$. This results in a ring up/down time of ~ 10 μs, which is small compared to the typical pulse time of ~ 100 μs.

5.6 Imaging System

The imaging configuration used to take all of the data in this thesis is a $4f$ imaging system. The primary type of imaging used was fluorescence imaging, while absorptive imaging was used for certain diagnostics. The details of these techniques, along with their noise and calibration, are covered extensively in Ref. [69].

5.6.1 Fluorescence Imaging

For fluorescence imaging, resonant or near resonant laser beams are directed at the atoms from the side of the imaging path (See Fig. 5.7 **(a)**). When the light interacts with the atoms, they fluoresce. The fluorescence is collected by the imaging system so

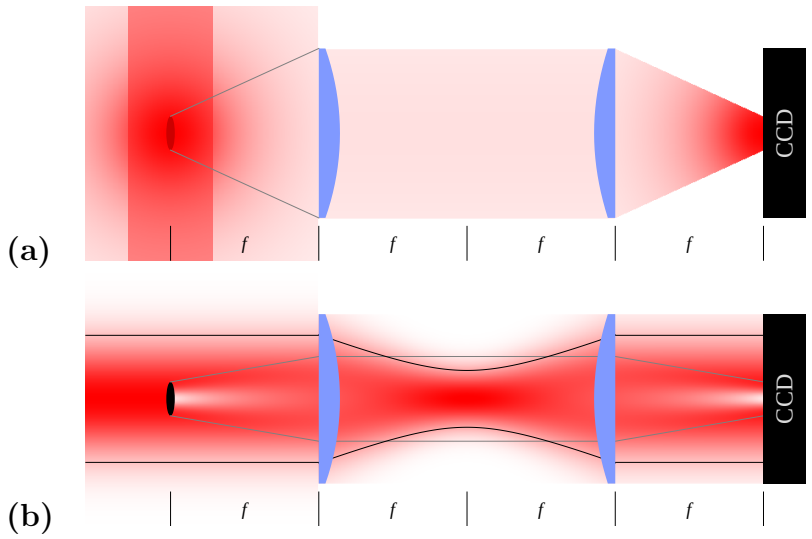

Figure 5.7: Imaging configurations. Shown here are the imaging configurations used in the experiment. **(a)** shows the configuration for fluorescence imaging, while **(b)** shows the configuration for absorptive imaging. All of the data in the results portion of this thesis used fluorescence imaging. Absorptive imaging was used for experimental diagnostics.

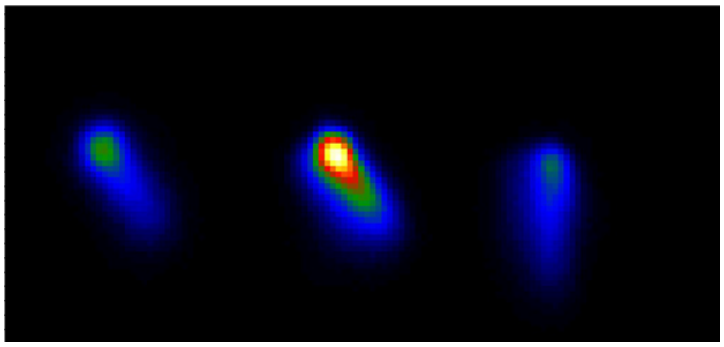

Figure 5.8: Fluorescence image of BEC. Fluorescence image of a spin-1 BEC. The component clouds are forced apart using a Stern-Gerlach field during time-of-flight expansion. The condensate is fluoresced with resonant light for 400 μs.

that the scattered photons can be counted. Here the two lenses merely act to image the fluorescing atoms onto the CCD camera. The collection efficiency is limited by the apertures of the system. Spatial resolution is limited by atomic motion due to heating and pushing from the beams used to fluoresce the atoms. This is a more significant problem for fluorescence imaging as compared to absorptive imaging since the exposure to the resonant light usually needs to be longer than absorptive imaging to collect enough photons. Also, fluorescence imaging is more sensitive to light scattering into the imaging path that is not from fluorescing of the atoms. This technique does not, however, suffer from interference noise typical of absorptive imaging since the fluoresced light is not phase coherent. This technique is very good at counting atoms due to its linear response to the number of atoms.

5.6.2 Absorptive Imaging

For absorptive imaging, a probe beam of resonant light is directed towards the imaging system from behind the atoms (See Fig. 5.7 **(b)**). The atoms absorb the light and cast a shadow. This shadow propagates as a combination of modes subtracted from the probe beam. The image of the shadow of the atomic cloud is compared to a reference image of the probe light when no atoms are there in order to determine the optical depth of the atomic cloud. The optical depth is related to the column density of the atomic cloud, which can be summed to determine the number of atoms. The determination of the optical depth, however, is non-linear in the column density and depends on the probe beam intensity. The absorptive imaging technique has a high spatial resolution, though, because the atoms do not move much during the imaging since the probe pulses are short. However, a challenge of absorptive imaging is that the laser light passes through multiple optical elements, and as a result interference patterns may result which could limit final image quality.

Both of these techniques use resonant light on the cycling transition. However,

the majority of the atoms being imaged are in the $f = 1$ state. Consequently, in order to image the atoms in the $f = 1$ state as well, the repump beam is turned on at the same time as the probe/fluoresencing beams so that the $f = 1$ atoms will absorb/fluoresce with the $f = 2$ atoms. In the event that one only wanted to count the atoms in the $f = 2$ state, then (e.g. when doing microwave spectroscopy), the repump would be turned off such that only the $f = 2$ atoms would absorb/fluoresce.

5.7 The Control System

The control system of the experiment was complete redesigned in the last two years. The control computer was upgraded to a new Windows 7 machine employing a Core i-7 processor with twelve threads and 16 GB of RAM. The control computer was moved away from the control center to accommodate the addition of a Magma 7-slot PCI chassis for controlling the numerous PCI cards needed for the experiment. All of the control cables were rerouted using cable trays a reasonable distance from electrical lighting to reduce noise from that source. The information display system was also upgraded with two stacked 24" wide-screen monitors.

The experimental sequence is controlled using Labview software to control the National Instruments analog and digital output cards in the PCI chassis. The entire Labview control software was upgraded when the new control computer was brought online, simplifying control of the entire experiment. The system has two analog output boards with a total of 16 channels. The analog boards control various signals such as the bias and gradient coil currents, laser detuning and power, and getter current. The system has one digital output card with 24 channels. The digital channels control various RF switches, shutters, triggers for cameras, and pulse generators, amongst other things. The control computer is connected to function generators, pulse generators, and lens movers through GPIB and RS-232 controllers for updating the values. Additionally, a frame grabber captures a digital images from an analog

camera for use in trap loading diagnostics. The values of each channel are updated using a spreadsheet interface that allows for flexibility and adaptability to the large number of experiments conducted in the lab.

5.8 Basic Experimental Sequence

The spreadsheet interface used to update channel values discussed Section 5.7 controls every aspect of the experimental sequence. The general sequence contained in the spreadsheet is summarized below.

The experimental sequence begins by loading the main optical dipole force trap. This starts with the MOT laser light and coils on, the blue LED lights on, and the CO_2 trapping laser on at full power with the zoom lens positioned such that the dipole trap has a large waist to maximize overlap. The MOT loads for 15 s, at which point the number of atoms in the MOT saturates. Once this happens, the atoms are loaded into the optical dipole trap using a temporal dark MOT sequence. The MOT gradient coil current is cut in half, the cycling transition laser power is halved, the repump power is lowered to a few tens of μW, and the detuning of the cycling transition laser is adjusted as far to the red as the control system will allow.[3] While in this transient condition, the MOT collapses along the direction of the repump light (gravity direction) into a pancake shape. The exact location it collapses to is sensitively dependent on the final repump power.[4] The final cloud loads the optical dipole force trap with 10-15 million atoms at $\sim$30 μK with an equal distribution of m_f states within the $f = 1$ manifold.

With the optical dipole force trap loaded, all resonant light is extinguished and

[3]The optimization of the temporal dark MOT sequence is empirically determined. The final gradient and cycling transition intensity both have some effect on loading and the optimum values vary from no change to half of their MOT values. The effect on the loading from the detuning is stronger and has always been optimized for the farthest red from the cycling transition as the control system can reliably produce.

[4]The efficiency of the loading is very sensitive to the final power for the repump laser, which has to be checked daily.

evaporative cooling begins. Evaporation is accomplished in two ways. The trap power is lowered slowly (compared to the inverse of the trap frequencies), allowing the hotter atoms to escape, thereby lowering the overall temperature. If this were the only technique used for a dipole force trap with a large waist, the re-thermalization rate, and hence the evaporative cooling rate, would slow too much and there would be insufficient cooling to reach the BEC transition temperature. So the zoom lens moves simultaneously, changing the geometry of the trap to a smaller waist which maintains the radial trap frequencies and thus re-thermalization rate. This creates a BEC with over 100,000 atoms after 2 s of evaporative cooling.

During evaporation, magnetic biases and gradients are typically applied to influence the m_f populations of the final BEC. In order to create a $m_f = 0$ condensate, a relatively large gradient of 20 G/cm is applied along the weak trapping direction of the main trapping beam. This pulls the $m_f = \pm 1$ components towards more weakly trapped regions, causing them to be lost preferentially while maintaining thermal equilibrium with the other m_f states. To create a condensate of $m_f = \pm 1$, the gradient is oriented along the gravity direction. Because of this alignment, one of the states is levitated against gravity and the other is pushed with it, causing the levitated state to be kept preferentially. In this case, the $m_f = 0$ component is neither levitated or pushed down and usually leaves some residual amount. It is possible to selectively push out this residual component using microwave transitions and resonant light.

After the gradient is ramped down, the secondary dipole force trap, if used, is ramped up. For the cross trap configuration, the secondary dipole force trap remains on throughout the remainder of the experimental sequence. Further evaporation cools the atoms to well below the BEC transition temperature whereby the ground state of the trapping potential is macroscopically occupied.

Dynamical evolution of the internal states of the BEC would occur ever before evaporation is complete unless it is prevented. During the creation of the BEC a

bias field of 2 G is applied to prevent this dynamical evolution. Evolution of the condensate is initiated by rapidly lowering the magnetic field bias. After the bias is lowered, the initial state can be further prepared by performing microwave and RF manipulations, as necessary. These manipulations are not performed until the ramp is complete since the microwave and RF frequencies are magnetic field dependent. The field ramp takes 10-15 ms to reach the necessary stability of $\sim$ 200 mG to use the microwaves and RF. The manipulations themselves take a few hundred microseconds. Most of the experiments in this thesis use an initial state of $m_f = 0$ with no state preparation. After the preparation, the BEC is allowed to evolve freely in the trap for time intervals varying from 0 to a several seconds. Following this evolution, the the microwaves and RF may again be used to prepare the state for measurement. At this point, the trapping lasers are shut off and the atoms are allowed to fall and expand for 5-20 ms. During this time of flight (TOF), a gradient is turned on again to spatially separate the final m_f projections. At the end of this expansion one of the two imaging techniques discussed in Section 5.6 is used to count and spatially resolve the expanded atom clouds. The system is then reset for another data run. In total, the experimental procedure just described takes $\sim$25 s.

CHAPTER 6

MAPPING THE PHASE SPACE

This chapter will focus on the study of the phase space of a spin-1 ferromagnetic BEC. It will rely on the key observations made in Section 4.1 when discussing the simple classical pendulum. Those observations were that one can estimate where in the phase space that orbit is at any time based on the shape of the parametric plot of the angular displacement, and that the period of the orbit decreases as you move away from the separatrix.

In this chapter, the conjugate variables of the fractional population in the $m_f = 0$ sublevel, ρ_0, and the spinor phase, θ_s, for the condensate will take the place of the angular displacement, θ, and the angular momentum, p_θ, for the simple pendulum. Using these variables, the spin-1 phase space for the ferromagnetic ^{87}Rb looks as depicted in Fig. 2.1 in Chapter 2. The results presented in this chapter help show the shape of the phase space by using the techniques demonstrated with the simple pendulum.

The mean-field phase space is used to demonstrate dynamics in several experimental papers involving spin-1 BECs, and more generally for the Bose-Hubbard double-well potential and internal Bosonic junctions [36, 53, 110, 111]. The shape of the phase space was used to portray the measured evolution of the system. Here, the measured evolution of the system is used to portray the shape of the phase space.

6.1 State Preparation and Measurement Protocol

As was discussed in Chapter 5, the condensate is initialized in a pure $m_f = 0$ state. In the experiments to be discussed in Chapter 7, the system will be allowed to freely evolve from this state through spin mixing. However, for the experiments in this

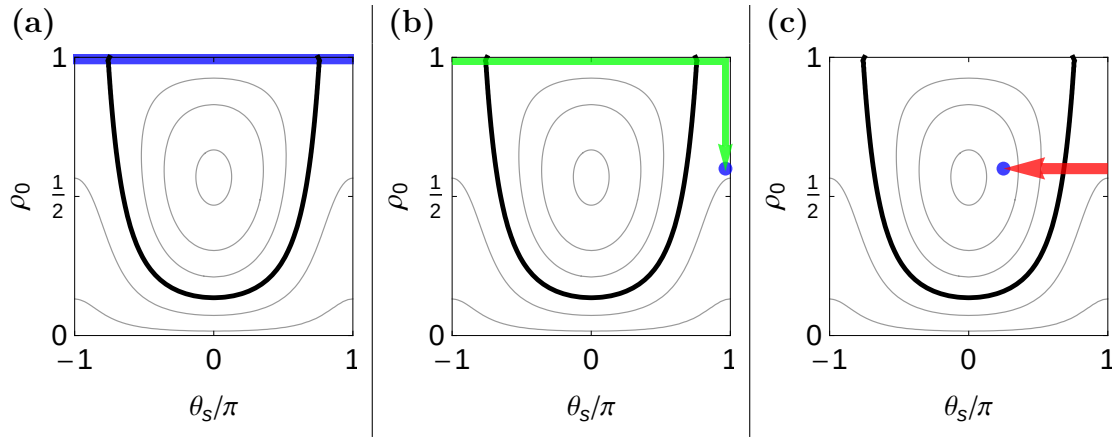

Figure 6.1: Phase space schematic of state preparation. The state preparation of the condensate for the phase space mapping begins **(a)** with the condensate in the $m_f = 0$ state. **(b)** Shows an RF rotation that then takes the state from $\rho_0 = 1$ with random θ_s to the desired value of ρ_0 with $\theta_s = \pi$. **(c)** Shows the final step in the process, an off-resonant microwave pulse to shift the condensate to the desired θ_s.

chapter, the evolution of the system will be measured from different initial points in the phase space. As a result, the initial $m_f = 0$ state has to be arbitrarily shifted to the desired state when needed. This is done with a combination of RF rotations and microwave spinor phase shifts. The general process for state preparation is to first initialize the system in the $m_f = 0$ state by preparing the condensate in a high magnetic field ($\sim$ 2 G) where the ground state is $m_f = 0$. Then, the magnetic field is rapidly lowered to the final value ($\sim$ 200 mG), leaving the system in the $m_f = 0$, which is at a hyperbolic fixed point in the spin-nematic phase space. In the $\rho_0 - \theta_s$ phase space this corresponds to the initial distribution being spread across the top of the phase space ($\rho_0 = 1$, while θ_s is random, see (See Fig. 6.1 **(a)**).

State preparation begins once the magnetic field reaches stable levels ($\sim$15 ms after the quench). First, the system undergoes an RF rotation to shift the value of ρ_0 from 1 to the desired "final" value, in the process it picks up a spinor phase of π (See Fig. 6.1 **(b)**). Then, the spinor phase is adjusted to its "final" value with an off-resonant microwave pulse (See Fig. 6.1 **(c)**). In total, this process takes less than $\sim$150 μs. The system is then allowed to freely evolve.

Measurement of the system is done at varying evolution times, usually every $10-15$ ms in accordance with the imaging techniques discussed in Chapter 5. The results are then compared to dynamical simulations under the same conditions.

6.2 Surveying the Phase Space by Changing θ_s

In Section 4.1 the period of the simple pendulum was determined for different values of the angular momentum at a fixed value of the initial angular displacement. The location of the separatrix was clearly visible in Fig. 4.5. The $\rho_0-\theta_s$ phase space can be similarly surveyed. The first such survey consisted of a series of measurements of the period of orbit across a horizontal line at $\rho_0 \sim 0.6$ (See Fig. 6.3 **(a)**). The results of the period measurement are shown in Fig. 6.3 **(b)**. The location where the survey crosses the two manifolds of the separatrix are clearly visible. In addition to identifying the location of the two manifolds of the separatrix, the period measurements can be used to map the energy contours they follow. By aligning the data points with simulation results, a spinor phase can be directly inferred from the shape of the parametric plot, just as in Section 4.1 with the simple pendulum. The results for five of the survey points are shown in Fig. 6.2. For each block of the figure, the left image shows the fitting of the parametric plot of ρ_0 to the simulation. The right block then shows the location of one orbit of data points with its' inferred spinor phase on the $\rho_0-\theta_s$ phase space, along with the simulation trajectory.

6.3 Surveying the Phase Space by Changing ρ_0

The second survey of the phase space consisted of a series of measurements of the period of orbit along a vertical line at $\theta_s \sim 0$ (See Fig. 6.4 **(a)**). The results of the period measurement are shown in Fig. 6.4 **(b)**. The location where the survey crosses the main manifold of the separatrix is clearly visible. The results for five of the survey points are shown in Fig. 6.5. For each block of the figure, the left image shows the fitting of the parametric plot of ρ_0 to the simulation. The right block then shows the

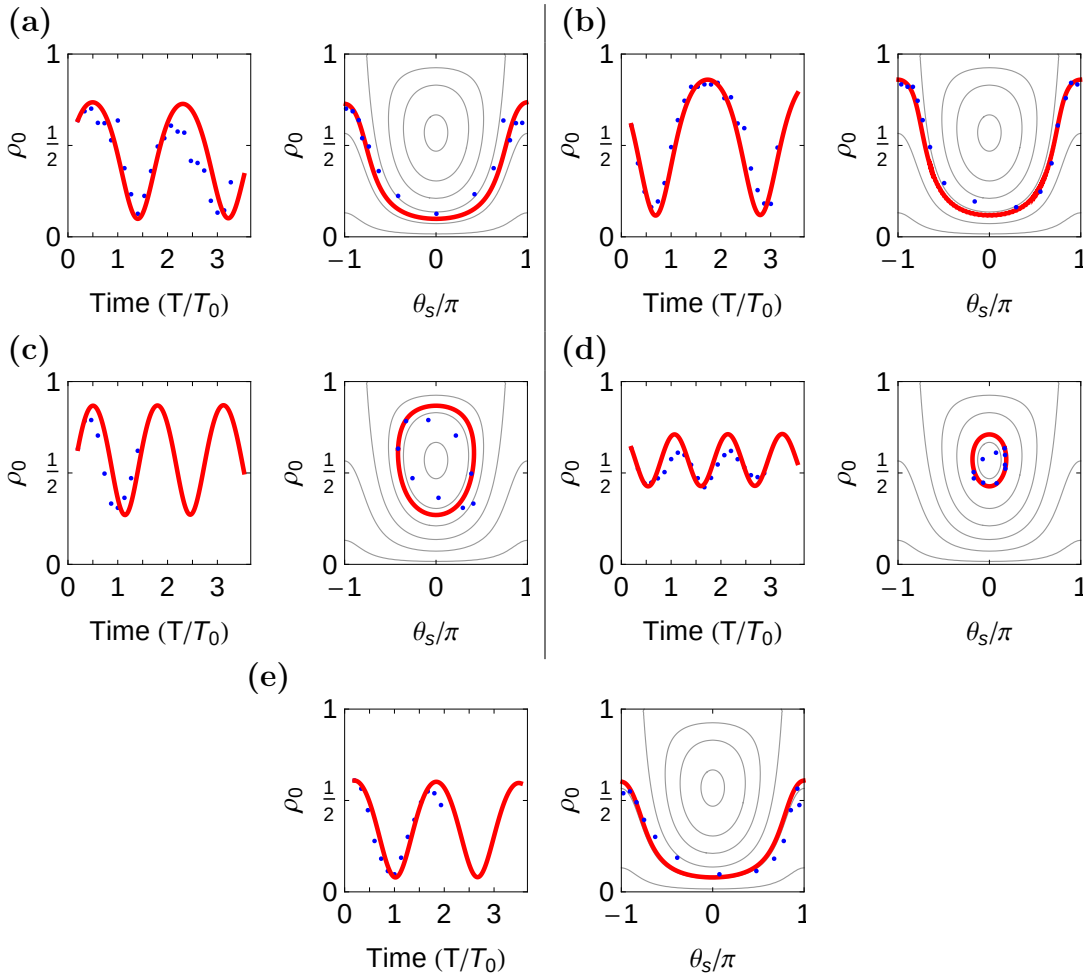

Figure 6.2: Mapping the phase space energy contours 1. Each section shows the parametric plot of ρ_0 fit to the simulation, and the measured trajectories and the simulation results overlayed on to the $\rho_0 - \theta_s$ phase space. Each trajectory follows an energy contour in the phase space, so the measurements are effectually mapping the energy contours directly. The trajectories shown are for initial spinor phase values of: **(a)** $\theta_s \sim -0.85\pi$, **(b)** $\theta_s \sim 0.75\pi$, **(c)** $\theta_s \sim -0.40\pi$, **(d)** $\theta_s \sim 0.20\pi$, and **(e)** $\theta_s \sim \pi$. In each plot, the red line represents the results of the best-fit for the theory.

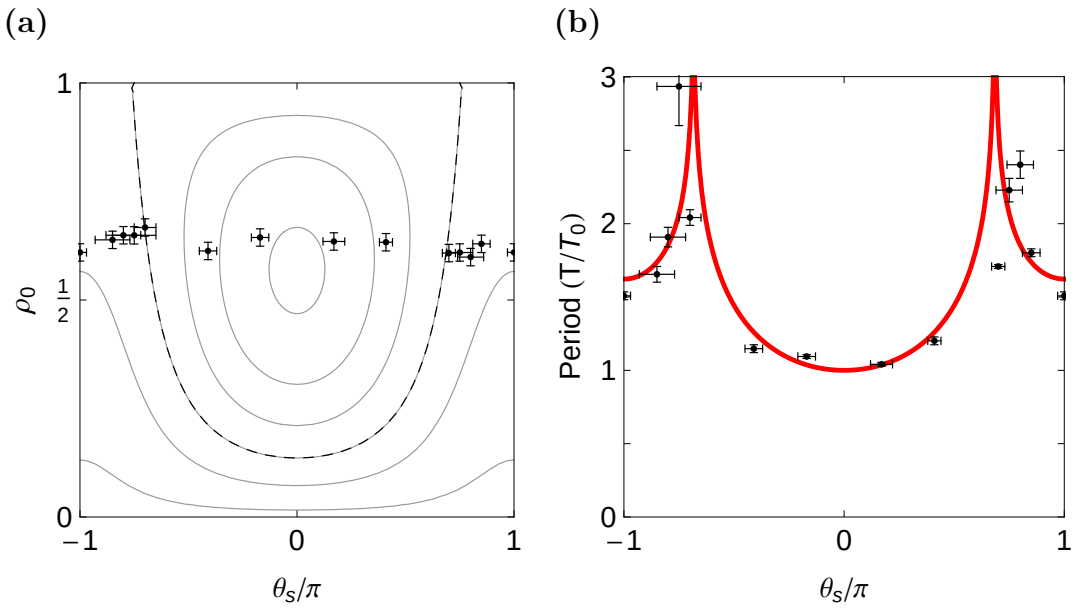

Figure 6.3: Changing θ_s to survey the phase space. **(a)** The $\rho_0 - \theta_s$ phase space was surveyed across the $\rho_0 \sim 0.6$ line by measuring the period of oscillations at different locations. **(b)** shows the results of the measurements compared to the dynamical simulations. T_0 is the period of oscillations for orbits slightly displaced from the ground state, $T_0 \sim 75$ ms. The red line represents the best-fit of the theory.

location of one orbit of data points with its' inferred spinor phase on the $\rho_0 - \theta_s$ phase space, along with the simulation trajectory.

6.4 Concluding Remarks

In all of the plots contained in this chapter, there is reasonable agreement, with some trajectories showing better agreement than others. Experimental runs initialized near the separatrix showed a large standard deviation for these states due to dispersion caused by differing periods. The simulations also showed this same effect, with large standard deviations in ρ_0 being common.

As stated, the results shown are in good overall agreement with the predictions of the dynamical simulation. However, it is important to point out that the simulation results shown are not at the exact experimental conditions. A small discrepancy between the measured magnetic field in the experiment and the "best-fit" magnetic field

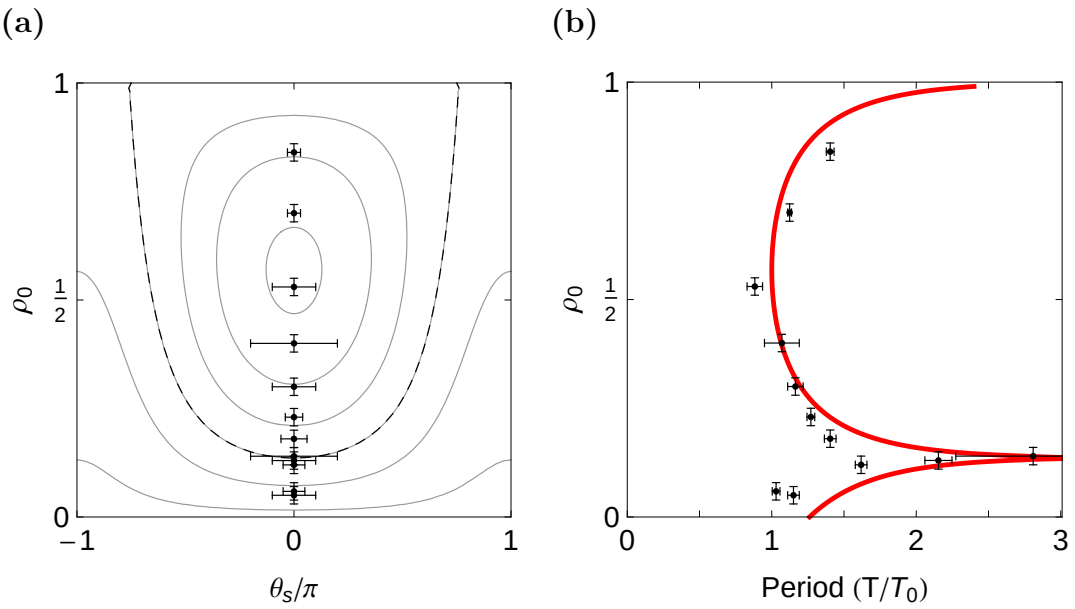

Figure 6.4: Changing ρ_0 to survey the phase space. **(a)** The $\rho_0 - \theta_s$ phase space was surveyed across the $\theta_s \sim 0$ line by measuring the period of oscillations at different locations. **(b)** shows the results of the measurements compared to the dynamical simulations. T_0 is the period of oscillations for orbits slightly displaced from the ground state, $T_0 \sim 75$ ms. The red line represents the best-fit of the theory.

for the simulations was found. The magnetic field for the experiment was measured using RF spectroscopy, and found to be ∼210 mG. The best fit for the simulation with the data was with a magnetic field of 165 mG.

There are several possible explanations for the discrepancy. The first is that the magnetic field changes throughout the day, and may have been measured at a point of high field in the lab. This explanation may account for $\sim 5-10$ mG of the difference, as the field has been known to fluctuate on that order throughout a measurement cycle ($\sim 1-2$ days).

A second possibility is that there were fluctuations in the trapping laser power throughout the measurement cycle, which would cause the spinor dynamical rate to change. A lower trapping laser power would result in a less-tightly confined condensate, and hence a lower spinor dynamical rate. A lower spinor dynamical rate will have the same effect on the phase space map as a lower magnetic field (See Eqn. (2.25)).

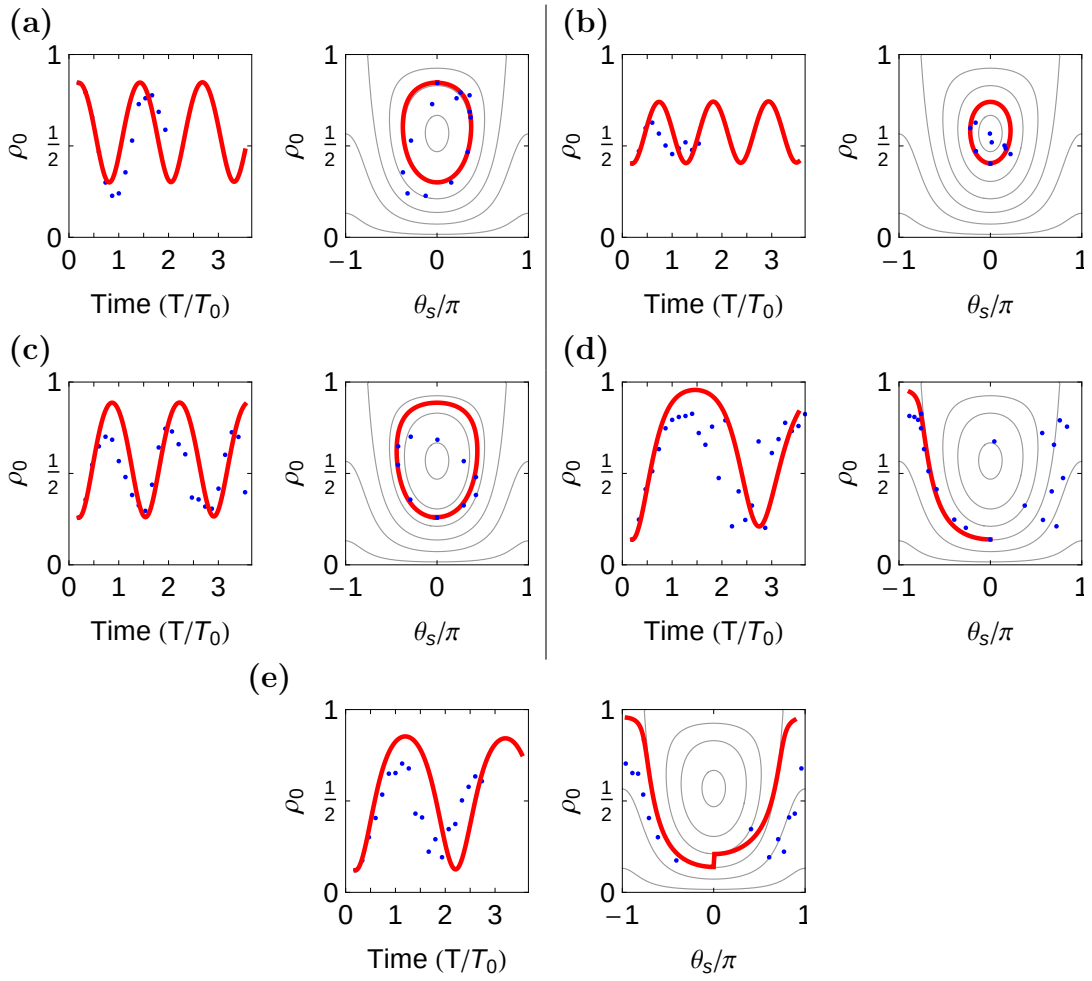

Figure 6.5: Mapping the phase space energy contours 2. Each section shows the parametric plot of ρ_0 fit to the simulation, and the measured trajectories and the simulation results overlayed on to the $\rho_0 - \theta_s$ phase space. Each trajectory follows an energy contour in the phase space, so the measurements are effectually mapping the energy contours directly. The trajectories shown are for initial ρ_0 values of: **(a)** $\rho_0 \sim 0.85$, **(b)** $\rho_0 \sim 0.40$, **(c)** $\rho_0 \sim 0.25$, **(d)** $\rho_0 \sim 0.15$, and **(e)** $\rho_0 \sim 0.10$. The discontinuity in the phase space plot of **(e)** is due to effects of the loss model used in the simulation. In each plot, the red line represents the results of the best-fit for the theory.

This may account for ~ 5 mG of the discrepancy.

A final possibility is that there was an alignment error with the 852 nm cross-trap laser. The misalignment could be either in the pointing of the beam or the location of the focus, both of which would result in a less-tightly confined trap and lower spinor dynamical rates. Another alignment concern for the cross-trap is the alignment of the polarization axis of the beam. There exists the possibility of a tensor light shift from the cross trap that would impart an effective magnetic field on the atoms. However, the effect would be small. Measurements of the effective magnetic field using RF spectroscopy for different polarization orientations of the cross-trap showed only a $\sim 5 - 10$ mG change in measured magnetic field.

CHAPTER 7

NON-GAUSSIAN EVOLUTION OF THE QUANTUM INVERTED PENDULUM

In this chapter the main experimental results of the thesis are presented. The analysis of the inverted simple pendulum in Section 4.1.1 highlighted several features of a quantum inverted pendulum that are observable in a spin-1 BEC. The simple pendulum was simulated in an inverted state corresponding to a probability distribution centered on a hyperbolic fixed point in its phase space. The pendulum was allowed to freely evolve, and its angular position was measured at a later time. The subsequent measurements create a probability distribution of the angular position for each evolution time. Fig. 4.7 and Fig. 4.9 illustrate this point clearly. The evolution of the quantum inverted pendulum is shown to be rich in non-Gaussian distributions at different evolution times. The same non-Gaussian evolution can be demonstrated in the dynamics of a spin-1 BEC. The evolution of the fractional population of atoms in the $m_f = 0$ state is measured starting from a pure $m_f = 0$ state. The rich non-Gaussian dynamics are shown to be qualitatively similar to what is seen for a quantum inverted pendulum.

The analysis of the evolution of probability distributions has been studied in several experiments [111–114]. The general purpose of these experiments was to determine the overall change in the nature of the distribution as its respective system evolved. The measured distributions in these experiments are used to provide a direct measure of the two-point correlation function, or to provide a probe of non-local correlations and entanglements in a system. This thesis will measure the evolution of the spin-1 population in the $m_f = 0$ state in order to demonstrate the detailed

distribution of ρ_0 as the system evolves.

7.1 Phase Spaces, Initial Conditions, and Evolution

The quantum Hamiltonian for the system is the spin-mixing Hamiltonian, given by Eqn. (2.20): $\hat{H}_{a,B} = \lambda_a{}' \left(\hat{S}^2 - 2\hat{N}\right) + p\hat{S}_z + \frac{q}{2}\hat{Q}_{zz}$. The mean-field Hamiltonian of the system is given by Eqn. (2.26) (for $m = 0$): $\mathcal{E} = \frac{c}{4}(1-x^2)(1+\cos\theta_s) + \frac{q}{2}(1-x)$ This Hamiltonian is in the same form as a non-rigid, momentum-shortened pendulum of length $\sqrt{1-x^2}$, where x is the conjugate momentum, similar to Hamiltonians used in double-well systems such as bosonic Josephson junctions [115–118]. Section 3.1.1.1 showed that the $m_f = 0$ minimum uncertainty initial state of the experiment can be represented as a quasi-probability distribution. This initial distribution is shown in the different phase spaces of the system in Fig. 7.1 (left). The distribution has a standard deviation $\sim \frac{1}{\sqrt{N}}$, so for $45,000$ atoms the distribution would be 1/200 atoms wide, too small to see in the figure. The illustrations shown are for 30 atoms in order to exaggerate the distribution. The bottom phase space depicted in each figure is the traditional $\rho_0 - \theta_s$ phase space with which many in the field are familiar. It is shown to be a Mercator projection of one of the hemispheres of the spin-nematic Bloch sphere representation of the phase space introduced in Refs. [38, 58]. The top phase space depicted is a polar projection of the spin-nematic phase space. Both the Bloch sphere and the spin-nematic polar projection both clearly show the initial state of the system as a probability distribution centered on the hyperbolic fixed point of the phase spaces.

As with the simple pendulum, the system here evolves along the diverging manifolds of the separatrix as shown in Fig. 7.1 (right). The subsequent measurements of the system, then, should reflect a probability distribution in ρ_0. Fig. 7.2 shows the measured evolution of the system. The figure represents the result of the collection of $\sim 10,000$ individual data points collected over the span of one week. For each

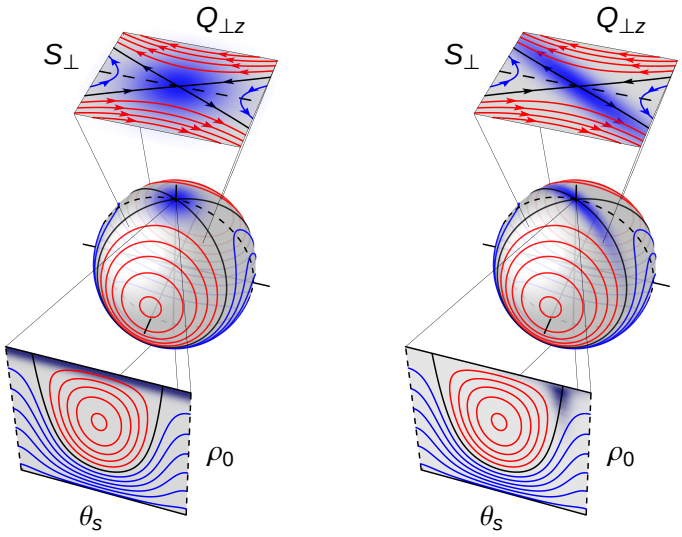

Figure 7.1: Different representations of the relevant phase spaces. The different phase spaces are shown for the system. The center represents the spin-nematic phase space used extensively in Refs. [38, 58]. The top represents the polar projection of the Bloch sphere spin-nematic phase space. The hyperbolic fixed point is clearly visible in both phase spaces. The bottom of the illustration shows the familiar $\rho_0 - \theta_s$ phase space as a mercator projection of one of the hemispheres of the spin-nematic Bloch sphere. The left side shows the system at $t = 0$, where it has been initialized at the hyperbolic fixed point. The right side shows the system after some evolution. The distribution has been exaggerated for illustrative purposes.

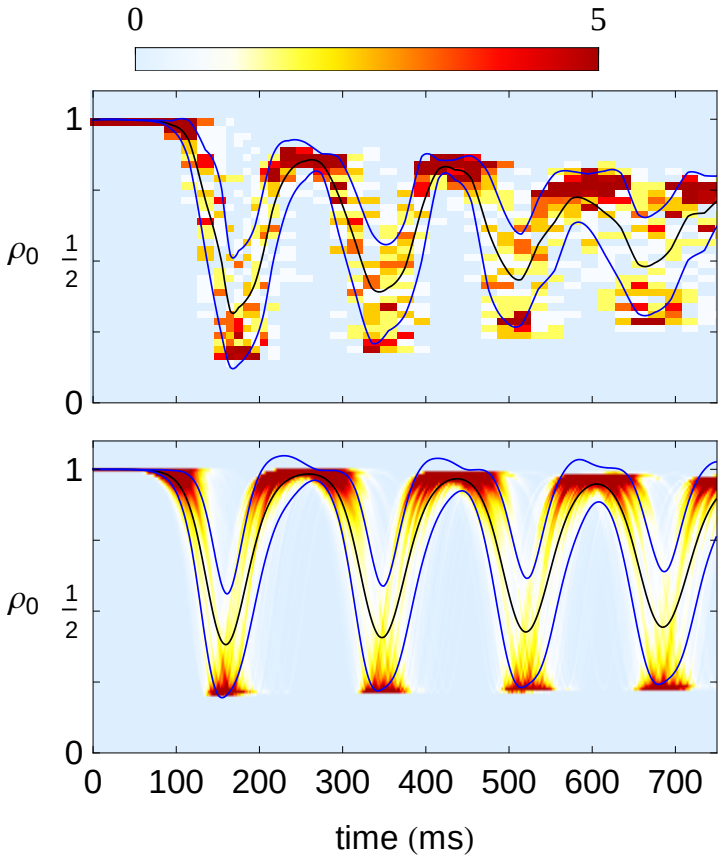

Figure 7.2: Measured evolution of the probability density of ρ_0. The measured evolution of the probability density of ρ_0 is shown (top). The black line represents the mean value of ρ_0 and the blue lines represent $\pm\sigma$, the standard deviation. The theoretical evolution is shown in the bottom plot.

data points, the system was initialized in the $m_f = 0$ state and allowed to freely evolve for different time intervals. At the end of the evolution time, the condensate was released and allowed to expand in a Stern-Gerlach field, separating the different m_f components for imaging. After 22 ms of free-fall, the condensate was imaged using fluorescence imaging for 400 μs and the different components counted. At each evolution, at least 50 samples were taken to allow the data to be binned. At several times, large sample sizes (≥ 900) were collected to produce very detailed histograms of the distribution.

Several observations can be immediately made in looking at Fig. 7.2. First, there is a long pause at the onset of evolution where the condensate does not appear to evolve, similar to the simple inverted pendulum. After 100 ms, the system begins oscillations, nearly reviving to $\rho_0 = 1$ at 250 ms. Without noticeable pause, the condensate then continues to oscillate with a regular period. The long pause, and general oscillatory nature of the data is matched by the simulation results of Fig. 3.5 to good estimate for the period. The subsequent oscillations of the data do exhibit more dampening than the simulation, but otherwise, the two appear to be in good agreement, especially for the first oscillation.

The second observation that can be made from Fig. 7.2 is that, just as was seen for the simple pendulum and in the dynamical simulations, for the majority of the evolution, the mean does not pass through the point of highest probability density. Instead, the measured values appear to be skewed from the mean. Additionally, at times, the data appears to be very sharply peaked around the maximum or minimum values at the turning points of the oscillation.

7.2 Origins of ρ_0 Probability Distributions

When looking to understand the reason for the distributions that arise from the system evolution, it is convenient to look at the $\rho_0 - \theta_s$ mean-field phase space.

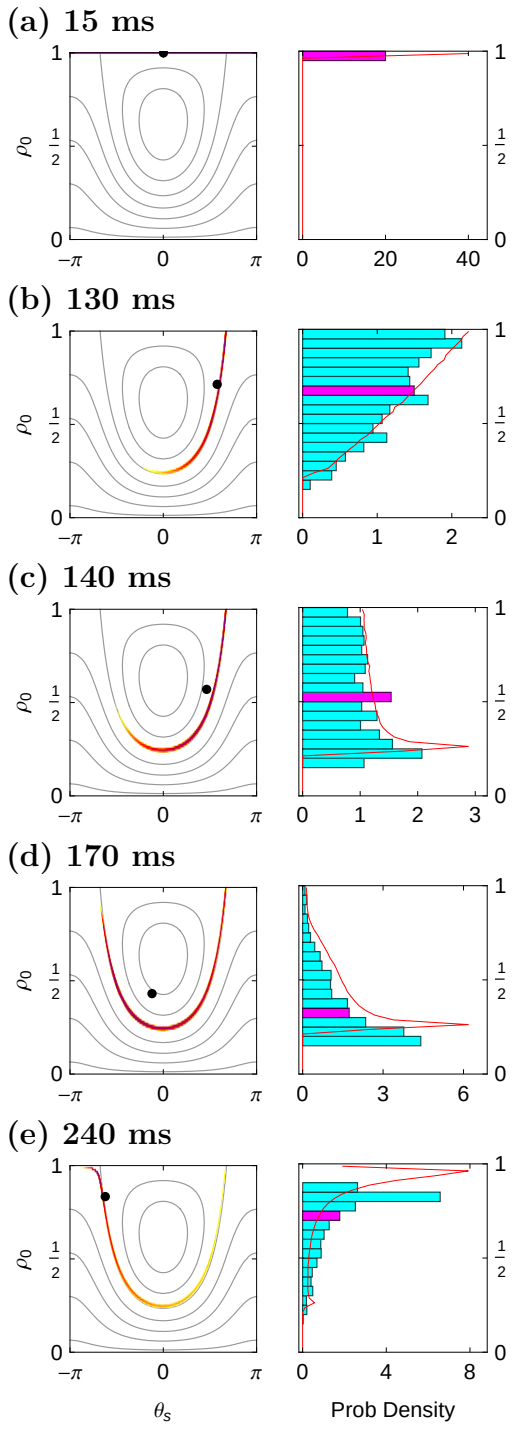

Figure 7.3: Phase space and ρ_0 distributions. The evolution of the system is shown on the $\rho_0 - \theta_s$ phase space (left) for various evolution times. The black dot represents the mean value of (ρ_0, θ_s). The right column shows a histogram of the ρ_0 values for the given evolution time. The bars are the binned data points from over 900 experimental observations per evolution time, and the purple bar represents the bin containing the mean value of ρ_0. The red line is the histogram from the simulation.

Fig. 7.3 (Left) shows the mean-field phase space for several different evolution times. On each of the energy contours the probability density of the simulated system at that time is shown, as well as the location of the mean value of ρ_0 and θ_s (black dot). Shown next to each phase space diagram is the measured histograms for the data (bars) and the simulation (red line). The purple bar in each histogram represents the bin containing the mean of ρ_0 for that time step.

When examining the energy contours and the probability densities, one can see that at $t = 15$ ms, the system is primarily distributed along the $\rho_0 = 1$ point, and consequently the histogram for ρ_0 is binned there, as well. As the system converges to the separatrix and begins to evolve along it, the probability density of the system starts to dip lower into the ρ_0 values. This is mirrored in the histograms which gradually shift probability density from $\rho_0 = 1$ to lower values. This trend continues until the system reaches the lowest point in the phase space that it can travel at around 170 ms. The shape of the phase space is such that the system is distributed along a relatively wide range of θ_s and a wide range of ρ_0, but most of the system is at the bottom. The result is that the histogram shows a skew below the the mean with a sharp peak. The system then returns to the top where it again distributes itself over a relatively wide range of θ_s for a small range of ρ_0, resulting in the same relative shape as at the bottom of the phase space, only skewed in the opposite direction.

7.3 Higher-Order Analysis of ρ_0 Distributions

When attempting to characterize a statistical distribution, the most common attributes used in the description are the mean and the standard deviation. For a Gaussian distribution, the mean and standard deviation are all that is needed to characterize the shape. However, throughout the evolution of ρ_0, the distribution takes on highly non-Gaussian shapes. At times, the maximum probability density is skewed to the right of the mean, and others it is skewed to the left. Additionally,

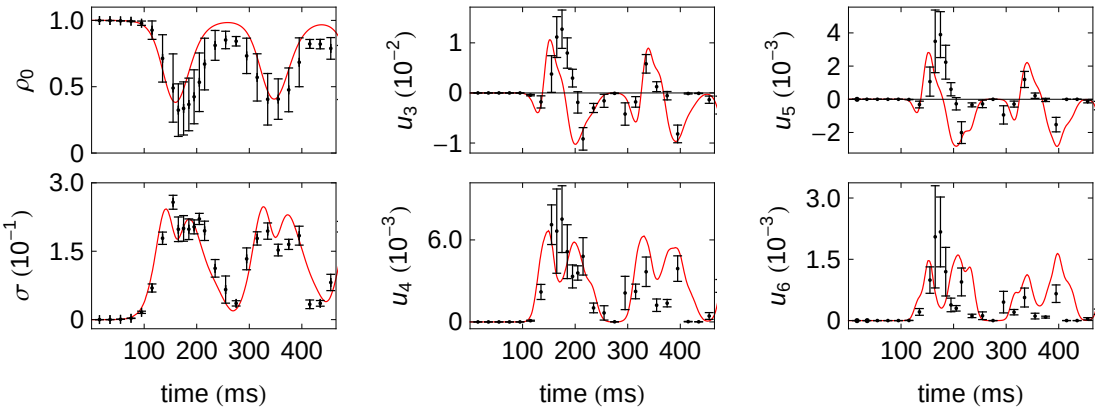

Figure 7.4: Central moments for spin mixing evolution. The first through sixth central moments are shown for the evolution of ρ_0. The top row has the odd moments, the bottom row has the even moments. The error bars for the data were calculated using a common bootstrap algorithm.

there are times where the data is sharply peaked at a value, and at others it is not. For these reasons, it is clear that the mean and standard deviation alone are not sufficient in characterizing the distribution.

7.3.1 Central Moments

The mean and the standard deviation are just the first two of a series of quantities that describe the nature of a distribution. The mean, or first moment[1], describes the center point of the distribution, while the standard deviation, or second moment[2], describes the width of the distribution.

The third moment is the skewness, which indicates the asymmetry of the distribution. A positive skew has the area of highest probability density to the left of the mean, while a negative skew has the area of highest probability density to the right of the mean. For a normal distribution, the skew is zero.

[1]Use of the term "nth-moment" in this chapter will be used to mean both the nth central moment and the nth standardized moment. The definitions for each are: nth-central moment- $u_n = \langle(\rho - \bar{\rho})^n\rangle$. nth-standardized moment=$\frac{u_n}{\sigma^n}$ For the purposes of this section, it is not important which is used.

[2]The second moment is actually the variance, σ^2, however, it is more intuitive to discuss the standard deviation because its units are the same as those of the mean.

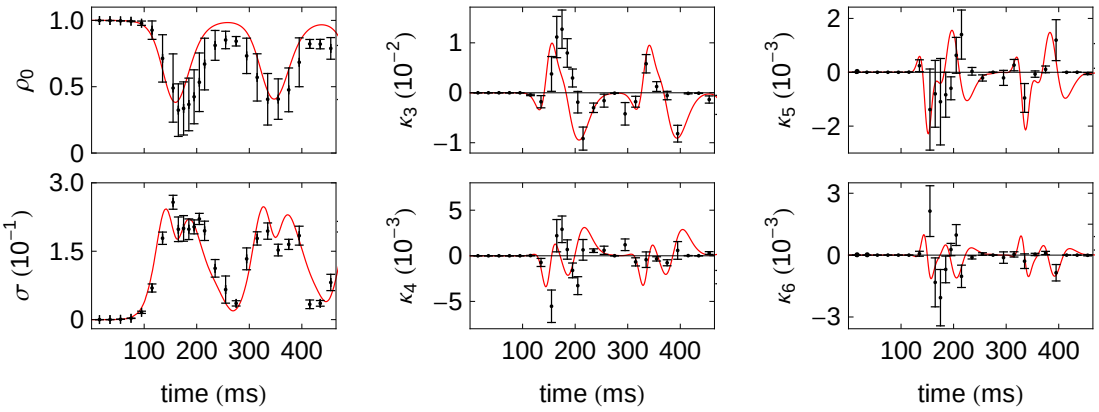

Figure 7.5: Data cumulants for spin mixing evolution. The first through sixth cumulants are shown for the evolution of ρ_0. The top row has the odd cumulants, the bottom row has the even cumulants. The error bars for the data were calculated using a common bootstrap algorithm.

The fourth moment is the kurtosis. The kurtosis measures the pointedness of a distribution. The kurtosis for a normal distribution is three, which makes it more convenient to look at the kurtosis excess which subtracts three from the kurtosis so that a normal distribution has a kurtosis excess of zero. The more pointed a distribution, the higher its kurtosis excess, while the flatter a distribution is the smaller its kurtosis excess.

Higher-order central moments have no physical significance, but structure in the higher order moments indicates strong trends in the data at lower moments. The results of the measured central moments of ρ_0 are shown in Fig. 7.4.

7.3.2 Cumulants

A drawback of central moments is that they are not independent of each other. As a result, it is often preferred to use cumulants instead of central moments. Though the first three cumulants are the same as the first three central moments, the fourth and higher cumulants correct for the contributions of lower central moments in their calculation by subtracting them out. However, the physical interpretation of the fourth cumulant, for example, still applies.

There is no closed form for the nth cumulant (κ_n) as there is for u_n, instead, they must be derived from a generating function. Most mathematics software have a built in function for their calculation, which is what was used for the results in Fig. 7.5. Additionally, deriving a closed form for the standard error of the cumulants is a non-trivial task. Standard error prorogation techniques [119] are impractical. Instead, a technique called bootstrapping, while imperfect [120, 121], was used to calculate the error bars.

Fig. 7.5 shows the evolution of the first six cumulants. The mean is shown with the standard deviation for its error bars, while the remaining cumulants error bars are calculated as described in the previous paragraph. All of the cumulants show good quantitative agreement with the simulation results, especially the first, second, and third cumulants. For the fourth through sixth cumulants, the general trend of the data matches the simulation, but the timing and amplitude begin to differ slightly.

The standard deviation clearly shows the first dip in ρ_0 where the standard deviation reaches a maximum, and then the first revival where the system returns to the mostly $\rho_0 = 1$ state. The system then repeats the process for subsequent oscillations. The first dip and subsequent revival is also clearly visible in the third cumulant, which indicates the asymmetry of the distribution. As the system bottoms out in the phase space, the distribution is positively skewed, then the skew quickly changes direction at the first revival. This pattern repeats for subsequent oscillations.

The fourth cumulant shows the pointedness of the turning points quite clearly, as one would expect from looking at Fig. 7.3. The fifth and sixth cumulants also show structure in the data that closely matches the simulation.

7.4 Long Term Evolution

The long-term evolution of the system is shown in Fig. 7.6. The also show a fairly consistent frequency of oscillations, though the oscillations break down after ~ 1.5 s.

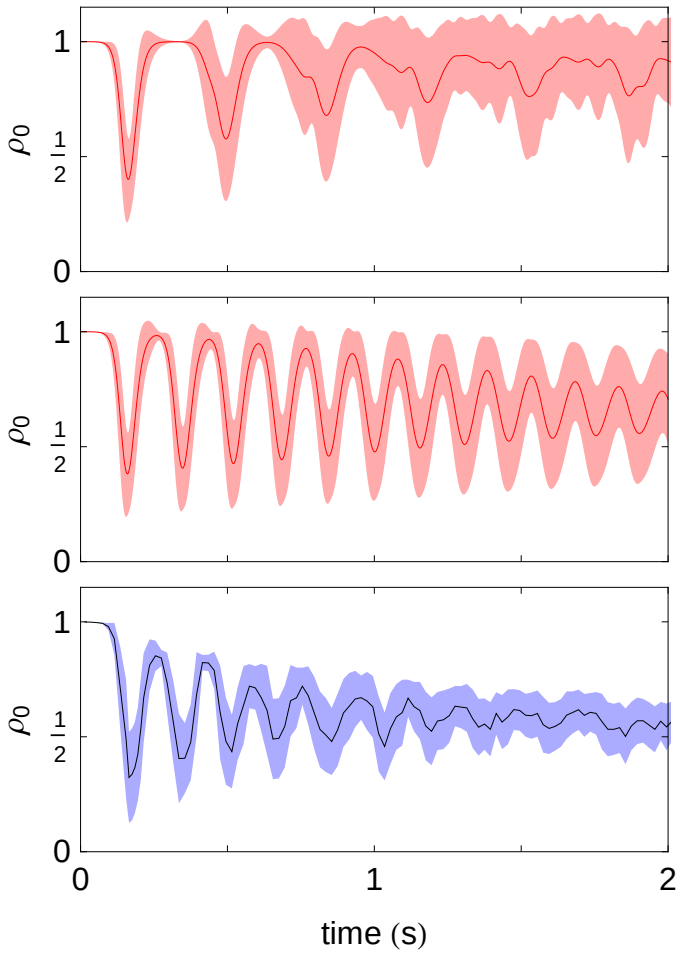

Figure 7.6: Long-term evolution of ρ_0. The top plot shows the quantum simulation without loss, while the middle plot shows the quantum simulation incorporating atomic loss. The bottom plot is the measured evolution of ρ_0. The solid line is the mean, the shaded region is $\pm\sigma$.

This is close to the trap lifetime of $\tau_B = 1.8$ s. Also, the standard deviation of ρ_0 remains fairly constant. When compared to the long-term evolution of the dynamical simulations in Fig. 3.4, the oscillatory nature of the measured ρ_0 more closely resembles that of the simulation with the loss model. However, the experimental results show significantly greater dampening than the simulation results. This would indicate that the chosen model is incomplete, but serves as an acceptable first-order correction to account for loss. The possibility exists that the loss model is wrong, however, so further study of incorporating loss should be considered for future work.

7.5 Impurity Analysis

Some of the dynamics observed in the experiment could be described by impurities in the initial state of the system. In this section, the effects of spin impurities in the initial state preparation are discussed, and the impurity limits determined by the experiment. The experiment uses condensates containing 4×10^4 atoms, initialized in the $f = 1, m_f = 0$ hyperfine state with measured impurities in the $m_f = \pm 1$ states (limited by the atom counting noise [38]) below < 30 atoms or 0.1% of the total population.

Spin evolution from the metastable state is a parametric amplification process whose early-time dynamics are logarithmically sensitive to initial population in the $m_F = \pm 1$ states [55]. Hence, any impurities in the initial state preparation will certainly effect the timescale of the initial pause and first oscillation minimum. Importantly though, as shown in [122], the overall character of the evolution, including the intricate evolution of the quantum spin fluctuations, is robust to impurities even up to the few percent level, which is an order of magnitude larger than our measured bound. In order to analyze the quantitative effect of impurities, we perform simulations with two types of impurities: an initial non-zero magnetization and an initial non-zero number of pairs of $m_f = \pm 1$ atoms. The results of these calculations are

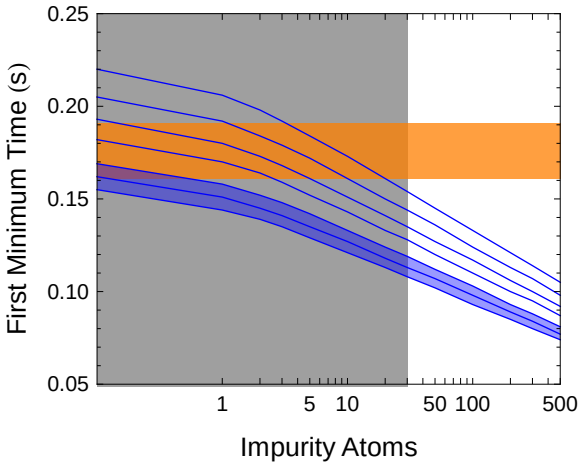

Figure 7.7: Analysis of Impurities. Upper bound from direct measure of impurities at 15 ms of evolution, gray shaded region. Measurement of first minimum of ρ_0, orange shaded area. Simulation with polluting atoms for a spinor dynamical rate of $|c|/(2\pi\hbar) = 5.0$, 5.5, 6.0, 6.5, 7.0, 7.5, and 8.0 Hz (blue lines top to bottom). The values between 7-8 Hz are most consistent with the long term dynamics and are shaded blue.

nearly identical for the same number of impurity atoms with the non-zero magnetization results shown in Fig. 7.7 for various levels of impurities and for a range of spinor dynamical rates determined from the long time evolution of the experiment (blue shaded region) as well as several other values (blue lines). These are compared to experimental measurements in order to ascertain an upper bound on the impurities in the experiment.

The first time at which the atom populations are measured is 15 ms after the beginning of the magnetic quench, which provides an upper bound on the impurities present at $t = 0$. The population in the $m_F = \pm 1$ states at this time is < 30 atoms, which is shown as the gray shaded region in Fig. 7.7. Also plotted in Fig. 7.7 is the measured time that the $m_f = 0$ population reaches a minimum value. This time is logarithmically sensitive to impurity atoms and, for both magnetization and pair impurities, reduces similarly for the same number of impurity atoms. The experimental measurement of this time plus and minus one standard deviation is shown as

the orange shaded region. The shaded regions overlap only in the limit of very little pollution of the initial state.

The overlap region is consistent with no pollution and is inconsistent with pollution of the magnetization of greater than 5-10 atoms and pair pollution of greater than 3-5 pairs of ± 1 atoms, even for significantly different spinor dynamical rates than the evolution suggests. While it is conceivable to trade off between measured values of the spinor dynamical rate and pollution, the dynamics of the quadrature squeezing measurement reported previously [38] indicates that the value of spinor dynamical rate estimated from the long term population dynamics is more consistent with the available data. The analysis presented here along with the non-Gaussian nature of the fluctuations and the squeezing dynamics reported previously make an effective argument for the initial state preparation producing a very pure $m_f = 0$ state.

7.6 Concluding Remarks

This chapter described the major experimental results of this thesis. It showed the summary of over 10,000 data points to demonstrate the non-Gaussian evolution of the spin-1 Bose condensate. The large numbers of samples were used to gain reliable statistics of the results. These results included the traditionally measured mean and standard deviation of ρ_0, but went further in the analysis by including the third through sixth central moments and cumulants. Additionally, very large samples were taken for various time points and detailed histograms of the distributions were shown to be in very good agreement with simulations.

The inclusion of a loss model allowed for comparison with simulations for longer evolution times than previously reported, and showed reasonable match in the higher order moments. Furthermore, the effect of impurities in the initial state was shown to be an unlikely cause of the dynamics. In general, this chapter demonstrates that the loss model used is a reasonable first order correction to the dynamical equations

of Chapter 2.

CHAPTER 8

IMPLICATIONS OF THE LOSS MODEL

The addition of a loss model in Chapter 3 greatly improved the quantitative agreement between the data and the simulation. The data-simulation agreement prior to the loss model was good for ~ 250 ms, but quickly diverged from there, with the simulation remaining in the $\rho_0 \sim 1$ area for an extended pause while the data showed no pause before continuing oscillations. The loss model eliminated the long pause at the top of the first revival in the simulation, and also demonstrated the same oscillatory pattern as the data. The loss model employed two different techniques, both of which captured the dynamics of the system fairly well. This chapter will explore the implications of the loss model. Specifically, what happens to the phase space of the system if the spinor dynamical rate changes as atoms are lost, and what impact does that have on the long-term evolution of the system.

8.1 Changing of the Phase Space

8.1.1 Simulation Results- No Loss

The dynamical simulations without the loss model show a pause at the first revival, then the system quickly takes on a multi-frequency oscillation pattern with increased standard deviation (See Fig. 7.6). The primary cause of this pattern is the dispersion of the system near the separatrix due to the diverging periods of orbits. After a short period of time, and intermittently thereafter, the system is almost completely dispersed in a ring round the separatrix See Fig. 8.1, (b), (d), and (f)). At other times the mean of ρ_0 shows small oscillations as the different trajectories revive at near simultaneous times, similar to beat notes (See Fig. 8.1, (a), (c), and (e)). The result of the diverging orbital periods and consequential dispersion make for a complicated

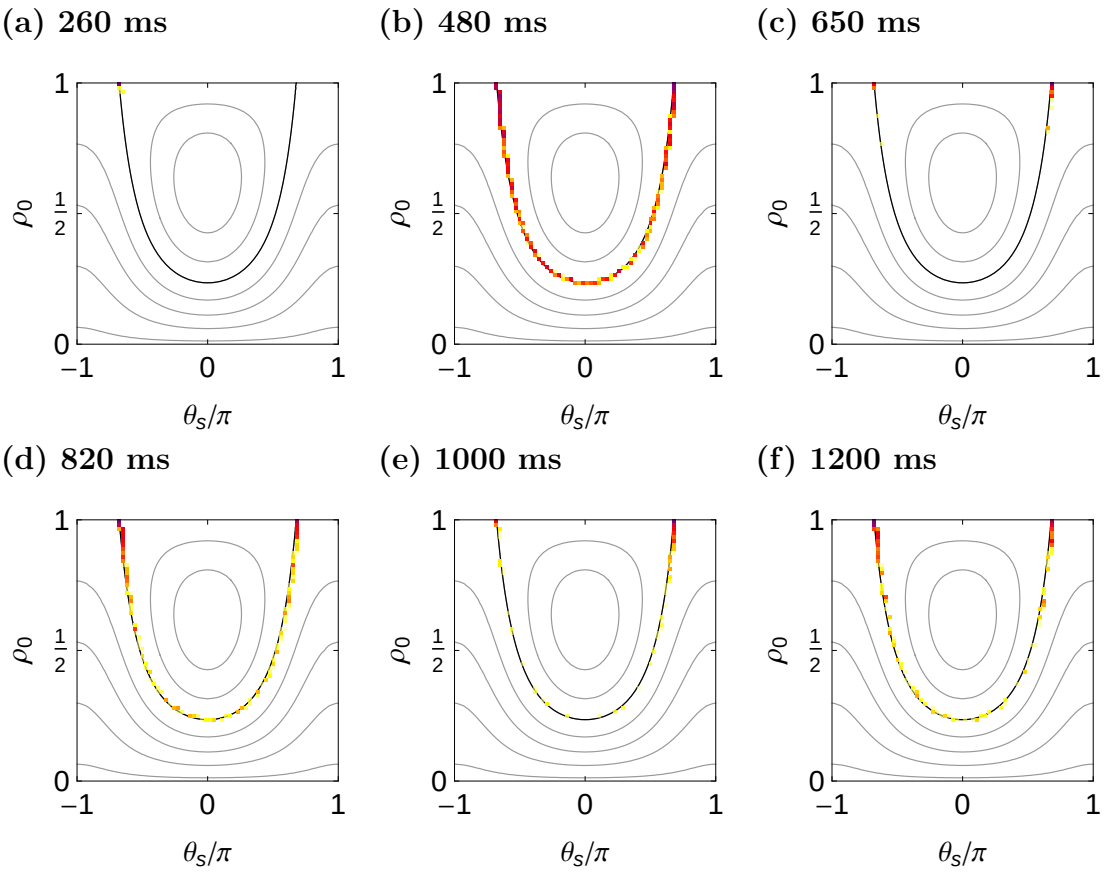

Figure 8.1: System evolution without loss. The evolution of the probability density of ρ_0 is displayed on the mean-field phase space for several different times.

oscillatory pattern for ρ_0.

8.1.2 Simulation Results- With Loss

The dynamical simulations that incorporate the loss model do not show the pause at the first revival, nor do they show multi-frequency oscillations. Instead, ρ_0 oscillates in an apparently coherent fashion with a regular period and slight dampening (See Fig. 7.6). This pattern is consistent with the data and other comparisons between the data and simulations indicate that the loss model is, at least to first order, valid. The question then is what does the probability of ρ_0 look at different times on the mean-field phase space? Fig. 8.2 shows the system evolution at two times that illustrate the key difference between the models. The first time is near the first revival, ∼220

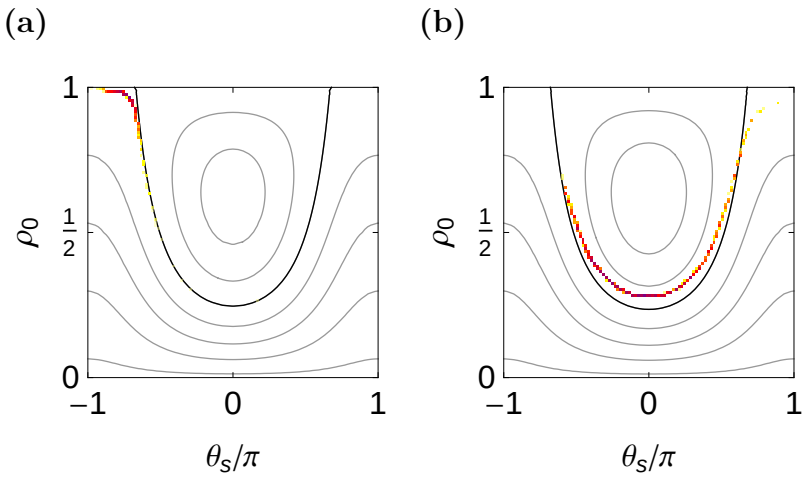

Figure 8.2: System evolution with loss on fixed phase space. The evolution of the probability density of ρ_0 is displayed on the mean-field phase space at two illustrative times. The value of the spinor dynamical rate for the simulation is changed as the atoms are lost, but the phase space remains constant. **(a)** shows the system at the first revival, $t \sim 260ms$. **(b)** shows the system at a later time, ∼1150 ms.

ms. In the loss-less model, the probability distribution of ρ_0 returns to the top of the phase space where it "turns" both left and right, dispersing itself across the entire range of θ_s, thus occupying phase winding orbits (left turn) and closed orbits (right turn). On the other hand, in the model with loss, it is clear that the probability distribution of ρ_0 only "turns" left, away from the separatrix, and into phase-winding trajectories instead of trajectories that span both winding and closed orbits as in the loss-less case. The second time is at a later time in the simulation, ∼1150 ms, when the system is roughly centered at the bottom of its orbit in the phase space. This time was chosen because it illustrates that the trajectories of the system cross the separatrix in what appears to be an unexpected way. In fact, the evolution of ρ_0 does not appear to be following the contour lines of the phase space at all. The simulation uses the time-varying spinor dynamical rate which changes as $N^{2/5}$. However, the mean-field phase space is also a function of the spinor dynamical rate, so the shape of the phase space will also evolve. The following discussion is based on the assumption that the loss model is correct, with the caveat that it may be incorrect. Previous

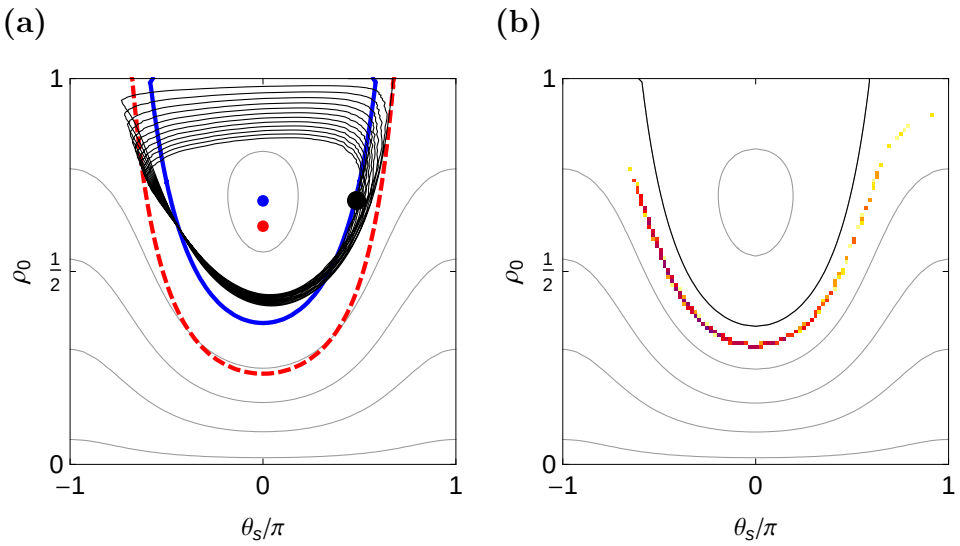

Figure 8.3: Ensemble evolution compared with $\bar{\rho}_0$ evolution. **(a)** shows the evolution of $\bar{\rho}_0$. The red dashed line and the red dot are the separatrix and ground state at $t = 0$, respectively. The blue line and the blue dot are the separatrix and ground state at $t = 2$ s. **(b)** The evolution of the probability density of ρ_0 is shown at $t = 2$ s.

experiments that showed the evolution of ρ_0 on the mean-field phase space [34, 36], demonstrating what looked like ρ_0 spiraling to the ground state on the phase space drawn for $t = 0$. However, due to loss, the phase space at later times is not the same. The separatrix has moved up in the phase space, as has the ground state. The probability distribution of ρ_0 is undergoing phase winding orbits outside of the moving separatrix, while the mean of ρ_0 appears to spiral into the fixed phase-space ground state. This is illustrated in Fig. 8.3. The black line in Fig. 8.3 **(a)** shows the evolution of $\bar{\rho}_0$ for 2 s. The red dashed line and the red dot are the separatrix and the ground state of the system at $t = 0$, while the blue line and the blue dot are the separatrix and the ground state at $t = 2$ s. Notice how the evolution of $\bar{\rho}_0$ appears to spiral toward the initial ground state, while the separatrix and the ground state move upwards in the phase space. Fig. 8.3 **(b)** instead shows the probability density of ρ_0 at $t = 2$ s. It is clear that the system is in a close group of phase-winding trajectories outside the separatrix.

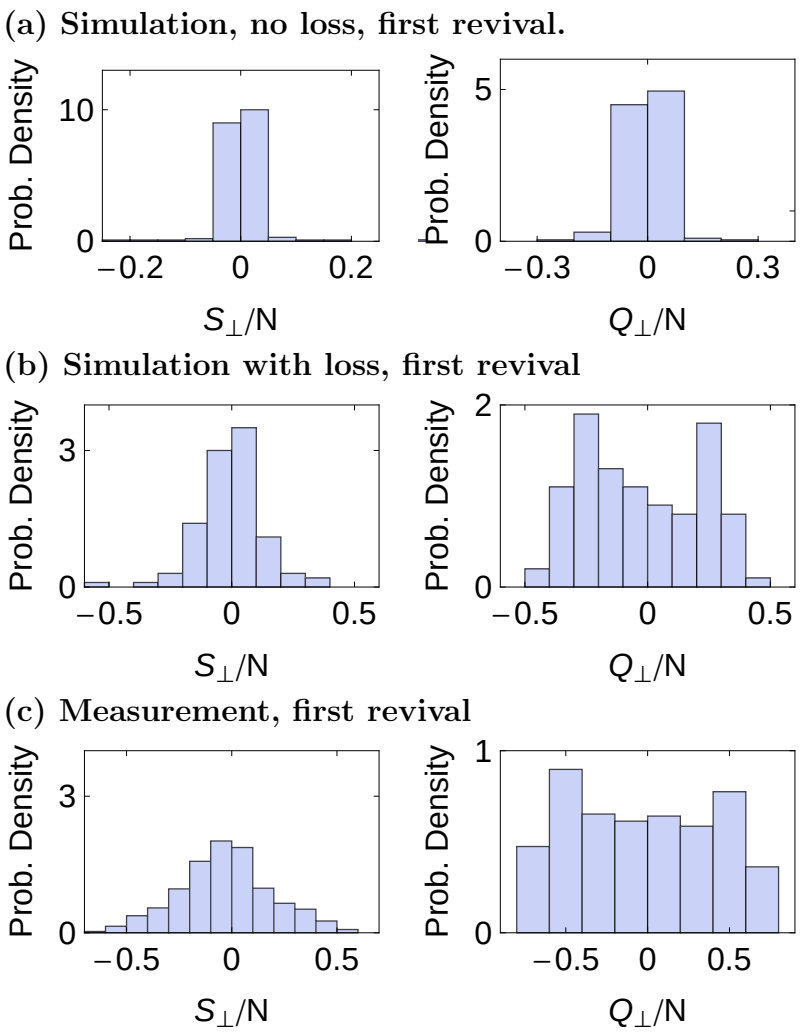

Figure 8.4: Histograms of $\mathbf{S}_\perp$ and $\mathbf{Q}_\perp$. The histogram for $S_\perp$ and $Q_\perp$ for the loss-less simulation, the simulation incorporating loss, and the data at the first revival of the evolution.

8.2 Measurement of $S_\perp$-$Q_\perp$

As was shown in the simulation, the changing of the phase space due to a changing spinor dynamical rate causes the system evolution to take a completely different track than the loss-less case. Instead of the system undergoing a combination of phase-winding and closed orbits, the separatrix shifts upwards and the ensembles all become phase-winding. The distributions of $S_\perp$ and $Q_\perp$ at the first revival for the simulation and the measurements are shown in Fig. 8.4. The top set of histograms shows what the distribution of $S_\perp$ and $Q_\perp$ look like for the loss-less simulation, while the middle set of histograms shows the distribution of $S_\perp$ and $Q_\perp$ for the simulation with loss. The loss-less histograms show a Gaussian-like distribution for both $S_\perp$ and $Q_\perp$. The histograms for the loss-included simulation show a Gaussian-like distribution for $S_\perp$, while $Q_\perp$ is bimodal, a possible consequence of the system evolving outside of the separatrix as previously discussed. The bottom set of histograms are measured in the experiment. The $Q_\perp$ histogram shows a bimodal shape, similar to the simulation incorporating loss.

A reconstruction of the phase space distributions can be performed to verify the evolution of the system. In order to reconstruct the phase space distribution, an inverse Radon transformation (similar to tomographic systems in the medical field, Ref. [123].) is performed on the histograms from the simulations and the data at eight different quadrature angles. In terms of the $S_\perp$-$Q_{\perp z}$ phase space, with out loss, the system starts as a Gaussian distribution and returns to a roughly Gaussian distribution at the first revival. (Fig. 8.5 **(a)**). However, when the effects of loss are included, the distribution more closely resembles a bow-tie with the majority of the distribution aligned along the $S_\perp$ axis (Fig. 8.5 **(b)**).

Reconstruction of the phase space at the first revival from experimental results shows that the phase space does in fact resemble a bow-tie as the simulation predicts (Fig. 8.5 **(c)**). The first revival is chosen as the best time to study the system because

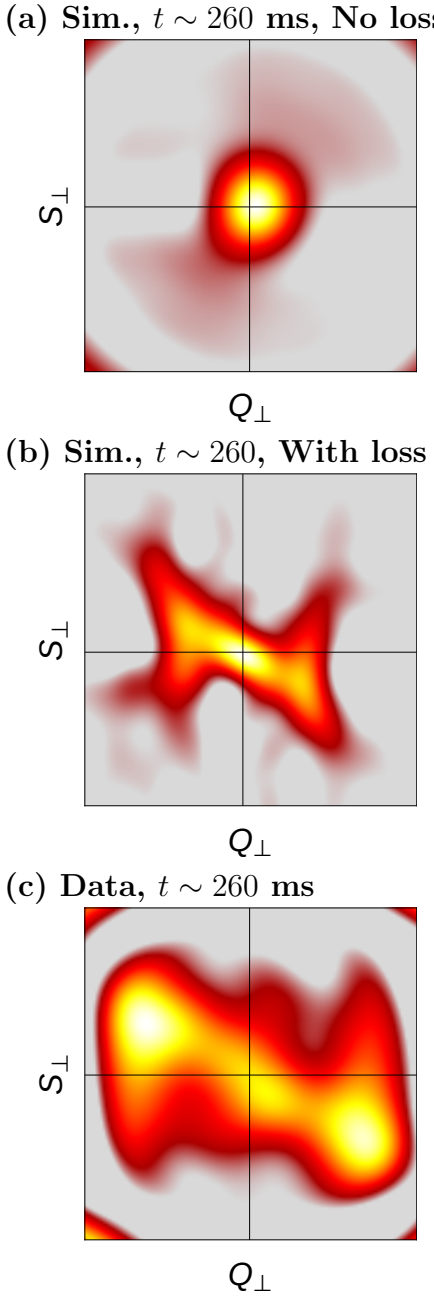

Figure 8.5: Reconstruction of the $S_\perp$-$Q_{\perp z}$ phase space. **(a)** shows the reconstruction of the phase space for the loss-less simulation results for the first revival. **(b)** shows the reconstructed phase space for the simulation with the loss model at the first revival. **(c)** shows the reconstructed phase space for the experimental results at the first revival.

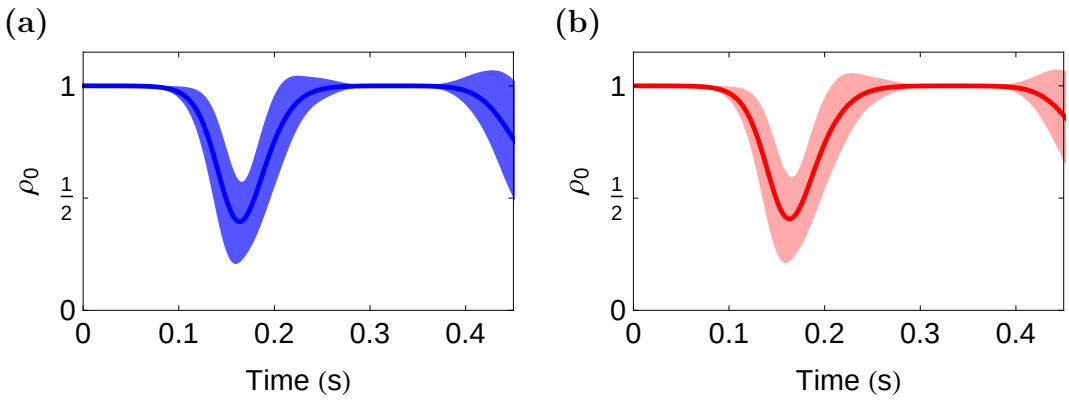

Figure 8.6: Evolution of ρ_0 with changing magnetic field. **(a)** shows the simulated evolution of ρ_0 without atomic loss. **(b)** shows the simulated evolution of ρ_0 with atomic loss and a decreasing magnetic field.

it is the earliest time in the experiment when we can clearly see the effect we want, yet not too far in the evolution of the system that other known issues with the simulation are dominant (e.g. dampening discrepancies).

8.3 Future Experimental Measurements

An interesting topic of exploration proposed in previous works has been the measurement of the dispersion of the system. However, with the atomic loss causing the phase space to change, the dispersion effects may be difficult to isolate. An alternative would be to compensate for the atomic loss by changing the magnetic field. By decreasing the magnetic field at the appropriate rate, the phase space would remain unchanged, and evolution of the system should follow fixed contour lines. Fig. 8.6 shows dynamical simulations for the evolution of ρ_0, **(a)** shows the simulation without loss, and **(b)** shows the simulation with loss and a decreasing magnetic field. The two plots are very similar, providing at least conceptual proof of principal. The next step would be to modify the control sequence to scale the magnetic field and measure the evolution of ρ_0, looking for the long pause after the first revival.

8.4 Concluding Remarks

The loss model used for the dynamical simulations captures a good amount of the dynamics of the system. The oscillatory nature of the evolution of ρ_0 is captured by the model, and is explained by the upwards motion of the separatrix in the phase space changes the trajectories from equal sets of diverging phase winding and closed orbits to a collection of close phase-winding orbits. Reconstruction of the phase space from experimental data confirms that the evolution of the system is indeed outside of the separatrix, indicating an upward movement of the separatrix as a result of the atomic loss.

Despite the improved agreement between the data and simulation that the loss model provides, there is still exists unaccounted for differences between the evolution of each. The most noteworthy is the difference in dampening rates. While the simulations show some dampening, the data shows dampening at a greater rate. Initial thoughts on the cause of the dampening could be that, as atoms are lost, the single mode approximation used in Section 2.2 may be invalidated. This would lead to a complicated interplay of the internal and external dynamics that ultimately transfers the internal spin energy into spatial domain structures [63]. However, quick dimensional analysis shows that the condensate radius scales as $N^{1/5}$, while the spin healing length, ξ_s, scales as $N^{-1/5}$. Any dampening from atomic loss is not, at first glance, related to the violation of the SMA, since the loss of atoms makes the SMA more valid. However, internal spin energy may be transferred to other areas, such as rethermalization after atoms are lost such that the internal spin energy decreases with time. The effects of possible internal spin energy transference would need more analysis and possible inclusion into the dynamical equations.

CHAPTER 9

CONCLUSION

The principal contribution of this thesis is the detailed study of the non-Gaussian evolution of a spin-1 BEC in the regime of a quantum inverted pendulum. Detailed measurements of the distribution of the evolution are taken for times far in excess of any previously conducted. Furthermore, higher-order moment and cumulant analysis was conducted to demonstrate the non-Gaussian nature of the evolution.

This thesis also provided a mapping of the phase space through the use of coherent oscillations. The oscillations were fit to the analytical solution to the mean-field dynamical equations and the general shape of the phase space shape was extracted.

Despite the obvious shortcomings of the loss model, it was helpful in capturing some of the dynamics of the system caused by loss. As a result of the partial success of the loss model, some implications as to the effect of atomic loss on the model came to light. These implications were studied, including a reconstruction of the phase space.

9.1 Spinor Theory and Dynamical Simulations

The spinor theory used in this thesis is the same as used to analyze the most recent experiments. The quantum theory was largely a review of the literature, with the noted exception that the effect of the quadratic Zeeman energy was added. The addition quadratic Zeeman energy was a critical step in the implementation of the quantum model. The mean-field theory used in this thesis was also largely a review of the literature, using the quasi-probability distribution to capture the quantum fluctuations needed for evolution of the other-wise stationary $m_f = 0$ initial conditions in the semi-classical model. The two methods provided simulations that were within

0.5% of each other for population dynamics.

The addition of a loss model to the mean-field and quantum simulations moderately increased the evolution time for which the data and the simulation had reasonable quantitative agreement. Not only did the oscillatory nature of the evolution of ρ_0 match the data more accurately, but the agreement was seen in the higher order cumulants. Previously, experimental results showed only limited quantitative agreement, limited to the low depletion, perturbative limit at very early times. This agreement was extended for the mean and standard deviation to ~ 240 ms, however the simulation and data diverged greatly from there. The addition of the loss model extended the reasonable quantitative agreement to ~ 450 ms, and qualitatively they agreed well past the trap lifetime.

The convenience of relying on both the quantum theory and the mean-field theory for comparison with the data results opened up new avenues of exploration, and greater conceptual understanding of the results. Many of the results were analyzed with simulations from each theory. The best example of this is the measured histograms of ρ_0 being compared to the coefficients of the Fock states, pictured along side the mean-field phase space results for spin-mixing evolution from the $m_f = 0$ initial state. The effects of dispersion were clearly visible in the mean-field phase space, while the dynamics of the Fock states was clear in the histograms.

The mean-field theory shows that the system resembles a non-rigid, momentum-shortened pendulum. The simple pendulum was studied in Chapter 4, which provided insight used to study the BEC system. The results of Chapter 6 and 7 verify the analogy to the simple pendulum. Future experimental work should look to extend the pendulum analogy and find ways to stabilize the system in the "inverted pendulum" position. This can be shown in two key ways, the first being a lack of evolution in ρ_0. The second way to show stabilization would be to measure the variance of $S_\perp$, which should increase as the system evolves, then decrease after a spinor phase shift

rotates the quadrature angle such that the system is on the converging manifold of the separatrix.

Despite the improved agreement between the data and simulation that the loss model provides, there is still exists unaccounted for differences between the evolution of each. The most noteworthy is the difference in dampening rates. While the simulations show some dampening, the data shows dampening at a greater rate. Future work will focus on improving the loss model to account for this.

9.2 Non-Gaussian Evolution and Mapping the Phase Space

The non-Gaussian evolution and phase space mapping chapters served as an in-depth validation of the expanded theoretical model. The evolution of ρ_0 could not be adequately characterized by the mean and standard deviation, as for most of the evolution the mean is not located in the area of highest probability density. Additionally, with the inclusion of the loss model it was necessary to extend the evolution times to well beyond those measured before. A common method used to characterize the shape of a distribution is to calculate the cumulants of the distribution. While the first three cumulants can be directly translated into a physical understanding of the distribution's shape, the higher order cumulants indicate additional structure to the data. The measurements showed evolution in the first six cumulants, demonstrating that the system was evolving in a non-Gaussian manner.

When mapping the phase space, the system was initialized to specific start points in the mean-field phase space and allowed to evolve. The subsequent parametric plots of ρ_0 allowed for a detailed reconstruction of the phase space using the techniques gleaned from analysis of the simple pendulum. Moreover, the results further validated the simulation's ability to take a pure $m_f = 0$ system, conduct an RF rotation with spinor phase shift, and produce subsequent evolution that accurately models the experiment.

Future work in this area would increase the number of surveys of the phase space conducted in Chapter 6. This would give a complete map of the phase space rather than just two cross-sections. Additionally, the surveys could be done at a later time, after several orbits have transpired. This would allow for observation of any changes in the shape of the phase space as a result of atomic loss.

9.3 Implications of the Loss Model

The loss model used to improve the dynamical simulations, at least to first order, provides an increased accuracy in the matching of data with simulation. Naturally, the changing of the spinor dynamical rate in the mean-field picture has the implication that the shape of the phase space would change as well. Though the system evolves by following the appropriate energy contour, the evolution would be affected by the changing energy contours. The initial state of $m_f = 0$ would see the biggest affect from the change, since it initially closely spans both sides of the separatrix equally. If the separatrix moves upwards in the phase space, the initial state would rather rapidity find itself outside of the separatrix executing phase winding orbits as a whole, rather than a superposition of phase winding and closed orbit trajectories.

The best time in the evolution to determine if this is happening is at the first revival of ρ_0, where the loss affects are beginning to become important yet not as dominant as at later times. Using the reverse radon transformation, the $S_\perp - Q_{\perp z}$ phase space was reconstructed, showing that the majority of the system was in fact outside of the separatrix, providing evidence to support the physical validity of the loss model.

Future work in this area could include reconstruction of the phase space at different evolution times for different initial conditions that clearly demonstrate the nature of the changing phase space.

9.4 Problems, Improvements, and Future Improvements

It is no surprise to anyone who constructs an experimental apparatus that trade-offs are often made in the construction process. Often times, quick solutions meant to be a proof of principal instead turn into permanent solutions, or better ways to execute the experiment are found and implemented ad-hoc. Even more troublesome, components to the experiment go past their useable lifetime and need to be replaced. All of these can be found on the existing experiment, and some of them will be addressed here.

The large number of data points needed to construct the histograms of ρ_0 in Chapter 7 took several days to collect. This is a due to the fact that each experimental cycle takes $\sim$ 20 s, most of which is the long wait for the saturation of the MOT. Reduction in this time would allow for the same amount of data to be taken in less time, making the experimental results less sensitive to fluctuations in the conditions in the lab, where background magnetic fields can vary $\sim 10-20$ mG throughout the day. The use of a 2D MOT to form a cold atomic beam used to load the 3D MOT could reduce trap loading times from $\sim$ 15 s to $\sim$ 1 s. This also solves several other issues with the experiment. The use of a getter as a source in the experimental chamber would be eliminated, reducing background in the imaging system. Also, the ability to employ differential pumping between the 2D MOT and 3D MOT will increase trap lifetimes by an order of magnitude, conservatively. This in turn decreases the effect of loss on the system.

Another issue with the experiment is the use of magnetic windows on the vacuum chamber. The ferromagnetic materials (Kovar, an iron-nickel alloy) in the transition sleeve of the window causes a hysteresis problem and a semi-permanent magnetization of the chamber. There are work-arounds for both of these problems, but the best long-term solution is to replace the windows. We have purchased non-magnetic windows for all of the chambers on the octagon except the ZnSe windows, which do not have the hysteresis problem since they are constructed differently. These windows are AR

coated and waiting installation at the next chamber rebuild. A second option is to use an all-glass experimental chamber. This would completely eliminate the problems of hysteresis, but it would require new trapping techniques since the glass cell would be opaque to the CO_2 laser. The use of a Nd-YAG laser for trapping has been demonstrated, but it would have to be used in a cross-trap or lattice configuration.

Other problems include the accumulation of rubidium on the internal optics in the chamber. The ZnSe lenses are so contaminated that their surfaces glow from the heat of the CO_2 laser. These lenses will be replaced once they cause catastrophic problems in the experiment, at which time the windows in the chamber will be replaced.

Not all problems with the experiment are waiting to be repaired; several significant improvements have already been made. The control cables for all of the digital and analog channels used to pass over the light fixtures in the lab, possibly adding noise in the control voltages. These were all rerouted in appropriately installed cable trays throughout the lab. The insulated gate bipolar transistors (IBGTs) used to switch on the high current in the MOT coils were prone to failure as a result of the high inductance involved in switching $\sim$ 700 A in a sort period of time. The failure would destroy the IGBT along with its gate driver circuitry, resulting in a month of down time for repairs. The system was redesigned to include a large snubber capacitor circuit to mitigate the inductance problem. The system has yet to fail with the new design. Another change included the upgrading of all of the experimental computers to top of the line Windows 7 computers. For the most part, this was not too complicated. The exception was that the experimental control sequence in LabView was not compatible with Windows 7 and had to be re-designed. The switch allowed for some improvements and upgrades to the control sequence. Safety was also improved by the construction of new experimental table enclosures, including an aluminum casing for around the 100 W CO_2 laser. Lastly, the entire experimental cooling system was switched to a high-capacity chilled water system, resulting in

increased stability in the CO_2 system.

APPENDIX A

DIPOLE AND QUADRUPOLE OPERATORS

This appendix contains the tables of dipole and quadrupole operators used throughout the thesis for computations and derivations.

Table A.1: The spin-1 dipole operators. The expectation value of these operators are components of the angular momentum vector. The matrices are in a spherical polar basis $|f, m_f\rangle$.

$$S_x = \frac{1}{\sqrt{2}} \begin{pmatrix} 0 & 1 & 0 \\ 1 & 0 & 1 \\ 0 & 1 & 0 \end{pmatrix} \qquad \hat{S}_x = \frac{1}{\sqrt{2}} \left(\hat{a}_1^\dagger \hat{a}_0 + \hat{a}_0^\dagger \hat{a}_{-1} + \hat{a}_0^\dagger \hat{a}_1 + \hat{a}_{-1}^\dagger \hat{a}_0 \right)$$

$$S_y = \frac{i}{\sqrt{2}} \begin{pmatrix} 0 & -1 & 0 \\ 1 & 0 & -1 \\ 0 & 1 & 0 \end{pmatrix} \qquad \hat{S}_y = \frac{i}{\sqrt{2}} \left(-\hat{a}_1^\dagger \hat{a}_0 - \hat{a}_0^\dagger \hat{a}_{-1} + \hat{a}_0^\dagger \hat{a}_1 + \hat{a}_{-1}^\dagger \hat{a}_0 \right)$$

$$S_z = \begin{pmatrix} 1 & 0 & 0 \\ 0 & 0 & 0 \\ 0 & 0 & -1 \end{pmatrix} \qquad \hat{S}_z = \left(\hat{a}_1^\dagger \hat{a}_1 - \hat{a}_{-1}^\dagger \hat{a}_{-1} \right)$$

Table A.2: The spin-1 quadrupole operators. Expectation values of these operators are moments of the symmetric traceless quadrupole tensor. The matrices in spherical polar basis [58].

$$Q_{yz} = \frac{i}{\sqrt{2}} \begin{pmatrix} 0 & -1 & 0 \\ 1 & 0 & 1 \\ 0 & -1 & 0 \end{pmatrix} \qquad \hat{Q}_{yz} = \frac{i}{\sqrt{2}} \left(-\hat{a}_1^\dagger \hat{a}_0 + \hat{a}_0^\dagger \hat{a}_{-1} + \hat{a}_0^\dagger \hat{a}_1 - \hat{a}_{-1}^\dagger \hat{a}_0 \right)$$

$$Q_{xz} = \frac{1}{\sqrt{2}} \begin{pmatrix} 0 & 1 & 0 \\ 1 & 0 & -1 \\ 0 & -1 & 0 \end{pmatrix} \qquad \hat{Q}_{xz} = \frac{1}{\sqrt{2}} \left(\hat{a}_1^\dagger \hat{a}_0 - \hat{a}_0^\dagger \hat{a}_{-1} + \hat{a}_0^\dagger \hat{a}_1 - \hat{a}_{-1}^\dagger \hat{a}_0 \right)$$

$$Q_{xy} = i \begin{pmatrix} 0 & 0 & -1 \\ 0 & 0 & 0 \\ 1 & 0 & 0 \end{pmatrix} \qquad \hat{Q}_{xy} = i \left(-\hat{a}_1^\dagger \hat{a}_{-1} + \hat{a}_{-1}^\dagger \hat{a}_1 \right)$$

$$Q_{xx} = \begin{pmatrix} -\frac{1}{3} & 0 & 1 \\ 0 & \frac{2}{3} & 0 \\ 1 & 0 & -\frac{1}{3} \end{pmatrix} \qquad \hat{Q}_{xx} = -\frac{1}{3}\hat{a}_1^\dagger \hat{a}_1 + \frac{2}{3}\hat{a}_0^\dagger \hat{a}_0 - \frac{1}{3}\hat{a}_{-1}^\dagger \hat{a}_{-1} + \hat{a}_1^\dagger \hat{a}_{-1} + \hat{a}_{-1}^\dagger \hat{a}_1$$

$$Q_{yy} = \begin{pmatrix} -\frac{1}{3} & 0 & -1 \\ 0 & \frac{2}{3} & 0 \\ -1 & 0 & -\frac{1}{3} \end{pmatrix} \qquad \hat{Q}_{yy} = -\frac{1}{3}\hat{a}_1^\dagger \hat{a}_1 + \frac{2}{3}\hat{a}_0^\dagger \hat{a}_0 - \frac{1}{3}\hat{a}_{-1}^\dagger \hat{a}_{-1} - \hat{a}_1^\dagger \hat{a}_{-1} - \hat{a}_{-1}^\dagger \hat{a}_1$$

$$Q_{zz} = \begin{pmatrix} \frac{2}{3} & 0 & 0 \\ 0 & -\frac{4}{3} & 0 \\ 0 & 0 & \frac{2}{3} \end{pmatrix} \qquad \hat{Q}_{zz} = \frac{2}{3}\hat{a}_1^\dagger \hat{a}_1 - \frac{4}{3}\hat{a}_0^\dagger \hat{a}_0 + \frac{2}{3}\hat{a}_{-1}^\dagger \hat{a}_{-1}$$

$[\downarrow, \rightarrow]$	S_y	S_z	Q_{yz}	Q_{xz}	Q_{xy}	Q_{xx}	Q_{yy}	Q_{zz}
S_x	iS_z	$-iS_y$	$i(Q_{zz} - Q_{yy})$	$-iQ_{xy}$	iQ_{xz}	0	$2iQ_{yz}$	$-2iQ_{yz}$
S_y		iS_x	iQ_{xy}	$i(Q_{xx} - Q_{zz})$	$-iQ_{yz}$	$-2iQ_{xz}$	0	$2iQ_{xz}$
S_z			$-iQ_{xz}$	iQ_{yz}	$i(Q_{yy} - Q_{xx})$	$2iQ_{xy}$	$-2iQ_{xy}$	0
Q_{yz}				$-iS_z$	iS_y	0	$-2iS_x$	$2iS_x$
Q_{xz}					$-iS_x$	$2iS_y$	0	$-2iS_y$
Q_{xy}						$-2iS_z$	$2iS_z$	0
Q_{xx}							0	0
Q_{yy}								0

Table A.3: Commutators of the dipole-quadrupole basis. There are seven closed SU(2) subspaces: $\{S_x, S_y, S_z\}$, $\{Q_{xz}, Q_{yz}, S_z\}$, $\{S_x, Q_{yz}, (Q_{zz} - Q_{yy})\}$, $\{S_x, Q_{xz}, Q_{xy})\}$, $\{S_y, Q_{xz}, (Q_{xx} - Q_{zz})\}$, $\{S_y, Q_{yz}, Q_{xy})\}$, and $\{S_z, Q_{xy}, (Q_{yy} - Q_{xx})\}$; 3 of which are linearly independent. These SU(2) projections can be used to illustrate the SU(3) space on multiple Bloch spheres with three spanning the space.

APPENDIX B

CUMULANTS

In order to characterize the evolution of the simple pendulum in Chapter 4 and the spin-1 BEC in Chapter 7, central moments (u_n) and cumulants (κ_n) were calculated from the simulation and data points. The general expression for the n^{th} central moment, u_n, is derived from a generating function, which yields a closed expression given by $u_n = \langle (x - \bar{x})^n \rangle$. Though this expression can be used to calculate the central moments from the simulation and data, most mathematics software have readily available functions for calculating the central moment.

A closed expression for the n^{th} cumulant, κ_n does not exist. Instead, the cumulants are obtained from a generating function in terms of the moment-generating function:

$$g(t) \equiv \sum_{n=1}^{\infty} \kappa_n \frac{t^n}{n!} = \ln\left(1 + \sum_{n=1}^{\infty} \frac{u'_n t^n}{n!}\right)$$

where u'_n is the n^{th} non-central moment. The n^{th} cumulant is given by the n^{th} derivative of $g(t)$ evaluated at $t = 0$:

$$\kappa_n = \frac{\partial^n}{\partial t^n} g(t)\bigg|_{t=0}$$

$$\kappa_1 = u'_1$$

$$\kappa_2 = u'_2 - {u'_1}^2$$

$$\kappa_3 = u'_3 - 3u'_2 u'_1 + 2{u'_1}^3$$

$$\kappa_4 = u'_4 - 4u'_3 u'_1 - 3{u'_2}^2 + 12u'_2 {u'_1}^2 - 6{u'_1}^4$$

$$\kappa_5 = u'_5 - 5u'_4 u'_1 - 10u'_3 u'_2 + 20u'_3 {u'_1}^2 + 30{u'_2}^2 u'_1 - 60u'_2 {u'_1}^3 + 24{u'_1}^5$$

$$\kappa_6 = u'_6 - 6u'_5 u'_1 - 15u'_4 u'_2 + 30u'_4 {u'_1}^2 - 10{u'_3}^2 + 120u'_3 u'_2 u'_1 - 120u'_3 {u'_1}^3 + 30{u'_2}^3 - 270{u'_2}^2 {u'_1}^2 + 360u'_2 {u'_1}^4 - 120{u'_1}^6.$$

To express the cumulants in terms of the central moments for $n > 1$, drop all of the terms in which u'_1 appears above:

$$\kappa_1 = u'_1 = \text{ Mean}$$

$$\kappa_2 = u'_2 = \text{ Variance}$$

$$\kappa_3 = u'_3 \propto \text{ Skew}$$

$$\kappa_4 = u'_4 - 3{u'_2}^2 \propto \text{ Kurtosis}$$

$$\kappa_5 = u'_5 - 10u'_3u'_2$$

$$\kappa_6 = u'_6 - 15u'_4u'_2 - 10{u'_3}^2 + 30{u'_2}^3.$$

Just as with the central moments, the expressions above can be used to calculate the cumulants; however, most mathematics software have readily available functions for calculating the cumulants from a set of values.

References

[1] M. H. Anderson, J. R. Ensher, M. R. Matthews, C. E. Wieman, and E. A. Cornell, "Observation of Bose-Einstein Condensation in a Dilute Atomic Vapor," *Science* **269**, pp. 198 (1995).

[2] C. C. Bradley, C. A. Sackett, and R. G. Hulet, "Bose-Einstein Condensation of Lithium: Observation of Limited Condensate Number," *Phys. Rev. Lett.* **78**, 985 (1997).

[3] K. B. Davis, M. O. Mewes, M. R. Andrews, N. J. van Druten, D. S. Durfee, D. M. Kurn, and W. Ketterle, "Bose-Einstein Condensation in a Gas of Sodium Atoms," *Phys. Rev. Lett.* **75**, 3969 (1995).

[4] W. C. Stwalley and L. H. Nosanow, "Possible "New" Quantum Systems," *Phys. Rev. Lett.* **36**, 910 (1976).

[5] I. F. Silvera and J. T. M. Walraven, "Stabilization of Atomic Hydrogen at Low Temperature," *Phys. Rev. Lett.* **44**, 164 (1980).

[6] E. L. Raab, M. Prentiss, A. Cable, S. Chu, and D. E. Pritchard, "Trapping of Neutral Sodium Atoms with Radiation Pressure," *Phys. Rev. Lett.* **59**, 2631 (1987).

[7] C. Monroe, W. Swann, H. Robinson, and C. Wieman, "Very cold trapped atoms in a vapor cell," *Phys. Rev. Lett.* **65**, 1571 (1990).

[8] M. R. Andrews, C. G. Townsend, H.-J. Miesner, D. S. Durfee, D. M. Kurn, and W. Ketterle, "Observation of Interference between Two Bose Condensates," *Science* **275**, pp. 637 (1997).

[9] I. Bloch, T. W. Hänsch, and T. Esslinger, "Measurement of the spatial coherence of a trapped bose gas at the phase transition," *Nature* **403**, 166 (2000).

[10] B. P. Anderson and M. A. Kasevich, "Macroscopic Quantum Interference from Atomic Tunnel Arrays," *Science* **282**, 1686 (1998) http://www.sciencemag.org/content/282/5394/1686.full.pdf.

[11] M. Albiez, R. Gati, J. Fölling, S. Hunsmann, M. Cristiani, and M. K. Oberthaler, "Direct Observation of Tunneling and Nonlinear Self-Trapping in a Single Bosonic Josephson Junction," *Phys. Rev. Lett.* **95**, 010402 (2005).

[12] M. Greiner, O. Mandel, T. Esslinger, T. W. Hänsch, and I. Bloch, "Quantum phase transition from a superfluid to a Mott insulator in a gas of ultracold atoms," *Nature* **415**, 39 (2002).

[13] M.-O. Mewes, M. R. Andrews, D. M. Kurn, D. S. Durfee, C. G. Townsend, and W. Ketterle, "Output Coupler for Bose-Einstein Condensed Atoms," *Phys. Rev. Lett.* **78**, 582 (1997).

[14] E. W. Hagley, L. Deng, M. Kozuma, J. Wen, K. Helmerson, S. L. Rolston, and W. D. Phillips, "A Well-Collimated Quasi-Continuous Atom Laser," *Science* **283**, 1706 (1999) http://www.sciencemag.org/content/283/5408/1706.full.pdf.

[15] I. Bloch, T. W. Hänsch, and T. Esslinger, "Atom Laser with a cw Output Coupler," *Phys. Rev. Lett.* **82**, 3008 (1999).

[16] C. Pethick and H. Smith, *Bose-Einstein condensation in dilute gases* (Cambridge University Press, 2002).

[17] G. Baym and C. J. Pethick, "Ground-State Properties of Magnetically Trapped Bose-Condensed Rubidium Gas," *Phys. Rev. Lett.* **76**, 6 (1996).

[18] F. Dalfovo and S. Stringari, "Bosons in anisotropic traps: Ground state and vortices," *Phys. Rev. A* **53**, 2477 (1996).

[19] C. C. Bradley, C. A. Sackett, and R. G. Hulet, "Bose-Einstein Condensation of Lithium: Observation of Limited Condensate Number," *Phys. Rev. Lett.* **78**, 985 (1997).

[20] E. Donley, N. Claussen, S. Cornish, J. Roberts, E. Cornell, and C. Wieman, "Dynamics of collapsing and exploding Bose-Einstein condensates," *Nature* **412** (2001).

[21] M. R. Matthews, B. P. Anderson, P. C. Haljan, D. S. Hall, C. E. Wieman, and E. A. Cornell, "Vortices in a Bose-Einstein Condensate," *Phys. Rev. Lett.* **83**, 2498 (1999).

[22] K. W. Madison, F. Chevy, W. Wohlleben, and J. Dalibard, "Vortex Formation in a Stirred Bose-Einstein Condensate," *Phys. Rev. Lett.* **84**, 806 (2000).

[23] J. R. Abo-Shaeer, C. Raman, J. M. Vogels, and W. Ketterle, "Observation of Vortex Lattices in Bose-Einstein Condensates," *Science* **292**, 476 (2001) http://www.sciencemag.org/content/292/5516/476.full.pdf.

[24] D. S. Jin, J. R. Ensher, M. R. Matthews, C. E. Wieman, and E. A. Cornell, "Collective Excitations of a Bose-Einstein Condensate in a Dilute Gas," *Phys. Rev. Lett.* **77**, 420 (1996).

[25] M.-O. Mewes, M. R. Andrews, N. J. van Druten, D. M. Kurn, D. S. Durfee, C. G. Townsend, and W. Ketterle, "Collective Excitations of a Bose-Einstein Condensate in a Magnetic Trap," *Phys. Rev. Lett.* **77**, 988 (1996).

[26] M. R. Andrews, D. M. Kurn, H.-J. Miesner, D. S. Durfee, C. G. Townsend, S. Inouye, and W. Ketterle, "Propagation of Sound in a Bose-Einstein Condensate," *Phys. Rev. Lett.* **79**, 553 (1997).

[27] W. Hansel, P. Hommelhoff, T. Hansch, and J. Reichel, "Bose-Einstein condensation on a microelectronic chip," *Nature* **413** (2001).

[28] H. Ott, J. Fortagh, G. Schlotterbeck, A. Grossmann, and C. Zimmermann, "Bose-Einstein Condensation in a Surface Microtrap," *Phys. Rev. Lett.* **87**, 230401 (2001).

[29] T.-L. Ho, "Spinor Bose Condensates in Optical Traps," *Phys. Rev. Lett.* **81**, 742 (1998).

[30] T. Ohmi and K. Machida, "Bose-Einstein Condensation with Internal Degrees of Freedom in Alkali Atom Gases," *J. Phys. Soc. Jpn* **67**, 1822 (1998).

[31] C. J. Myatt, E. A. Burt, R. W. Ghrist, E. A. Cornell, and C. E. Wieman, "Production of Two Overlapping Bose-Einstein Condensates by Sympathetic Cooling," *Phys. Rev. Lett.* **78**, 586 (1997).

[32] J. Stenger, S. Inouye, D. M. Stamper-Kurn, H.-J. Miesner, and W. Ketterle, "Spin domains in ground-state Bose-Einstein condensates," *Nature* **396**, 345 (1998).

[33] H. Schmaljohann, M. Erhard, J. Kronjäger, M. Kottke, S. van Staa, L. Cacciapuoti, J. J. Arlt, K. Bongs, and K. Sengstock, "Dynamics of $F = 2$ Spinor Bose-Einstein Condensates," *Phys. Rev. Lett.* **92**, 040402 (2004).

[34] M.-S. Chang, C. D. Hamley, M. D. Barrett, J. A. Sauer, K. M. Fortier, W. Zhang, L. You, and M. S. Chapman, "Observation of Spinor Dynamics in Optically Trapped ^{87}Rb Bose-Einstein Condensates," *Phys. Rev. Lett.* **92**, 140403 (2004).

[35] M. D. Barrett, J. A. Sauer, and M. S. Chapman, "All-Optical Formation of an Atomic Bose-Einstein Condensate," *Phys. Rev. Lett.* **87**, 010404 (2001).

[36] M.-S. Chang, Q. Qin, W. Zhang, and M. S. Chapman, "Coherent spinor dynamics in a spin-1 Bose condensate," *Nature Physics* **1**, 111 (2005).

[37] E. M. Bookjans, C. D. Hamley, and M. S. Chapman, "Strong Quantum Spin Correlations Observed in Atomic Spin Mixing," *Phys. Rev. Lett.* **107**, 210406 (2011).

[38] C. D. Hamley, C. Gerving, T. Hoang, E. M. Bookjans, and M. S. Chapman, "Spin-nematic squeezed vacuum in a quantum gas," *Nature Phys.* **8**, 305 (2012).

[39] D. M. Stamper-Kurn, M. R. Andrews, A. P. Chikkatur, S. Inouye, H.-J. Miesner, J. Stenger, and W. Ketterle, "Optical Confinement of a Bose-Einstein Condensate," *Phys. Rev. Lett.* **80**, 2027 (1998).

[40] S. Inouye, M. R. Andrews, J. Stenger, H.-J. Miesner, D. M. Stamper-Kurn, and W. Ketterle, "Observation of Feshbach resonances in a Bose-Einstein condensate," *Nature* **392**, 151 (1998).

[41] H.-J. Miesner, D. M. Stamper-Kurn, J. Stenger, S. Inouye, A. P. Chikkatur, and W. Ketterle, "Observation of Metastable States in Spinor Bose-Einstein Condensates," *Phys. Rev. Lett.* **82**, 2228 (1999).

[42] D. M. Stamper-Kurn, H.-J. Miesner, A. P. Chikkatur, S. Inouye, J. Stenger, and W. Ketterle, "Quantum Tunneling across Spin Domains in a Bose-Einstein Condensate," *Phys. Rev. Lett.* **83**, 661 (1999).

[43] A. Lamacraft, "Quantum Quenches in a Spinor Condensate," *Phys. Rev. Lett.* **98**, 160404 (2007).

[44] J. Kronjäger, C. Becker, M. Brinkmann, R. Walser, P. Navez, K. Bongs, and K. Sengstock, "Evolution of a spinor condensate: Coherent dynamics, dephasing, and revivals," *Phys. Rev. A* **72**, 063619 (2005).

[45] J. Kronjäger, C. Becker, P. Navez, K. Bongs, and K. Sengstock, "Magnetically Tuned Spin Dynamics Resonance," *Phys. Rev. Lett.* **97**, 110404 (2006).

[46] A. T. Black, E. Gomez, L. D. Turner, S. Jung, and P. D. Lett, "Spinor Dynamics in an Antiferromagnetic Spin-1 Condensate," *Phys. Rev. Lett.* **99**, 070403 (2007).

[47] M.-S. Chang, *Coherent Spin Dynamics of a Spin-1 Bose-Einstein Condensate*, PhD thesis Georgia Institute of Technology 2006.

[48] L. E. Sadler, J. M. Higbie, S. R. Leslie, M. Vengalattore, and D. M. Stamper-Kurn, "Spontaneous symmetry breaking in a quenched ferromagnetic spinor Bose-Einstein condensate," *Nature* **443**, 312 (2006).

[49] M. Vengalattore, S. R. Leslie, J. Guzman, and D. M. Stamper-Kurn, "Spontaneously Modulated Spin Textures in a Dipolar Spinor Bose-Einstein Condensate," *Phys. Rev. Lett.* **100**, 170403 (2008).

[50] C. Klempt, O. Topic, G. Gebreyesus, M. Scherer, T. Henninger, P. Hyllus, W. Ertmer, L. Santos, and J. J. Arlt, "Multiresonant Spinor Dynamics in a Bose-Einstein Condensate," *Phys. Rev. Lett.* **103**, 195302 (2009).

[51] L. S. Leslie, A. Hansen, K. C. Wright, B. M. Deutsch, and N. P. Bigelow, "Creation and Detection of Skyrmions in a Bose-Einstein Condensate," *Phys. Rev. Lett.* **103**, 250401 (2009).

[52] E. M. Bookjans, A. Vinit, and C. Raman, "Quantum Phase Transition in an Antiferromagnetic Spinor Bose-Einstein Condensate," *Phys. Rev. Lett.* **107**, 195306 (2011).

[53] Y. Liu, E. Gomez, S. E. Maxwell, L. D. Turner, E. Tiesinga, and P. D. Lett, "Number Fluctuations and Energy Dissipation in Sodium Spinor Condensates," *Phys. Rev. Lett.* **102**, 225301 (2009).

[54] S. R. Leslie, J. Guzman, M. Vengalattore, J. D. Sau, M. L. Cohen, and D. M. Stamper-Kurn, "Amplification of fluctuations in a spinor Bose-Einstein condensate," *Phys. Rev. A* **79**, 043631 (2009).

[55] C. Klempt, O. Topic, G. Gebreyesus, M. Scherer, T. Henninger, P. Hyllus, W. Ertmer, L. Santos, and J. J. Arlt, "Parametric Amplification of Vacuum Fluctuations in a Spinor Condensate," *Phys. Rev. Lett.* **104**, 195303 (2010).

[56] B. Lücke, M. Scherer, J. Kruse, L. Pezz, F. Deuretzbacher, P. Hyllus, O. Topic, J. Peise, W. Ertmer, J. Arlt, L. Santos, A. Smerzi, and C. Klempt, "Twin Matter Waves for Interferometry Beyond the Classical Limit," *Science* **334**, 773 (2011).

[57] E. A. Cornell, D. S. Hall, M. R. Matthews, and C. E. Wieman, "Having It Both Ways: Distinguishable Yet Phase-Coherent Mixtures of Bose-Einstein Condensates," *Journal of Low Temperature Physics* **113**, 151 (1998), 10.1023/A:1022513609071.

[58] C. D. Hamley, *Spin-Nematic Squeezing in a Spin-1 Bose Einstein Condensate*, PhD thesis Georgia Institute of Technology 2012.

[59] W. Zhang, S. Yi, and L. You, "Mean field ground state of a spin-1 condensate in a magnetic field," *New Journal of Physics* **5**, 77 (2003).

[60] W. Zhang, D. L. Zhou, M.-S. Chang, M. S. Chapman, and L. You, "Coherent spin mixing dynamics in a spin-1 atomic condensate," *Phys. Rev. A* **72**, 013602 (2005).

[61] K. Murata, H. Saito, and M. Ueda, "Broken-axisymmetry phase of a spin-1 ferromagnetic Bose-Einstein condensate," *Phys. Rev. A* **75**, 013607 (2007).

[62] C. K. Law, H. Pu, and N. P. Bigelow, "Quantum Spins Mixing in Spinor Bose-Einstein Condensates," *Phys. Rev. Lett.* **81**, 5257 (1998).

[63] H. Pu, C. K. Law, S. Raghavan, J. H. Eberly, and N. P. Bigelow, "Spin-mixing dynamics of a spinor Bose-Einstein condensate," *Phys. Rev. A* **60**, 1463 (1999).

[64] G. I. Mias, N. R. Cooper, and S. M. Girvin, "Quantum noise, scaling, and domain formation in a spinor Bose-Einstein condensate," *Phys. Rev. A* **77**, 023616 (2008).

[65] D. R. Romano and E. J. V. de Passos, "Population and phase dynamics of $F = 1$ spinor condensates in an external magnetic field," *Phys. Rev. A* **70**, 043614 (2004).

[66] J. Heinze, F. Deuretzbacher, and D. Pfannkuche, "Influence of the particle number on the spin dynamics of ultracold atoms," *Phys. Rev. A* **82**, 023617 (2010).

[67] Z. Chen, C. Bao, and Z. Li, "Effect of a Magnetic Field on the Spin Evolution of ^{87}Rb Bose–Einstein Condensates with Zero Polarization," *Journal of the Physical Society of Japan* **78**, 114002 (2009).

[68] M. D. Barrett, *A QUEST for BEC: an all optical alternative*, PhD thesis Georgia Institute of Technology 2002.

[69] E. M. Bookjans, *Relative Number Squeezing in a Spin-1 Bose-Einstein Condensate*, PhD thesis Georgia Institute of Technology 2010.

[70] S. Yi, L. You, and H. Pu, "Quantum Phases of Dipolar Spinor Condensates," *Phys. Rev. Lett.* **93**, 040403 (2004).

[71] C. S. Gerving, T. M. Hoang, B. J. Land, M. Anquez, C. D. Hamley, and M. S. Chapman, "Non-equilibrium dynamics of an unstable quantum pendulum explored in a spin-1 Bose-Einstein condensate," *Nature Communications* (2012).

[72] M. Yasunaga and M. Tsubota, "Internal Josephson effects in spinor dipolar Bose-Einstein condensates," *Phys. Rev. A* **81**, 023624 (2010).

[73] D. Steck, "Rubidium 87 D Line Data,", available online at `http://steck.us/alkalidata` 2008.

[74] L.-M. Duan, J. I. Cirac, and P. Zoller, "Quantum entanglement in spinor Bose-Einstein condensates," *Phys. Rev. A* **65**, 033619 (2002).

[75] M. Luo, C. Bao, and Z. Li, "Evolution of the average populations of spin components of spin-1 Bose-Einstein condensates beyond mean-field theory," *Phys. Rev. A* **77**, 043625 (2008).

[76] W. H. Zurek, U. Dorner, and P. Zoller, "Dynamics of a Quantum Phase Transition," *Phys. Rev. Lett.* **95**, 105701 (2005).

[77] B. Damski and W. H. Zurek, "Dynamics of a Quantum Phase Transition in a Ferromagnetic Bose-Einstein Condensate," *Phys. Rev. Lett.* **99**, 130402 (2007).

[78] S. Sachdev, *Quantum Phase Transitions* (Cambridge University Press, Cambridge, UK, 1999).

[79] R. Barnett, A. Polkovnikov, and M. Vengalattore, "Prethermalization in quenched spinor condensates," *Phys. Rev. A* **84**, 023606 (2011).

[80] D. F. Walls and G. J. Milburn, *Quantum optics* (Springer, Berlin ; New York :, 1994).

[81] H. Carmichael, *An open systems approach to quantum optics: lectures presented at the Université libre de Bruxelles, October 28 to November 4, 1991*Lecture notes in physics: Monographs (Springer-Verlag, 1993).

[82] C. W. Gardiner, A. S. Parkins, and P. Zoller, "Wave-function quantum stochastic differential equations and quantum-jump simulation methods," *Phys. Rev. A* **46**, 4363 (1992).

[83] S. Tan, "A computational toolbox for quantum and atomic optics," *Journal of Optics B: Quantum and Semiclassical Optics* **1**, 424 (1999).

[84] G. P. Cook and C. S. Zaidins, "The quantum point-mass pendulum," *American Journal of Physics* **54**, 259 (1986).

[85] M. M. Nieto, "Angular Momentum Uncertainty Relation and the Three-Dimensional Oscillator in the Coherent States," *Phys. Rev. Lett.* **18**, 182 (1967).

[86] J. Candy and W. Rozmus, "A symplectic integration algorithm for separable Hamiltonian functions," *Journal of Computational Physics* **92**, 230 (1991).

[87] X. Tan, "Almost symplectic Runge-Kutta schemes for Hamiltonian systems," *Journal of Computational Physics* **203**, 250 (2005).

[88] J. Hald, J. L. Sørensen, C. Schori, and E. S. Polzik, "Spin Squeezed Atoms: A Macroscopic Entangled Ensemble Created by Light," *Phys. Rev. Lett.* **83**, 1319 (1999).

[89] A. Kuzmich, L. Mandel, and N. P. Bigelow, "Generation of Spin Squeezing via Continuous Quantum Nondemolition Measurement," *Phys. Rev. Lett.* **85**, 1594 (2000).

[90] T. Takano, M. Fuyama, R. Namiki, and Y. Takahashi, "Spin Squeezing of a Cold Atomic Ensemble with the Nuclear Spin of One-Half," *Phys. Rev. Lett.* **102**, 033601 (2009).

[91] Z. Chen, J. G. Bohnet, S. R. Sankar, J. Dai, and J. K. Thompson, "Conditional Spin Squeezing of a Large Ensemble via the Vacuum Rabi Splitting," *Phys. Rev. Lett.* **106**, 133601 (2011).

[92] I. D. Leroux, M. H. Schleier-Smith, and V. Vuletić, "Implementation of Cavity Squeezing of a Collective Atomic Spin," *Phys. Rev. Lett.* **104**, 073602 (2010).

[93] C. Gross, T. Zibold, E. Nicklas, J. Estève, and M. K. Oberthaler, "Nonlinear atom interferometer surpasses classical precision limit," *Nature* **464**, 1165 (2010).

[94] M. F. Riedel, P. Böhi, Y. Li, T. W. Hänsch, A. Sinatra, and P. Treutlein, "Atom-chip-based generation of entanglement for quantum metrology," *Nature* **464**, 1170 (2010).

[95] M. Kitagawa and M. Ueda, "Squeezed spin states," *Phys. Rev. A* **47**, 5138 (1993).

[96] D. J. Wineland, J. J. Bollinger, W. M. Itano, F. L. Moore, and D. J. Heinzen, "Spin squeezing and reduced quantum noise in spectroscopy," *Phys. Rev. A* **46**, R6797 (1992).

[97] D. Rugar and P. Grütter, "Mechanical parametric amplification and thermomechanical noise squeezing," *Phys. Rev. Lett.* **67**, 699 (1991).

[98] F. DiFilippo, V. Natarajan, K. R. Boyce, and D. E. Pritchard, "Classical amplitude squeezing for precision measurements," *Phys. Rev. Lett.* **68**, 2859 (1992).

[99] V. Natarajan, F. DiFilippo, and D. E. Pritchard, "Classical Squeezing of an Oscillator for Subthermal Noise Operation," *Phys. Rev. Lett.* **74**, 2855 (1995).

[100] M. Leibscher and B. Schmidt, "Quantum dynamics of a plane pendulum," *Phys. Rev. A* **80**, 012510 (2009).

[101] C. M. Marle, "The inception of symplectic geometry: the works of Lagrange and Poisson during the years 18081810,", Pre-published at arXiv.org 2009.

[102] P. J. Channell and C. Scovel, "Symplectic integration of Hamiltonian systems," *Nonlinearity* **3** (1990).

[103] A. C. da Silva, "Symplectic Geometry," in *Handbook of Differential Geometry, vol. 2* 2004.

[104] D. McDuff, "What is Symplectic Geometry,", A Talk Given at the European Women in Mathematics conference 2007.

[105] R. I. McLachlan and P. Atela, "The accuracy of symplectic integrators," *Nonlinearity* **5** (1992).

[106] C. Klempt, T. van Zoest, T. Henninger, O. Topic, E. Rasel, W. Ertmer, and J. Arlt, "Ultraviolet light-induced atom desorption for large rubidium and potassium magneto-optical traps," *Phys. Rev. A* **73**, 013410 (2006).

[107] H. J. Metcalf and P. van der Straten, *Laser Cooling and Trapping* (Springer-Verlag, New York, 1999).

[108] W. Demtröder, *Laser spectroscopy: basic concepts and instrumentation*Advanced texts in physics (Springer, 2003).

[109] R. Grimm, M. Weidermüller, and Y. B. Ovchinnikov, "Optical Dipole Traps for Neutral Atoms," *Adv. Atom Mol. Opt. Phys.* **42**, 95 (1999).

[110] Y. Liu, S. Jung, S. E. Maxwell, L. D. Turner, E. Tiesinga, and P. D. Lett, "Quantum Phase Transitions and Continuous Observation of Spinor Dynamics in an Antiferromagnetic Condensate," *Phys. Rev. Lett.* **102**, 125301 (2009).

[111] T. Zibold, *Classical Bifurcation in Entangled Generation in an Internal Bosonic Josephson Junction*, PhD thesis Ruperto-Carola-University of Heidelberg 2012.

[112] M. Gring, M. Kuhnert, T. Langen, T. Kitagawa, B. Rauer, M. Schreitl, I. Mazets, D. A. Smith, E. Demler, and J. Schmiedmayer, "Relaxation and Prethermalization in an Isolated Quantum System," *Science* **337**, 1318 (2012).

[113] V. Gritsev, E. Altman, E. Demler, and A. Polkovnikov, "Full quantum distribution of contrast in interference experiments between interacting one-dimensional Bose liquids," *NPhys* **2** (2006).

[114] H.-P. Stimming, N. J. Mauser, J. Schmiedmayer, and I. E. Mazets, "Dephasing in coherently split quasicondensates," *Phys. Rev. A* **83**, 023618 (2011).

[115] A. Smerzi, S. Fantoni, S. Giovanazzi, and S. R. Shenoy, "Quantum Coherent Atomic Tunneling between Two Trapped Bose-Einstein Condensates," *Phys. Rev. Lett.* **79**, 4950 (1997).

[116] S. Raghavan, A. Smerzi, S. Fantoni, and S. R. Shenoy, "Coherent oscillations between two weakly coupled Bose-Einstein condensates: Josephson effects, π oscillations, and macroscopic quantum self-trapping," *Phys. Rev. A* **59**, 620 (1999).

[117] M. Chuchem, K. Smith-Mannschott, M. Hiller, T. Kottos, A. Vardi, and D. Cohen, "Quantum dynamics in the bosonic Josephson junction," *Phys. Rev. A* **82**, 053617 (2010).

[118] M. C. Tichy, J. F. Sherson, and K. Mølmer, "Dynamical effects of exchange symmetry breaking in mixtures of interacting bosons," *Phys. Rev. A* **86**, 063630 (2012).

[119] J. R. Taylor, *An Introduction to Error Analysis*, Second ed. (University Science Books, 1997).

[120] H. Ankarali, A. Canan-Yazici, and S. Ankarali, "A Bootstrap Confidence Interval for Skewness and Kurtosis and Properties of t-test in Small Samples from Normal Distribution,", Presented at the XI. National Congress of Biostatistics, May 27-30 2008.

[121] D. Wright and J. Herrington, "Problematic standard errors and confidence intervals for skewness and kurtosis," *Behav Res Methods* **43**, 8 (2011).

[122] R. B. Diener and T.-L. Ho, "Quantum spin dynamics of spin-1 Bose gas,", Preprint at http://arxiv.org/abs/cond-mat/0608732 2006.

[123] A. C. Bovik, *Handbook of Image and Video Processing (Communications, Networking and Multimedia)* (Academic Press, Inc., Orlando, FL, USA, 2005).